HIGGS BOSON PROPERTIES AT COLLIDERS

by

Zhuoni Qian

Bachelor of Science, East China Normal University, 2012

Master of Science, University of Pittsburgh, 2014

Submitted to the Graduate Faculty of

the Kenneth P. Dietrich School of Arts and Sciences in partial

fulfillment

of the requirements for the degree of

Doctor of Philosophy in Physics and Astronomy

University of Pittsburgh

2017

UNIVERSITY OF PITTSBURGH

THE DIETRICH SCHOOL OF ARTS & SCIENCES

This dissertation was presented

by

Zhuoni Qian

It was defended on

May 1st 2017

and approved by

Tao Han, Department of Astronomy and Physics, University of Pittsburgh

Ayres Freitas, Department of Astronomy and Physics, University of Pittsburgh

James A Mueller, Department of Astronomy and Physics, University of Pittsburgh

D. John Hillier, Department of Astronomy and Physics, University of Pittsburgh

Anna Vainchtein, Department of Mathematics, University of Pittsburgh

Dissertation Director: Tao Han, Department of Astronomy and Physics, University of Pittsburgh

HIGGS BOSON PROPERTIES AT COLLIDERS

Zhuoni Qian, PhD

University of Pittsburgh, 2017

Since its discovery at the large hadron collider (LHC) in 2012, the Higgs boson and its properties are under intense investigation from both theorists and experimentalists. As the only scalar particle in the Standard Model (SM), the Higgs is believed to be closely related to the nature of electroweak symmetry breaking and the mass generation of fundamental massive particles. Respectively, they manifest as the couplings between the Higgs to the massive bosons (gauge couplings) and the Higgs to the massive fermions (Yukawa couplings). Thus, measurements of the Higgs sector properties are highly motivated either to confirm our current theory, the standard model, or to reveal possible new theories.

With the ongoing effort at the LHC, the Higgs is studied through various production and decay channels. However at a hadron collider, the large background and the ignorance of the partonic center of mass energy make testing many parameters of the Higgs sector challenging. For this dissertation I studied Higgs processes at a lepton collider, explored mass determination abilities for certain processes at a lepton collider and also studied the challenging Higgs decay to light jets at the LHC. These studies suggest new observables to improve our sensitivity to the Higgs sector and to constrain possible new physics deviations.

In order, I present in Chapter 1 an introduction of the Standard Model Higgs and its detection at colliders. Chapter 2 details the study on Higgs production through the ZZ fusion process at the lepton collider and the measurement of the inclusive rate. Our study improves the prospecting sensitivities on the standard model couplings, and puts further constraints on dimension-6 effective operators which are generic in quantifying beyond standard model (BSM) deviations. Chapter 3 describes the Higgs to light jets decays through the boosted Vh

associated production at the LHC. Extrapolation of sensitivities on small Yukawa couplings at the hadron collider are discussed and achieved. Chapter 4 presents another study on linear collider, further exploring its many advantages on kinematic reconstruction and precision measurement.

LaTeX.

TABLE OF CONTENTS

PREFACE xi

1.0 INTRODUCTION 1

1.1 A Recount of the Standard Model 1

1.1.1 Quantum Electrodynamics 2

1.1.2 Quantum Chromodynamics 3

1.1.3 Electroweak Theory 5

1.2 The Higgs Sector in the Standard Model 6

1.3 Higgs Properties at Colliders 9

1.4 Status of Higgs Measurements 12

2.0 HIGGS PRODUCTION THROUGH ZZ FUSION IN E^+E^- COLLISIONS 15

2.1 Sensitivity Analysis 17

2.1.1 Simulation framework 21

2.1.2 500 GeV analysis 22

2.1.3 1-TeV analysis 25

2.1.4 Multivariate log-likelihood analyses 26

2.2 Impact on Higgs Physics 28

2.2.1 Higgs width and coupling Fits 28

2.2.2 Operator analysis 29

2.3 Conclusions 32

3.0 HIGGS DECAY TO LIGHT JETS AT THE LHC 35

3.1 Signal and Background Processes 36

3.2 Signal Selection . . . 39
3.2.1 $\ell^+\ell^- + jj$ channel . . . 41
3.2.2 $\ell^\pm + \not{E}_T + jj$ channel . . . 42
3.2.3 $\not{E}_T + jj$ channel . . . 42
3.2.4 Background control . . . 43
3.3 Alternative Discriminants with Missing Energies . . . 45
3.4 Results and Discussion . . . 46
3.4.1 Signal significance . . . 46
3.4.2 Bounds on the branching fractions and correlations with $h \to b\bar{b},\ c\bar{c}$ . . . 47
3.4.3 Bounds on light-quark Yukawa couplings . . . 50
3.5 Summary and Conclusions . . . 51
4.0 ANTLER TOPOLOGY FOR MASS DETERMINATION . . . 62
4.1 Motivation . . . 62
4.2 Massless visible particle cases: smuon pair production . . . 65
4.2.1 The kinematics of cusps and endpoints . . . 66
4.2.2 The effects of acceptance cuts . . . 71
4.2.3 Mass measurements with realistic considerations . . . 73
4.2.3.1 Backgrounds and simulation procedure . . . 73
4.2.3.2 `Case-A`: $\tilde{\mu}_R\tilde{\mu}_R$ pair production . . . 76
4.2.3.3 `Case-B`: production of $\tilde{\mu}_R\tilde{\mu}_R$ and $\tilde{\mu}_L\tilde{\mu}_L$ . . . 78
4.2.4 The mass measurement precision . . . 82
4.3 Massive visible particle case: chargino pair production . . . 83
4.4 Summary and conclusions . . . 86
5.0 CONCLUSIONS . . . 95
APPENDIX A. CONSIDERATION OF ONE-PHOTON SENSITIVITY . . . 98
APPENDIX B. CUSPS AND ENDPOINTS OF THE ANTLER PROCESS 100
APPENDIX C. LOG-LIKELIHOOD COMBINATION . . . 104
BIBLIOGRAPHY . . . 106

LIST OF TABLES

1 Cross section (fb) for signal $e^-e^+ + h$ and background $e^-e^+\gamma$ after sequence of cuts. 20

2 Cuts applied at ILC 500 GeV. 23

3 Cross sections for signal and background processes at ILC 500 GeV. 25

4 Cuts applied at ILC 1 TeV. 26

5 Cross sections for signal and background processes at ILC 1 TeV with 1000 fb^{-1} of integrated luminosity. 28

6 The improvement on selected coupling precisions by incorporating our ZZ fusion analysis from a typical 10-parameter model-independent fit 30

7 Cross sections in units of fb for signal and dominant background processes, with the parton-level cuts of Eq. (3.3), and boosted regions $p_{T(V)} > 150,\ 200$ GeV. 38

8 The consecutive cut efficiencies for signal $\ell^+\ell^-\ jj$ and dominant background processes at the LHC. 55

9 The consecutive cut efficiencies for signal $\ell^\pm \not{E}_T\ jj$ and dominant background processes at the LHC. 55

10 The consecutive cut efficiencies for signal $\not{E}_T\ jj$ and dominant background processes at the LHC. 56

11 Fitted results for the background rates from various fitting functions as in Eqs. (3.7) and (3.8). 58

12 Fitted results for the background rate from various fitting ranges by the fitting function in Eq. (3.7). 58

13 Signal significance achieved from each channel and combined results for both statistics and systematics dominance. 59
14 Flavor tagging efficiency 60
15 Fraction of SM decay channels 60
16 Extrapolated upper bounds at 95% CL on the light-quark Yukawa couplings $\overline{\kappa}_q = y_q/y_b^{\rm SM}$ ($\kappa_q = y_q/y_q^{\rm SM}$) for $q = u, d, s$. 61
17 Illustrative SUSY mass spectrum for `Case-A`, `Case-B` (as introduced in Sec. 4.2.1) and `Case-C` (as introduced in Sec. 4.3). All of the masses are in units of GeV. 67
18 The values of various kinematic cusps and endpoints as seen in Fig. 21, for the mass parameters in Table 17. All of the masses and energies are in units of GeV. 68
19 The values of various kinematic cusps and endpoints for the mass parameters in the `Case-C`. All the masses and energies are in units of GeV. 92
20 The cusp and endpoints of the invariant mass distribution m_{aa} in the three regions of c.m. energy and parameter space. 101

LIST OF FIGURES

1 Vertices between the Higgs and other SM particles at lowest order in the SM. 9

2 Main Higgs production mechanisms at the LHC. 10

3 Main Higgs production mechanisms at the ILC. 11

4 Feynman diagram of the ZZ fusion signal process 16

5 Total cross section (in fb) for $e^-e^+ \to e^-e^+ + h$ versus $\sqrt{s}$. 17

6 Angles θ_1, θ_2 and ϕ as defined in the text. 18

7 Comparison of signal and total background distributions for five variables at 500 GeV 24

8 Comparison of signal and total background distributions for five variables at 1 TeV 27

9 Five-dimensional Log likelihood as a function of r 29

10 Constraints on coefficients of dimension-six operators $\bar{c}_H$ and $\bar{c}_{HB}$ 34

11 Higgs boson transverse momentum distribution for the signal processes $qq \to Zh$ (upper solid curve) and $gg \to Zh$ (lower dashed curve) at the 14 TeV LHC. 37

12 Four kinematical distributions of the signal process $pp \to Zh, h \to gg$ and the leading background $pp \to Zjj$ 53

13 Invariant mass distributions of three jet reconstruction methods 54

14 Invariant mass distributions constructed from (a) two-jet events and (b) three-jet events with different pile-up values $\langle\mu\rangle = 0, 15, 50, 140$, respectively. . . . 54

15 Invariant mass distribution m_{jj} for $Z(\ell^+\ell^-)$+jets with MC simulated events and fitted spectrum 56

16 Generated distribution from three-parameter ansatz function in Eq. (3.7) for m_{jj} with (a) 300 fb^{-1}, (b) and 3000 fb^{-1} (right). 57
17 Fitted results for 300 fb^{-1} (left) and 3000 fb^{-1} (right). 57
18 Scatter plot of 10000 events for the signal (blue crosses) and background (red dots) in the visible $p_T - TvQ$ plane. 59
19 Three-dimensional constraints of signal strengths 60
20 The antler decay diagram of a heavy particle D into two visible particles a_1 and a_2 and two invisible particles X_1 and X_2 through on-shell intermediate particles B_1 and B_2. 63
21 Five normalized kinematic distributions for three cases 69
22 Effects due to various $\not{p}_T$ cuts on five kinematic distributions for `Case-A` for $e^+e^- \to \tilde{\mu}_R\tilde{\mu}_R \to \mu^+\mu^- + \not{E}$ 72
23 Effects due to various E_a cuts on five kinematic distributions for `Case-A` for $e^+e^- \to \tilde{\mu}_R\tilde{\mu}_R \to \mu^+\mu^-\not{E}$ 74
24 Five kinematic distributions for `Case-A` for $e^+e^- \to \tilde{\mu}_R\tilde{\mu}_R \to \mu^+\mu^-\not{E}$ with basic cuts 77
25 Five kinematic distributions for `Case-A` for $e^+e^- \to \tilde{\mu}_R\tilde{\mu}_R \to \mu^+\mu^-\not{E}$ with cut $m_{\rm rec} > 350\,{\rm GeV}$ 79
26 Five kinematic distributions for `Case-B` for $e^+e^- \to \tilde{\mu}_L\tilde{\mu}_L,\ \tilde{\mu}_R\tilde{\mu}_R \to \mu^+\mu^-\not{E}$ with cuts 89
27 Five kinematic distributions for `Case-B` for $e^+e^- \to \tilde{\mu}_L\tilde{\mu}_L,\ \tilde{\mu}_R\tilde{\mu}_R \to \mu^+\mu^-\not{E}$ with cuts and polarized beams 90
28 Five kinematic distributions for `Case-B` for $e^+e^- \to \tilde{\mu}_L\tilde{\mu}_L,\ \tilde{\mu}_R\tilde{\mu}_R \to \mu^+\mu^-\not{E}$ with cuts and opposite polarized beams 91
29 Mass contours for `Case-A` for $e^+e^- \to \tilde{\mu}_R\tilde{\mu}_R \to \mu^+\mu^-\not{E}$ 92
30 Five kinematic distributions for `Case-C` for $e^+e^- \to jj, jj + \not{E}$ with cuts . . . 93
31 Mass contours for `Case-C` for $e^+e^- \to jj, jj + \not{E}$ 94

PREFACE

This is a short acknowledgement proceeding my dissertation.

First and foremost I want to thank my advisor Professor Tao Han. The accomplishment of this dissertation and my completion of the doctorate program owes greatly to him. Along the journey of the past five years, his mentoring and advises have taught me numerous lessons in pursuing an academic career. His understanding of the field, untiring enthusiasm towards work, his sense of integrity and responsibility for the community is inspirational to me.

There are many collaborators and office mates that I have interacted with and learnt much from over my doctoral program. My gratitude goes to them as well. There are Dr. Zhen Liu, Dr. Josh Sayre, who held my hands through my early projects and passed on knowledge that would benefit me throughout the career. Professor Ayres Freitas whose lectures and talks I attended over the years has introduced me to various topics with clarity that I much appreciate. Xing Wang, Daniel Wiegand, Lin Dai, Barmak Shams Es Haghi, Wai Kin Lai, Junmou Chen and Richard Ruiz have shared office with me, and had countless discussions on wide ranges of topics. I enjoyed and appreciated the generous and supportive interactions I had with these officemates. I also wish to thank my committee members and the whole high energy group at Pittsburgh, who have over the years given me their honest and constructive advises.

Lastly I thank my parents for their unfailing support. It owes to them that I stay mostly grounded and dedicated throughout the program.

Zhuoni Qian

Pittsburgh, Pennsylvania

April, 2017

1.0 INTRODUCTION

This chapter serves as an introduction to the necessary concepts, and a motivation to my study on the Higgs measurement. It begins with a description of the current Standard Model (SM) of particle physics, a short recount of its coming into being. Then it details the Higgs mechanism part of the theory, giving a brief derivation of the relation between the Higgs couplings to the massive particles and their masses. It proceeds with a description of the Higgs production, decay and the Higgs detection at both hadron and lepton colliders. Lastly it comments on the current status of experimental measurements.

1.1 A RECOUNT OF THE STANDARD MODEL

Current formulation of the SM was theoretically completed around the 1970s, with the work of many. It summarizes the three out of four fundamental interactions that we currently know of in the nature. Besides gravity, which is described so far by Einstein's general relativity, and is not yet unified with the rest into one quantum field theory respecting unitarity, there are the electromagnetic, weak and strong interactions described in the current framework of the SM. This section recounts the modern history of the SM, which evolved along our understanding of the three interactions. The author realizes that it is difficult to be inclusive in giving credits to all that have contributed, and will focus more on providing the structurally necessary steps that eventually lead to the SM theory.

1.1.1 Quantum Electrodynamics

The first established piece of a modern quantum field theory was from the upgrade of classical electrodynamics to quantum electrodynamics (QED), first attempted in the 1920s by P.A.M. Dirac [1], Enrico Fermi and others, and eventually took its modern form in the late 1940s-1950s. During the process, Bethe's calculation in 1947 on the hyperfine splitting of the hydrogen atom ground state [2] extracted out finite corrections using QED and showed agreement with the experimental measurements of the lamb shift [3]. This instilled confidence in the theory and inspired the renormalization procedure. Later, by writing the fields into Lorentz covariant forms and realizing the idea of renormalization, the modern formalism of QED is established by the work of Tomonaga [4], Schwinger [5], Feynman [6, 7, 8] and Dyson [9, 10] in the late 1940s.

QED is a relativistic quantum field theory of charged fermions, photons and the interactions between. Mathematically it is an abelian gauge theory respecting the $\mathrm{U}(1)_{\mathrm{EM}}$ symmetry, which corresponds to the same gauge symmetry as in Maxwell's classical electromagnetism. In QED, photon is the quanta of the quantized gauge (electromagnetic) field, and charged fermions are the quanta of the Dirac/matter fields. As QED is the first relativistic quantum field theory, it serves as the template to later developments including the SM. Here I am to write down the Lagrangian of the QED in its modern form, and introduce some useful terminologies and symbols. The QED Lagrangian reads,

$$\mathcal{L}_{\mathrm{QED}} = \overline{\psi}(i\gamma^{\mu}D_{\mu} - m)\psi - \frac{1}{4}F_{\mu\nu}F^{\mu\nu}. \tag{1.1}$$

The spacetime index μ, ν (greek letters) run from 0 to 3 and Einstein's summation convention is assumed. ψ is the 4-component Dirac spinor field which represents spin-$\frac{1}{2}$ electron-position fields. The adjoint field is defined as $\overline{\psi} \equiv \psi^{\dagger}\gamma^{0}$. γ^{μ} are Dirac matrices[1]. The covariant derivative is defined as $D_{\mu} \equiv \partial_{\mu} + ieA_{\mu}$. e is the coupling strength or the electric charge magnitude of the ψ field. A_{μ} is a covariant vector field, or the gauge field. Lastly, the

[1] A detailed definition and useful identities of Dirac spinors and Dirac matrices using the same convention can be found in Chapter 2, section 10.2-10.3 of M. Schwartz's quantum field theory textbook [11].

electromagnetic field tensor can be written as $F_{\mu\nu} \equiv \partial_\mu A_\nu - \partial_\nu A_\mu$. Under a U(1) gauge transformation with an arbitrary $\alpha(x)$, the covariant operators and fields transform as:

$$\psi \to e^{i\alpha(x)}\psi, \quad A_\mu(x) \to A_\mu(x) - \frac{1}{e}\partial_\mu \alpha(x). \tag{1.2}$$

It can be checked that the QED Lagrangian is Lorentz invariant and U(1) invariant, or manifestly a relativistic U(1) gauge theory.

1.1.2 Quantum Chromodynamics

Strong interaction was long postulated in order to explain the existence of atomic nucleus, being the stable bound states of electrically charged protons that should fly apart under only electromagnetic interactions. Yet due to the energy scale that was simply experimentally unavailable then, it wasn't until the 1950s that further insights shone into the strong interaction inside the nucleus. By then the invention of bubble chambers and spark chambers started to reveal a plethora of particles called the "hadrons". The hadrons were classified by their electromagnetic charges, and some other quantum numbers such as the isospin (used by Eugene Wigner and Werner Heisenberg) and strangeness (proposed by Murray Gell-Mann and Kazuhiko Nishijima). In the 60s, they were further sorted by their quantum numbers and masses with the eightfold way by Gell-Mann [12] and Yuval Ne'eman [13]. The eightfold way directly inspired the proposals of quark model in 1963 by Gell-Mann and George Zweig [14], both suggested that the hadrons can be made of smaller constituents, or three flavors of quarks up, down and strange (known at the time). In order to resolve the issue of existing hadrons as bound states of quarks in the same state, which seemingly violates Pauli exclusion principle, soon in 1965, Moo-Young Han with Yoichiro Nambu [15] and Oscar W. Greenberg [16] proposed that quarks possess an additional SU(3) gauge degree of freedom, or an additional quantum number, later called the color charge. As pointed out by James Bjorken [17], the cross section measurements from deep inelastic scattering experiment at SLAC implied as well the existence of point-like substructures inside nucleus.

With the foundational work on general non-abelian gauge theory laid out by Chen Ning Yang and Robert Mills in 1954 [18], and the unified electroweak theory in the late 1960s (to

be discussed later), the quark model later was formulated as well into a gauge field theory of colored quarks and color octet gluons, now called Quantum Chromodynamics (QCD). It was mostly attributed to the work of Harald Fritzsch, Heinrich Leutwyler, and Gell-Mann [19] in 1973. During the same year, the asymptotic behavior of QCD was discovered by David Politzer [20], David Gross and Frank Wilczek[21], meaning that the strong interaction gets weaker as the distance between particles gets smaller. It further validates the predictive power of perturbative QCD calculation in short distances or high energy region where the quarks and gluons inside the colliding nuclei can be seen as free. The other end of asymptotic behavior is called confinement, meaning that the strong interaction coupling strength grows with the distance. It explains the fact that we do not observe in nature free colored object.

QCD is a non-abelian gauge theory respecting $SU(3)_{\text{color}}$ gauge symmetry. The additional quantum number carried by quarks was called "color". The eight gauge fields of a SU(3) group are called gluons. The colored quarks in each flavor form the fundamental representation of the group, with their strong interaction mediated by the gluon fields. The non-abelian nature of the SU(3) gauge theory gives rise to interactions among the gauge fields, which is not present in an abelian theory such as QED. The Lagrangian of the theory reads,

$$\mathcal{L}_{\text{QCD}} = \overline{\psi}_i(i(\gamma^\mu D_\mu)_{ij} - m\delta_{ij})\psi_j - \frac{1}{4}G^a_{\mu\nu}G^{\mu\nu}_a. \tag{1.3}$$

Here the latin alphabet i, j are the color indices running from 1 to 3. $D_\mu \equiv \partial_\mu + igA^a_\mu\lambda^a/2$. g is the strong coupling strength. A^a_μ are the gluon fields with 'a' denoting from 1 to 8. λ^a are the eight Gell-Mann matrices [2]. The gluon field strength tensor can be written as,

$$G^a_{\mu\nu} = \partial_\mu A^a_\nu - \partial_\nu A^a_\mu + gf^{abc}A^b_\mu A^c_\nu. \tag{1.4}$$

The f^{abc} are the structure constants of SU(3) gauge group. It is clear to see that in the QCD Lagrangian, there are self interacting terms among the gauge fields such as $\partial_\mu A^a_\nu A^b_\mu A^c_\nu$ etc, which are not present in the abelian theory of QED.

[2] A definition of the Gell-Mann matrices as a set of 3×3 matrices can be again found on Page 485 of Schwartz's books here [11].

1.1.3 Electroweak Theory

The weak interaction made its early appearance as radioactivity which was discovered in 1896 by Henri Becquerel in uranium. Categorizing by the different radioactive emissions, there are alpha, beta and gamma rays, which were known later as energetic Helium nucleus $^4He_2^{2+}$, electron and photon beams respectively. Continuous electron spectra from beta decay was measured by James Chadwick in 1916 and further confirmed by Charles Drummond Ellis and Nevill Mott in the 1920s, and puzzles rose since the results seemed to violate energy and angular momentum conservation. Wolfgang Pauli suggested in 1930 that a new light neutral particle was produced along with the electron, but evade the detection. Enrico Fermi further named the missing particle as "neutrino" and proposed the theory for beta decay in 1933 [22], which became the first model for the weak interaction. Fermi's theory postulate a contact interaction of four fermions, as two pairs of vector currents. The parity-violating axial current contact interaction case was formulated by George Gamow and Edward Teller in 1936 [23]. Much later, the possible existence of parity-violation in weak interaction and ways of detection were suggested in 1956 by T. D. Lee and C. N. Yang [24]. The experimental confirmation came right afterwards in 1957, done by Chien-Shiung Wu's group on beta decay from ^{60}Co nuclei [25]. Soon the correct tensor structure of weak interaction in beta decay was figured out to be vector minus axial vector ($V - A$) by the work of George Sudarshan, Robert Marshak [27] and Richard Feynman, Murray Gell-Mann in 1958 [26]. It was only part of the weak interactions, later known as the charged-current interaction.

At this point, the weak interaction was still governed by a theory of four-fermion contact interaction with the Fermi coupling constant G_F as the coupling strength. According to this theory, the rate of fermion scattering through the weak interaction would grow with the center of mass energy and eventually violate unitarity. It thus became natural to seek to reformulate the weak interaction into a gauge theory, following the successful example of QED. One major difficulty then was that the gauge mediators for weak interaction must be massive, with scales at around 100 GeV, as indicated by the Fermi coupling constant. However, simple mass terms of gauge bosons are forbidden by gauge symmetry. While the mass generation mechanism for the weak gauge bosons remained a puzzle, a proposal by S. L.

Glashow in 1961 unified electromagnetism and weak interactions correctly into a triplet plus a singlet (corresponding later to the gauge bosons of the $\mathrm{SU(2)_L \times U(1)_Y}$ group) interaction using "partial (gauge) symmetry" argument [28], and suggested an additional neutral vector boson, later known as the Z boson.

The conundrum of massive gauge bosons are eventually solved by a set of 1964 PRL symmetry breaking papers by Robert Brout, François Englert [29], Peter Higgs [30], Gerald Guralnik, C. Richard Hagen and Tom Kibble [31]. Those papers proposed the Higgs mechanism that offers a way to generate gauge boson mass terms while keeping the Lagrangian gauge invariant. Eventually in 1967, Steven Weinberg [32] and Abdus Salam applied the Higgs mechanism to Glashow's unified electroweak theory and formed the central piece of the Standard Model as we know today.

1.2 THE HIGGS SECTOR IN THE STANDARD MODEL

After the brief history on quantum field theory of the SM, we are in this section putting the ingredients together, while focusing on the theme of this thesis, the Higgs sector of the model. In the last section, the Lagrangian for the QED and QCD part of the theory are shown. Adding the Higgs sector and the unified electroweak interaction, the SM Lagrangian in its modern form consists of the following pieces,

$$\mathcal{L}_{\mathrm{SM}} = \mathcal{L}_{\mathrm{gauge}} + \mathcal{L}_{\mathrm{fermions}} + \mathcal{L}_{\mathrm{Higgs}} + \mathcal{L}_{\mathrm{Yukawa}}. \tag{1.5}$$

The central piece is the only fundamental scalar in the theory, the Higgs field, which gives rise to the mass terms of all other massive elementary particles in the theory.

The Higgs mechanism works as follows. The Higgs field part of the Lagrangian reads,

$$\mathcal{L}_{Higgs} = (D_\mu \Phi)^\dagger D_\mu \Phi + \mu^2 \Phi^\dagger \Phi - \lambda (\Phi^\dagger \Phi)^2. \tag{1.6}$$

The complex scalar field can be written as a $\mathrm{SU(2)_L}$ doublet,

$$\Phi = \begin{pmatrix} \phi^+ \\ \frac{v+H+i\phi_Z}{\sqrt{2}} \end{pmatrix}. \tag{1.7}$$

It contains an expectation value v that rises from its potential and will be explained later.

D_μ here is the covariant derivative under the $\mathrm{SU(2)_L \times U(1)_Y}$ symmetry group,

$$\begin{aligned} D_\mu &= \partial_\mu - i\frac{g}{2}W_\mu^a\sigma^a + ig'B_\mu Y \\ &= \partial_\mu - i\frac{g}{\sqrt{2}}(W_\mu^+\sigma^+ + W_\mu^-\sigma^-) - ieA_\mu Q - i\frac{g}{\cos\theta_W}Z_\mu(T_3 - \sin^2\theta_W Q). \end{aligned} \tag{1.8}$$

Here $\sigma^\pm = (\sigma_1 \pm i\sigma_2)/2$, with σ_i being the three Pauli matrices. The W_μ^a and B_μ fields are the gauge fields of the $\mathrm{SU(2)_L}$ and $U(1)_Y$ symmetry groups respectively, with g and g' as their coupling strength to the scalar field. Y is the U(1) charge of the scalar field Φ and it equals to 1/2 in our convention. The $W^\pm$, Z and A are the charged and neutral weak gauge bosons and the electromagnetic gauge boson (or photon) where

$$W_\mu^\pm = \frac{1}{\sqrt{2}}(W_\mu^1 \mp iW_\mu^2), \quad \begin{pmatrix} Z_\mu \\ A_\mu \end{pmatrix} = \begin{pmatrix} \cos\theta_W & -\sin\theta_W \\ \sin\theta_W & \cos\theta_W \end{pmatrix} \begin{pmatrix} W_\mu^3 \\ B_\mu \end{pmatrix}. \tag{1.9}$$

They become the physical gauge fields after the former three acquire masses from the symmetry breaking Higgs mechanism. Q represent the electromagnetic charges of the scalar field components and follow the relation $Q = T_3 + Y$. T_3 are eigenvalues of the scalar field under σ_3, and they equal to 1/2 and -1/2 for the upper and lower components of Φ. θ_W is called the Weinberg (weak) angel, which as defined above is the mixing angle to rotate from the unbroken basis $\{W_\mu^3,\ B_\mu\}$ to the physical fields $\{Z_\mu,\ A_\mu\}$. The coupling strength are related as

$$e = g\sin\theta_W = g'\cos\theta_W. \tag{1.10}$$

The μ in the positive quadratic term $\mu^2\Phi^\dagger\Phi$ sets an explicit mass scale in the theory. Together with the self coupling term $-\lambda(\Phi^\dagger\Phi)^2$, it shifts the vacuum expectation value (VEV) of the scalar field to a non-zero number $v = \frac{\mu}{\sqrt{\lambda}}$, which spontaneously breaks the $\mathrm{SU(2)_L \times U(1)_Y}$ gauge down to $U(1)_{EM}$. H here is the real physical Higgs field as a small perturbation around the VEV. As seen above, through the kinematic term of the scalar $(D_\mu\Phi)^\dagger D_\mu\Phi$, the vector bosons W^+, W^- and Z achieve their masses and couplings to the physical Higgs boson as the following,

$$M_W = \frac{gv}{2}, \quad g_{WWH} = \frac{g^2v}{2}; \qquad M_Z = \frac{gv}{2\cos\theta_W}, \quad g_{ZZH} = \frac{g^2v}{4\cos^2\theta_W}. \tag{1.11}$$

The fermion masses come from their Yukawa couplings with the Higgs which read,

$$\begin{aligned}\mathcal{L}_{\text{Yukawa}} &= -Y_\ell\ \overline{L}\ \Phi\ \ell_R - Y_d\ \overline{Q}\ \Phi\ d_R - Y_u\ \overline{Q}\ \tilde{\Phi}\ u_R + h.c. \\ &\supset -Y_\ell \frac{v+H}{\sqrt{2}}\ \overline{\psi}_\ell \psi_\ell - Y_q \frac{v+H}{\sqrt{2}}\ \overline{\psi}_q \psi_q.\end{aligned} \tag{1.12}$$

In the expressions above, the leptons and the Higgs fields are first expressed in terms of their $\mathrm{SU(2)_L}$ doublets $\{L,\, Q,\, \Phi\}$ and singlets $\{\ell_R,\ d_R\ , u_R\}$, where

$$L = \begin{pmatrix} \nu_\ell \\ L_\ell \end{pmatrix}, \quad Q = \begin{pmatrix} U \\ D \end{pmatrix} \tag{1.13}$$

for the leptons are quarks respectively. The summation over flavors are implicitly assumed. $\tilde{\Phi} = i\tau_2 \Phi^*$. The Y_i are the Yukawa coupling strength for each flavor. In the second line we retain only the terms in the scalar field involving the VEV and the physical Higgs field as $\frac{v+H}{\sqrt{2}}$, and the fermions as Dirac spinors for each flavor. The terms corresponding to the fermion masses and their couplings to the Higgs can be explicitly read off as,

$$m_f = \frac{y_f v}{\sqrt{2}}, \quad g_{f\bar{f}H} = \frac{y_f}{\sqrt{2}}. \tag{1.14}$$

The remaining massless particles in the standard model are two gauge bosons: the gluon that is not coupled to the scalar field, and the photon which remains unbroken by the VEV, and the neutrinos. They don't directly couple to the VEV. The photon and the gluon are nevertheless coupled to the Higgs through higher order corrections. In terms of Feynman diagrams, all the vertices between the Higgs and other SM particles are shown in Fig.1.

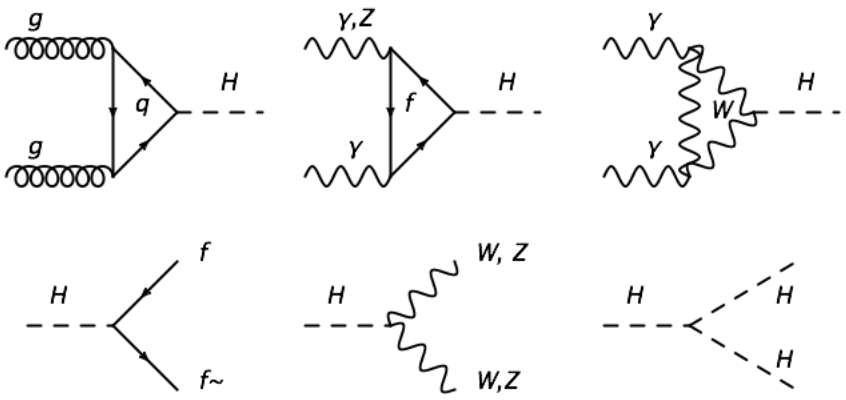

Figure 1: Vertices between the Higgs and other SM particles at lowest order in the SM.

1.3 HIGGS PROPERTIES AT COLLIDERS

The 125 GeV Higgs boson discovered at the LHC completes the roster of particles predicted by the Standard Model (SM). High-energy experiments now continue their search for physics beyond the Standard Model in light of this new era. A major new avenue for pursuing this search is the detailed study of the Higgs itself. While the mass of the Higgs boson is a free parameter in the SM, its couplings to other particles are dictated by the gauge and Yukawa interactions. The observations of this particle are so far consistent with the SM expectations, but there is considerable room for new physics to reveal itself in deviations of the Higgs properties from the SM. There are also many theoretical scenarios in which such deviations would arise at a potentially detectable level. A precise measurement of the Higgs couplings is a key tool in establishing a departure from the SM, and in characterizing any sign of new physics which may be discovered.

In the last section, we derived the particle masses and their tree level couplings to the Higgs from the SM Lagrangian. We now discuss the decay and production of the Higgs particle at colliders and the observables we measure. Given a 125 GeV Higgs, the mass spectra of other particles and their couplings, we can calculate the decay spectrum of the Higgs. The total decay width and the important decay channels with their corresponding

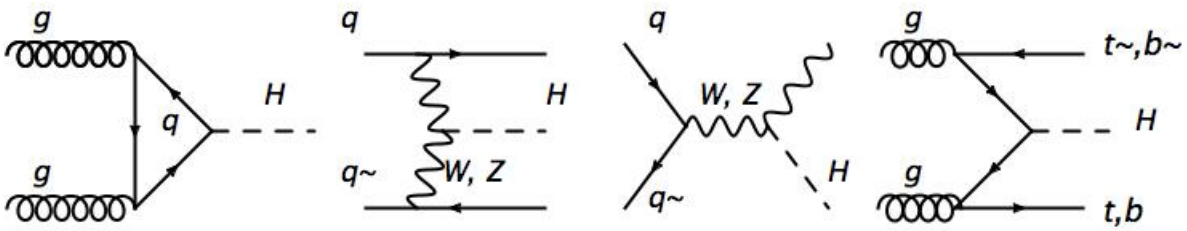

Figure 2: Main Higgs production mechanisms at the LHC.

branching ratios (BR) are quoted below from Ref. [137]:

$$
\begin{aligned}
&\Gamma_{\text{tot}} = 4.08(8)\ \text{MeV}, \\
&\text{BR}(h \to b\bar{b}) = 58.2\%, \quad \text{BR}(h \to c\bar{c}) = 2.89\%, \quad \text{BR}(h \to u\bar{u}, d\bar{d}, s\bar{s}) < 0.03\%, \\
&\text{BR}(h \to \tau^+\tau^-) = 6.27\%, \quad \text{BR}(h \to \mu^+\mu^-) = 0.02\%, \\
&\text{BR}(h \to gg) = 8.18\%, \quad \text{BR}(h \to \gamma\gamma) = 0.23\%, \quad \text{BR}(h \to Z\gamma) < 0.15\%, \\
&\text{BR}(h \to WW^*) = 21.4\%, \quad \text{BR}(h \to ZZ^*) = 2.62\%.
\end{aligned}
\tag{1.15}
$$

As shown above, more than half the time the Higgs decays to a $b\bar{b}$ pair. Next up is the WW^* channel where the W boson further decays leptonically or hadronically.

At the LHC, the Higgs are produced through four dominant mechanisms. They are, ordered by decreasing total signal rates, the gluon-gluon fusion (ggF), the vector boson fusion (VBF), the associated production with vector boson (VH) and the associated production with quark pairs ($b\bar{b}H, t\bar{t}H$). The Feynman diagrams are presented in Fig. 2. The signal of Higgs production is reconstructed through the invariant mass peak of its decay final states. Given a narrow width approximation (NWA), we can thus write down the schematic cross section of the Higgs signal at the LHC as [48]

$$
\sigma_{i \to H \to f} \propto \frac{g_i^2 g_f^2}{\Gamma_H}. \tag{1.16}
$$

The $g_{i,f}$ stands for the Higgs coupling to the SM particle at the production and decay side respectively. From the expression it's clear that the on-resonance Higgs cross section measured this way is degenerate under a simultaneous rescaling of the couplings and the Higgs

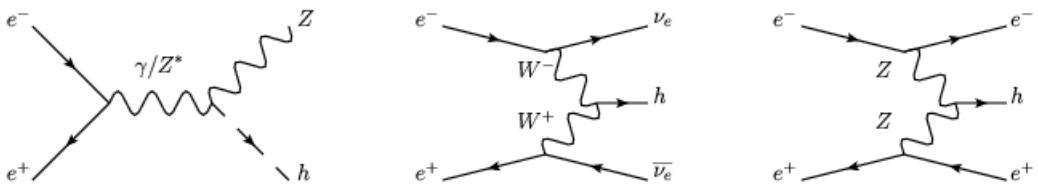

Figure 3: Main Higgs production mechanisms at the ILC.

total width. The measurements are thus insensitive to certain directions in the parameter space. Because it cannot measure a single coupling independent of the width, it cannot place strong bounds on the absolute values of couplings, nor on the total width unless additional, model-dependent, assumptions are made [33, 34, 35, 36, 37, 38]. Interference effects can be used to bound the width at a few times its SM value [39, 40, 41, 42, 43, 44, 45, 46, 47]. The other challenge that is intrinsic to hadron colliders is the uncertainty of large QCD-related backgrounds. Thus the signal of the type where the Higgs decay to quarks or gluons which further hadronize back to jets, is overwhelmed by the large QCD background and has little hope to be detected by the LHC. These signals are crucial for testing Yukawa couplings between the Higgs and quarks, and Higgs to gluon indirect couplings at the decay side. Studies making use of several production channels[155, 124, 122], boosted kinematics[130, 148] and jet substructure[144, 145, 146] are proposed to realize the measurements at the LHC.

At a lepton collider such as the proposed International Linear Collider (ILC)[127], the Future Circular Collider (FCC-ee)[128], or the Electron Position Collider (CEPC)[129] etc., the Higgs is produced dominantly by ZH associated production at a center of mass energy ($\sqrt{s}$) of around 250 GeV. The other important production channels include the WW fusion and ZZ fusion channels whose production rates rise with the center of mass energy $\sqrt{s}$ logarithmically. The Feynman diagrams are shown below in Fig. 3. At a lepton collider, since we have full knowledge of the parton level initial states, the on-resonance Higgs signal can be reconstructed from the recoil mass peak of its byproduct, in addition to its decay. The recoil mass reconstruction of the Higgs allows us to measure the Higgs production rate inclusively.

The inclusive cross section of the Higgs production thus takes the form of

$$\sigma^{inc} \propto g_Z^2. \tag{1.17}$$

This breaks the degeneracy between the Higgs couplings and its total width in the observable, which is unavoidable when reconstructing the Higgs resonance peak from its decay. Instead, it allows a direct determination of the individual coupling strengths, and an accurate extraction of the Higgs total width in a more model-independent manner. The lepton collider also offers a relatively QCD-background free environment to help measure the Higgs to light jets decay precisely. A summary of Higgs studies at linear colliders can be found in this white paper [127].

1.4 STATUS OF HIGGS MEASUREMENTS

The SM was experimentally established (2012), with the discovery of the Higgs boson at 125 GeV, at the Large Hadron Collider (LHC).

As we know for the Higgs detection at the LHC, $\gamma\gamma$ and ZZ were the discovery channels for the Standard Model (SM)-like Higgs boson (h) [117, 118]. Next came the WW decay channel, all have been measured with more than 5σ significance at Run I by both experiments ATLAS [119] and CMS [120]. While the ZZ, WW channels are tree-level processes, most directly related to the electroweak symmetry breaking (EWSB) with the coupling strength proportional to $M_{W,Z} \sim gv$, the Higgs coupling to the top quark is best inferred from its contribution to the production $gg \to h$ and the decay $h \to \gamma\gamma$ with a fitted accuracy of around 30% [121]. A direct measurement from Higgs and top associated production is yet to be established [122, 123]. For the lepton side, the challenging decay channel $h \to \tau^+\tau^-$ has also reached 5σ observation with a combined analysis of the two experiments [121]. With the upgrade of LHC to its higher center of mass energy at Run II and more accumulated data, the difficult mode $h \to b\bar{b}$ is expected to reach 5σ soon after several hundreds fb^{-1} at 14 TeV [124]. Thus, the Higgs couplings to the heaviest generation of fermions will soon be

settled to the values expected from the Standard Model (SM) prediction at an accuracy of about 20% [125], and verifying the pattern of non-universal Yukawa couplings.

We next consider the LHC upgrade to a total integrated luminosity of 3000 fb^{-1} at 14 TeV (HL-LHC). While the precision measurements of those couplings will continue in the LHC experiments, it is imperative to seek other "rare decay" channels, in the hope of uncovering any deviations from the SM. Among the rare channels, it is perhaps most promising to observe the clean mode $gg \to h \to \mu^+\mu^-$ [126], despite the small decay branching fraction $\mathrm{BR}(h \to \mu^+\mu^-) \sim 2 \times 10^{-4}$. A 5σ observation may be conceivable at the end of the run for HL-LHC with 3000 fb^{-1} [125], which would be of significant importance to establish the pattern of the Yukawa couplings by including a second generation fermion. For the other hadronic channels, it would be extremely challenging to make any measurements at the LHC due to the overwhelmingly large QCD backgrounds [3]

The most promising production mechanism for the hadronic decay signal of the Higgs boson is

$$pp \to Vh, \quad \text{where} \quad V = W^{\pm},\ Z. \tag{1.18}$$

With W/Z decaying leptonically to serve as effective triggers, the Higgs signal may be detected from the construction of its invariant mass of the hadronic products. To sufficiently suppress the large QCD backgrounds, it was proposed [130] to look for highly-boosted events for $h \to b\bar{b}$ against the leptonic W/Z. Studies on these processes at HL-LHC shows a $\approx 20\sigma$ (9σ) significance for the signal $Vh, h \to b\bar{b}$, with statistical (systematic added) uncertainty estimated [124]. Marching to the channel involving the second generation quarks, the sensitivity to $Vh, h \to c\bar{c}$ is significantly worse. Bounds are extrapolated in a recast study in Ref. [131] to be ~ 6.5 times the SM value (statistic errors assumed only). This is expected, given that $\mathrm{BR}(h \to b\bar{b})$ is ~ 20 times larger than $\mathrm{BR}(h \to c\bar{c})$, that expected b-tagging is twice as efficient as c-tagging, and that the dominant background $Vbb(cc)$ in the relevant kinematic region is about the same order. An interesting proposal to search for $h \to J/\psi + \gamma$

[3] As mentioned in the previous section, due to the much cleaner experimental environment, a lepton collider such as International Linear Collider (ILC) [127] or a circular e^+e^- collider [128, 129], running at the Zh threshold or higher energies, will give us much better sensitivity to the hadronic decays of the Higgs. The expected accuracy on $h \to gg$ and $h \to c\bar{c}$ will be 7% (2.3%) and 8.3% (3.1%) respectively, with the 250 GeV (1TeV) mission [127].

[132] does not seem to increase the observability for $hc\bar{c}$ coupling due to too low an event rate [133, 134]. Another study on $h + c$ associated production estimates a bound of order one on the SM charm Yukawa coupling at the end of the HL-LHC run [135]. A recent study on $h \to c\bar{c}\gamma$ shows comparable sensitivity on the charm Yukawa coupling [136].

It is natural to ask to what extent one would be able to search for other hadronic decays of the Higgs boson. As quoted above the updated calculations of the branching fractions for the 125 GeV Higgs boson decay hadronically in the SM [137], we can see that while the decay rates to light quarks predicted in the SM would be too small to be observable, the decay to a pair of gluons, mediated via the heavy top quark, will be nearly three times larger than the $c\bar{c}$ channel. The experimental signatures for those channels would be to search for the un-tagged light jet pairs jj, which form a mass peak near the Higgs boson mass m_h. The lack of a heavy-flavor tag makes background suppression difficult. The event sample gets "contamination" as well from mis-tagged events of the leading decay $h \to b\bar{b}$ and $c\bar{c}$. The individual event samples need to be correlatively quantified and treated. Together with $h \to b\bar{b}$ and $h \to c\bar{c}$ studies, the un-tagged channel puts an independent dimension of bound in the space of branching ratios of Higgs decays to quarks and gluons. It is also an expected Higgs signal from the decay side of the resonance that can be looked for and verified by the end of HL-LHC run. Furthermore, assuming a well measured ggh coupling at the end of HL-LHC [125], the result puts comparable but independent constraints on the light-quark Yukawa couplings.

2.0 HIGGS PRODUCTION THROUGH ZZ FUSION IN E^+E^- COLLISIONS

One key feature of a lepton collider in making model-independent measurements is the ability to determine the inclusive Higgs production rate. This is done using processes such as $e^-e^+ \to h + X$ where X represents additional measurable particles. Since the initial state, including longitudinal momentum, is well known we can infer the Higgs 4-momentum without specifying the decay of the Higgs,

$$p_h = p_{e^-e^+} - p_X. \tag{2.1}$$

This complete kinematical reconstruction allows us to discriminate the inclusive Higgs on-shell signal from background and measure the couplings of the relevant production mechanism independently of the width. Once this is done, measurements of additional specific decay channels can be used to determine the total width and the absolute values of other couplings. In a previous study we discussed this general strategy in detail [48]. Based on available analyses the model-independent Higgs width Γ_h can be measured at the level of $\delta_{\Gamma_h} \simeq 5\%$ relative to the true width. Most of this error derives from the uncertainty on the inclusive cross section. Thus, any substantial improvement of the total width measurement depends critically on improving the precision of the inclusive cross section. Currently, the inclusive cross section sensitivity is estimated for the "Higgsstrahlung" channel $e^-e^+ \to Zh$. The cross section for this channel is largest just above the threshold at a center-of-mass energy $\sqrt{s} \simeq 250$ GeV, where it can be measured using the Z decay to electrons and muons with a relative error $\delta\sigma^{\rm inc}_{Zh} \simeq 2.6\%$ [49, 50]. At $\sqrt{s} = 500$ GeV the Higgsstrahlung rate is substantially reduced but using hadronic decays of the Z may allow one to measure the cross section at $\delta\sigma^{\rm inc}_{Zh} \simeq 3\%$ [51].

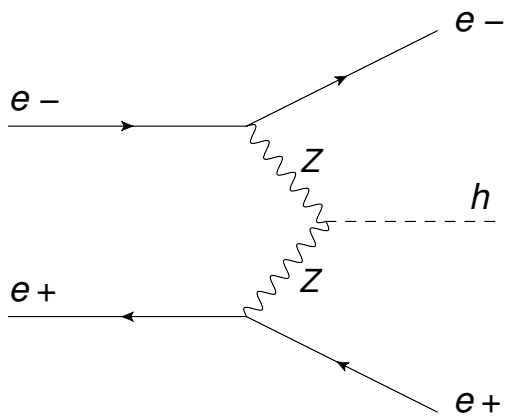

Figure 4: Feynman diagram of the ZZ fusion signal process

Further improvements can be made by examining the alternate production mechanism of ZZ fusion [52, 53]

$$e^-e^+ \to e^-e^+Z^*Z^* \to e^-e^+h, \tag{2.2}$$

as depicted in Fig. 4, which has often been neglected in the literature. This mode has a small rate at 250 GeV but grows with energy as $\ln^2(s/M_Z^2)$. At 500 GeV it already contributes roughly twice as much to the final state e^-e^+h as the Higgsstrahlung process $Zh \to e^-e^+h$, which falls roughly as $1/s^2$, as can be seen as the dashed curve in Fig. 5. At 1 TeV this ratio grows to almost a factor of 20. Thus, although the Higgsstrahlung process benefits from a sharp kinematic on-shell Z peak through the reconstructible final states into which the Z decays, the ZZ fusion channel, which features two energetic forward/backward electrons, should also be exploited to make maximal use of the high-energy reach of the ILC.

In this work we perform a fast detector simulation analysis of the inclusive ZZ fusion channel measurement at 500 GeV and 1 TeV. We simulate the predominant backgrounds and a SM-like Higgs signal and calculate the signal sensitivity using a cut-based analysis and multivariate log-likelihood analysis. We find that with the cut-based analysis, we can reach a sensitivity on the cross section to the 2.9% level. The multivariate analysis further improves the precision of the cross section measurement to 2.3%.

The rest of the chapter is organized as follows: In Sec. 2.1, we discuss the kinematic

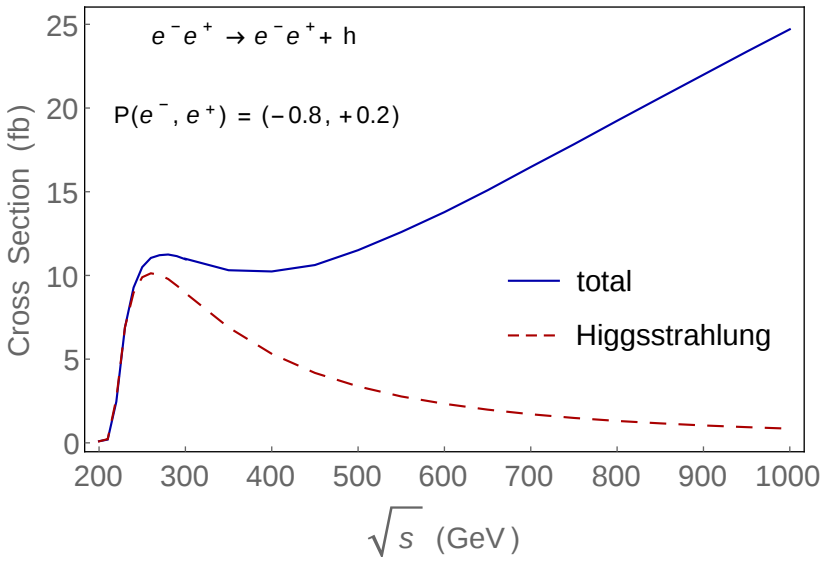

Figure 5: Total cross section (in fb) for $e^-e^+ \to e^-e^+ + h$ versus $\sqrt{s}$.

features for identifying the signal and perform a detailed analyses for the ZZ fusion process at 500 GeV and 1 TeV energies including backgrounds. In Sec. 2.2 we discuss the effects of this additional information on the model-independent Higgs width and couplings. We also illustrate the potential use of these couplings in constraining higher-dimensional operators. We summarize our results in Sec. 2.3. An appendix is included to address issues relating to potential signal and backgrounds with a single photon in the final state.

2.1 SENSITIVITY ANALYSIS

We consider the signal process $e^-e^+ \to e^-e^+h$ via ZZ fusion as in Eq. (2.2). We assume that the incoming leptons are described by the nominal beam energy moving along the beam axis in the positive and negative directions respectively. Then the outgoing electrons are each characterized by a three-dimensional vector and there are six independent degrees of freedom measured in our final state. We choose the dimensionful variables to be the invariant mass

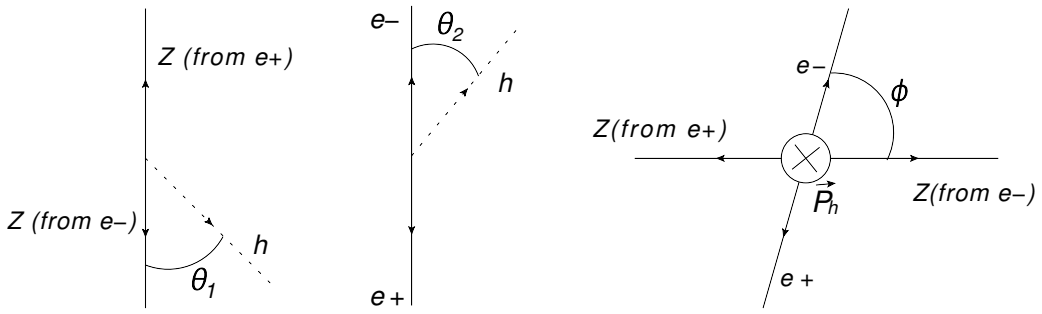

Figure 6: Angles θ_1, θ_2 and ϕ as defined in the text.

of the final electron-positron pair m_{ee} and the recoil mass, given by

$$m^2_{rec} \equiv s - 2\sqrt{s}E_{ee} + m^2_{ee}. \tag{2.3}$$

The recoil mass provides the most distinct signal feature since it displays the resonance peak at the Higgs mass $m_h \simeq 126$ GeV observable on top of a continuum background. The electron-pair mass m_{ee} favors a large value $m_{ee} \gtrsim 250$ (600) GeV at a 500 (1000) GeV center-of-mass energy. This is distinct from the Higgsstrahlung mode where the pair mass is strongly peaked at the Z resonance. Despite a broad distribution for the ee pair mass in the ZZ fusion, it still provides some discriminating power against the diffuse electron background.

The remaining kinematic degrees of freedom can be described by four angles. One of these, the azimuthal angle of the Higgs boson around the beam axis, is irrelevant to our analysis due to the rotational symmetry of the initial state around the beam line when the beam is not transversely polarized. The other three angles are illustrated in Fig. 6, where the label e^- (e^+) represents the outgoing electron (positron) and the Z momentum is given by the difference between outgoing and incoming electrons (positrons). The arrows represent momentum directions. The Higgs momentum is perpendicular to the plane in the right panel. The angles are chosen as follows: θ_1 is the angle between the intermediate Z coming from the initial electron and the Higgs boost direction in the rest frame of the Higgs. θ_2 is the angle between the final state electron and the Higgs boost direction in

the rest frame of the outgoing e^-e^+ pair. These angles take advantage of the scalar nature of the Higgs. The distributions for $\cos\theta_1$ and $\cos\theta_2$ are rather flat since the Higgs boost direction has no preference to align with the spins of the incoming Zs or outgoing electrons. There is some correlation between these two angles and mild enhancement at larger $|\cos\theta|$, which corresponds to a more collinear configuration. This is mitigated by the relatively large virtuality of the Z propagators. In contrast the most important backgrounds show much stronger correlation and peaks at high $|\cos\theta|$ arising from highly collinear regions of phase space which tend to dominate their production. The third variable, ϕ, is defined as the angle between the plane defined by the ZZ pair and the plane defined by the outgoing e^-e^+ pair when viewed along the Higgs boost direction. It is a measure of coplanarity. Here the signal shows a preference for small values of ϕ, indicating coplanar emission of the outgoing e^-e^+ pair with the Z propagators and with the incoming leptons. This strong correlation is expected since the Higgs does not carry away any spin information. The backgrounds will generally have a more complex spin structure which is not strongly coplanar.

In practice, the outgoing electrons of our signal will tend to radiate photons, an effect we treat with showering. This radiation degrades our signal resolution. To ameliorate this, nearby photons are clustered according to a recombination algorithm and identified with a single electron as described in detail in the next section.

Given our inclusive signal process, the backgrounds are of the form $e^-e^+ \to e^-e^+X$. Obviously, the single photon radiation $X = \gamma$ arising from the Bhabha scattering is by far the largest. Although the majority of events should be removed by the requirement of a large recoil mass m_X, beamstrahlung and the effects of the initial-state radiation (ISR), as well as the final-state radiation (FSR), will produce additional largely collinear photons. This generates a long tail in the recoil mass spectrum due to unobserved photons, mainly along the beam pipe. To keep this class of backgrounds under control, we introduce a cut on the transverse momentum p_T of the outgoing e^-e^+ pair. Photons which are lost down the beam pipe should only contribute small p_T differences to the observed final state. Thus the final state e^-e^+ intrinsically has no p_T as long as collinear photons from final-state showering are correctly regrouped with the electrons. The signal, in contrast, has a nonzero p_T from the recoiling Higgs.

Cuts (fb)	Generator level	$m_{\rm rec},\ m_{ee}$	$p_{T(ee)}$	Veto isolated single γ
e^-e^+h (500 GeV)	11.5	4.11	3.48	3.48
$e^-e^+\gamma$ (500 GeV)	165000	317	67.2	1.32
e^-e^+h (1 TeV)	24.1	9.75	8.49	8.18
$e^-e^+\gamma$ (1 TeV)	175000	1570	344	4.73

Table 1: Cross section (fb) for signal e^-e^++h and background $e^-e^+\gamma$ after sequence of cuts.

This leaves a background from $e^-e^+\gamma$ where the extra photon is not close enough to either electron to be grouped with it by the clustering algorithm. We find it most convenient to simply veto events, in addition to the e^-e^+ pair, with a single isolated photon

$$E_\gamma > 10\ \text{GeV}, \quad \theta_\gamma > 6^\circ, \tag{2.4}$$

where θ_γ is the polar angle with respect to the beam. The effectiveness of this cut is illustrated in Table 1 for the 500 GeV and 1 TeV runs. The cuts are specified in Table 2 and Table 4 for the 500 GeV and 1 TeV case respectively. Simple cuts on invariant mass and p_T reduce the $e^-e^+\gamma$-induced background by 3 orders of magnitude but it remains 30 times larger than our signal. However the single photon veto reduces this by more than 90%.

In principle this affects our inclusiveness. However, the Standard Model processes which could produce such a signal, such as $h \to \gamma\gamma$ (where one photon is lost down the beam pipe) and $h \to Z\gamma$, constitute branching fractions of 2.3×10^{-3} and 1.6×10^{-3} respectively. As will be seen, the ultimate precision for the inclusive Higgs production measurement is at the $\sim 2\%$ level so that Higgs decays to $\gamma\gamma$ or $Z\gamma$ would have to be enhanced by more than an order of magnitude compared to the Standard Model to be seen in the model-independent inclusive measurement. Any such large signal enhancements will be seen at the LHC, to the extent that they are not already excluded by current results. See the Appendix for further discussion.

After these cuts some background can remain due to poorly measured final-state particles. Particularly at 1 TeV center-of-mass energies, errors on the detected momentum of the final

state can sometimes fake a recoil mass and a high p_T that passes our other cuts. This is necessarily an issue to be determined in detail by experimentalists when working with an actual machine and is only parameterized by assumptions on detector smearing and efficiency in our simulation. We find that badly measured states are typically associated with very high-energy photons. Either these photons are not detected at all due to imperfect calorimeter efficiency, or they are reported but with significant error on their transverse momenta. Mismeasured low-energy photons will not usually cause a big enough error to satisfy our previous cuts. Thus it is useful to veto events with very high-energy detected photons, which are relatively rare in the signal.

Again, one may worry about introducing a bias against photons from Higgs decay, but this problem can be addressed. When an event has a high-energy photon we first boost it into the rest frame of the Higgs, as determined by the momentum of the outgoing lepton pair. If the photon's energy in the Higgs frame is less than half the Higgs mass, then it potentially comes from a Higgs decay, and we do not subject it to the high-energy veto. Thus only events with "eligible" photons, γ^*, which could not have come from the Higgs decay, are cut.

2.1.1 Simulation framework

To estimate the expected number of events and derive the sensitivity reach at a given energy and luminosity we use the ILC WHIZARD setup provided through the detector simulation package SGV3 [116]. Beam profiles for several energies have been generated by GuineaPIG [55], which includes effects from beamstrahlung and ISR. These profiles are interfaced with WHIZARD 1.95 [56] to generate parton-level samples. The parton-level samples are then passed to PYTHIA which performs showering and hadronization to final-state particles [142]. SGV is a fast detector simulation which has been found to agree well with full simulation results.

To avoid collinear and soft divergences, at the parton level we require that the energy of a final state photon be greater than 10 GeV, and that the invariant masses of final lepton-antilepton pairs and of lepton-photon pairs be greater than 4 GeV. We also require that the

invariant mass of a final-state (anti)electron with an initial (anti)electron, or of a final photon with an initial lepton, be greater than 4 GeV. More collinear photons will be generated via the showering routines in PYTHIA.

After simulating tracking and calorimeter hits, SGV attempts to identify charged and neutral particles and groups these into jetlike objects according to a sequential recombination algorithm. We use the JADE algorithm, which defines a distance between objects

$$y_{ij} \equiv \frac{2E_iE_j(1-\cos\theta_{ij})}{E_{\rm vis}^2}, \tag{2.5}$$

where E_i and E_j are the energies of two objects and $E_{\rm vis}$ is the total seen energy of the event. Nearby objects are merged into subjets until all subjets are separated by $y_{ij} > 0.01$.

In selecting our observables we first identify the two highest-energy electron/positron tracks in an event and discard it if there are fewer than two detected (anti)electrons. We also require that these particles have opposite signs. If nearby calorimeter hits included in the subjet which contains the track are only identified as photons, then we use the jet momentum and energy for our reconstructed lepton. If the subjet contains any particles identified as hadrons then we use only the track momentum in order to minimize cases where hadron jets overlap with the recoiling electrons. For the purposes of the isolated photon cut described above, we define an isolated photon as a jet object which contains only photons and no charged tracks or hadronic calorimeter hits.

In the case of pure photon plus electron/positron backgrounds we simulate both $e^-e^+ \to e^-e^+\gamma$ and $e^-e^+ \to e^-e^+\gamma\gamma$ at the matrix element level. After showering there is some overlap in the signals described by these two processes. In the spirit of matching calculations done for hadron colliders we discard events from $e^-e^+ \to e^-e^+\gamma$ which produce two isolated photons after the clustering procedure.

2.1.2 500 GeV analysis

We proceed with a sensitivity analysis for the ILC running at a 500 GeV center-of-mass energy. We apply an initial beam polarization of -0.8 for the electron and $+0.3$ for the positron, following the ILC technical design report [58]. We first perform a purely cut-based

Cut 1	$122\ \text{GeV} < m_{\text{rec}} < 145\ \text{GeV}$ $110\ \text{GeV} < m_{ee} < 370\ \text{GeV}$ $p_{T(ee)} > 40\ \text{GeV}$ veto 1 isolated photon $E^*_\gamma < 200\ \text{GeV}$
Cut 2	$\phi < 1.5$

Table 2: Cuts applied at ILC 500 GeV.

analysis with the cuts listed in Table 2. E^*_γ represents only photon hits with energy greater than 65 GeV in the rest frame of the Higgs.

Figure 7 displays the signal and background distributions in m_{rec}, m_{ee} and the three angular variables, after applying Cut 1 as listed. As can be seen, the angular variables show considerable distinction from the background which can be used to enhance our sensitivity. Cut 2 acts on these angles.

For this analysis we define the signal sensitivity according to the statistical 1σ relative error on the signal,

$$\frac{\delta\sigma}{\sigma} = \frac{\sqrt{N_s + N_b}}{N_s}, \tag{2.6}$$

where $N_{s,b} = L\sigma_{s,b}$ are the expected number of signal and background events after cuts respectively. We assume the integrated luminosity $L = 500\ \text{fb}^{-1}$ at this energy. The statistical significance is then inversely related to the signal sensitivity as $N_s/\sqrt{N_s + N_b}$. The effect of our cuts on the cross section for signal and background processes is given in Table 3.

We find that this cut-based analysis can measure the inclusive ZZ fusion signal to a relative error of 8%. At this energy the dominant background after our cuts is $e^-e^+\nu_e\bar{\nu_e}$, over 80% of which is from the process $e^-e^+ \to W^-W^+$. The large cross section of $e^-e^+ \to W^-W^+$ is favored by the beam polarization we have used at 500 GeV ILC. It is possible to reduce this background with a polarization that favors right-handed electrons; however, this also reduces the signal and we do not find any significant gain in sensitivity with the

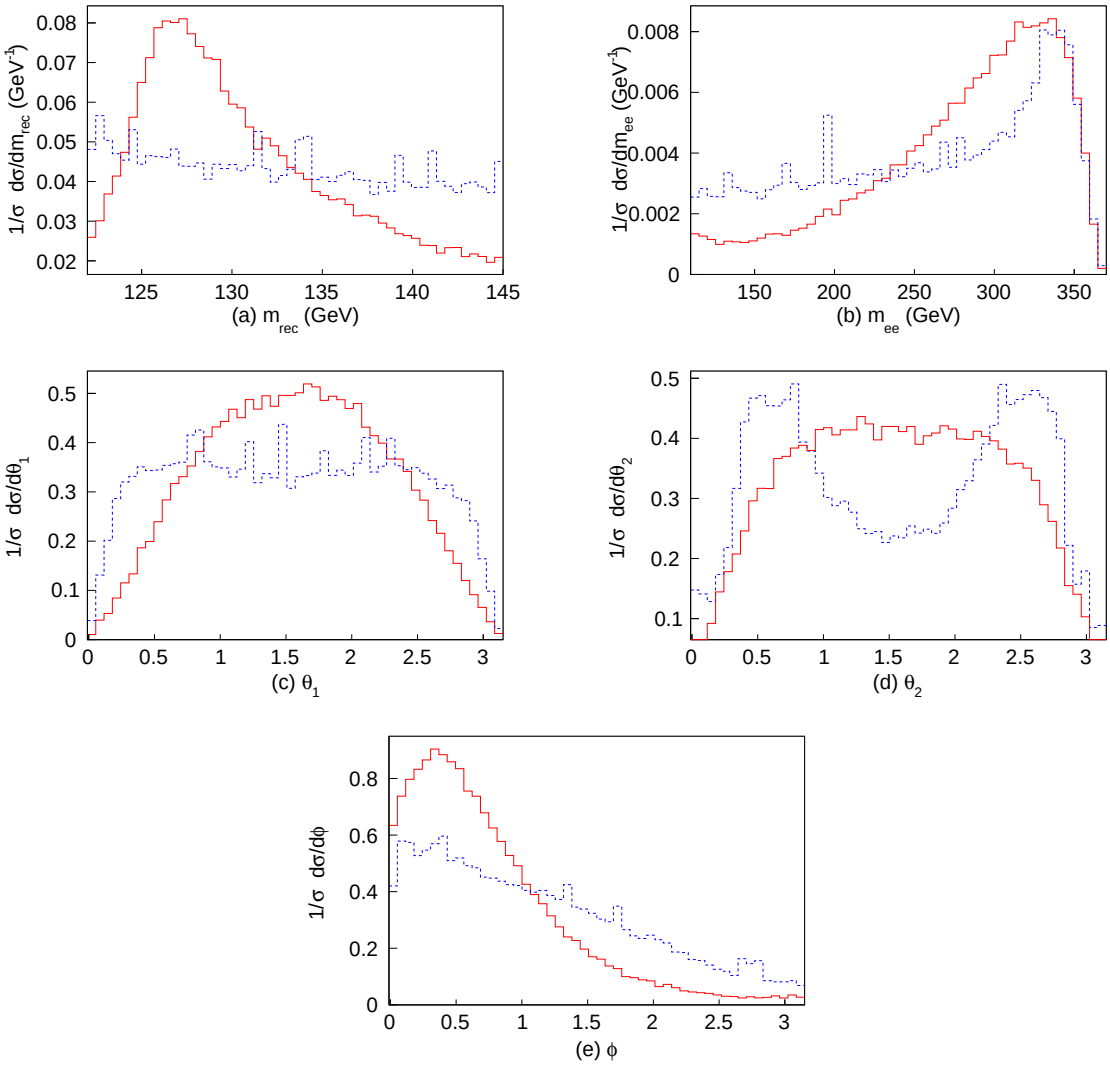

Figure 7: Comparison of signal (solid red) and total background (dashed blue) distributions for variables (a) m_{rec}, (b) m_{ee}, (c) θ_1, (d) θ_2 and (e) ϕ at $\sqrt{s} = 500$ GeV. Cut 1 in Table 2 is applied. For clarity, both signal and background distributions are normalized to unity.

Process	Generator level (fb)	Cut 1 (fb)	Cut 2 (fb)
$ee \to eeh$(Signal)	11.5	3.48	3.11
$ee \to ee\nu_e\nu_e$	659	23.9	16.0
$ee \to ee\nu_{\mu,\tau}\nu_{\mu,\tau}$	78.6	1.02	0.70
$ee \to eeqq$	1850	9.33	6.88
$ee \to eell$	4420	5.18	4.42
$ee \to ee\gamma\gamma$	1640	1.18	0.60
$ee \to ee\gamma$	165 000	1.32	0.66
Total background	174 000	41.9	29.2
$\delta\sigma/\sigma$	$\cdots$	8.7%	8.2%

Table 3: Cross sections for signal and background processes at ILC 500 GeV.

reversed polarization. It is possible to enhance sensitivity with an analysis that is sensitive to shape and to correlations between variables. This is particularly useful when the signal and background display distinct features which are not sharp enough to be efficiently cut on, as in Fig. 7.

2.1.3 1-TeV analysis

We next extend our analysis to a 1 TeV center-of-mass energy with 1000 fb^{-1} integrated luminosity. The polarization is assumed to be $(-0.8,\ +0.2)$ as suggested by the Snowmass Higgs report [59]. The ZZ fusion process is enhanced with increased center-of-mass energy. However, due to radiation from the energetic e^- and e^+, the Higgs mass peak in the $m_{\rm rec}$ distribution is much more smeared than in the 500 GeV case, and photon radiation backgrounds become more significant. The angular variables θ_2 and ϕ show greater distinctions between signal and background. To maximize significance we apply cuts as listed in Table 4.

Figure 8 compares the signal and total background distributions after Cut 1. Table 5 shows the expected cross sections after Cut 1 and Cut 2. Despite the degradation of the

Cut 1	$95\ \text{GeV} < m_{\text{rec}} < 300\ \text{GeV}$
	$500\ \text{GeV} < m_{ee} < 870\ \text{GeV}$
	$p_{T(ee)} > 50\ \text{GeV}$
	veto 1 isolated photon
	$E^*_\gamma < 200\ \text{GeV}$
Cut 2	$0.14 < \theta_2 < 3.0$
	$\phi < 1.5$

Table 4: Cuts applied at ILC 1 TeV.

recoil mass peak we gain significance from enhanced statistics and a somewhat improved signal-to-background ratio. The cut-based analysis can reach a sensitivity of 3.1%.

2.1.4 Multivariate log-likelihood analyses

To improve upon the cut-based results for reaching the optimal sensitivity, we perform a multivariate analysis (MVA) by evaluating a five-dimensional log-likelihood as a function of the deviation from the SM. Assuming Poisson statistics in each bin, the log-likelihood is defined as

$$LL(\mathbf{n};\boldsymbol{\nu}) = 2\sum_{i=1}^{N_{\text{bins}}}[\ n_i\ ln(\frac{n_i}{\nu_i}) + \nu_i - n_i] \tag{2.7}$$

where ν_i is the expected number of events in bin i for the SM signal plus background, and n_i is the number of events in bin i for the SM signal scaled by factor r (signal $\times$ r) plus background. We evaluate the region around $r = 1$ and our 1σ deviation from the Standard Model value corresponds to $\Delta LL = 1$.

Rather than applying Cut 2 on the angular distributions, we apply Cut 1 and evaluate the log-likelihood in the five dimensional phase space defined by the variables m_{rec}, m_{ee}, θ_1, θ_2, and ϕ. In the analysis, we perform a 3125-bin analysis by dividing the phase space along each variable evenly into five bins. Figure 9 shows the log likelihood as a function of r. In the 500 GeV analysis, we find the sensitivity on signal cross section improved to 6.0%. For

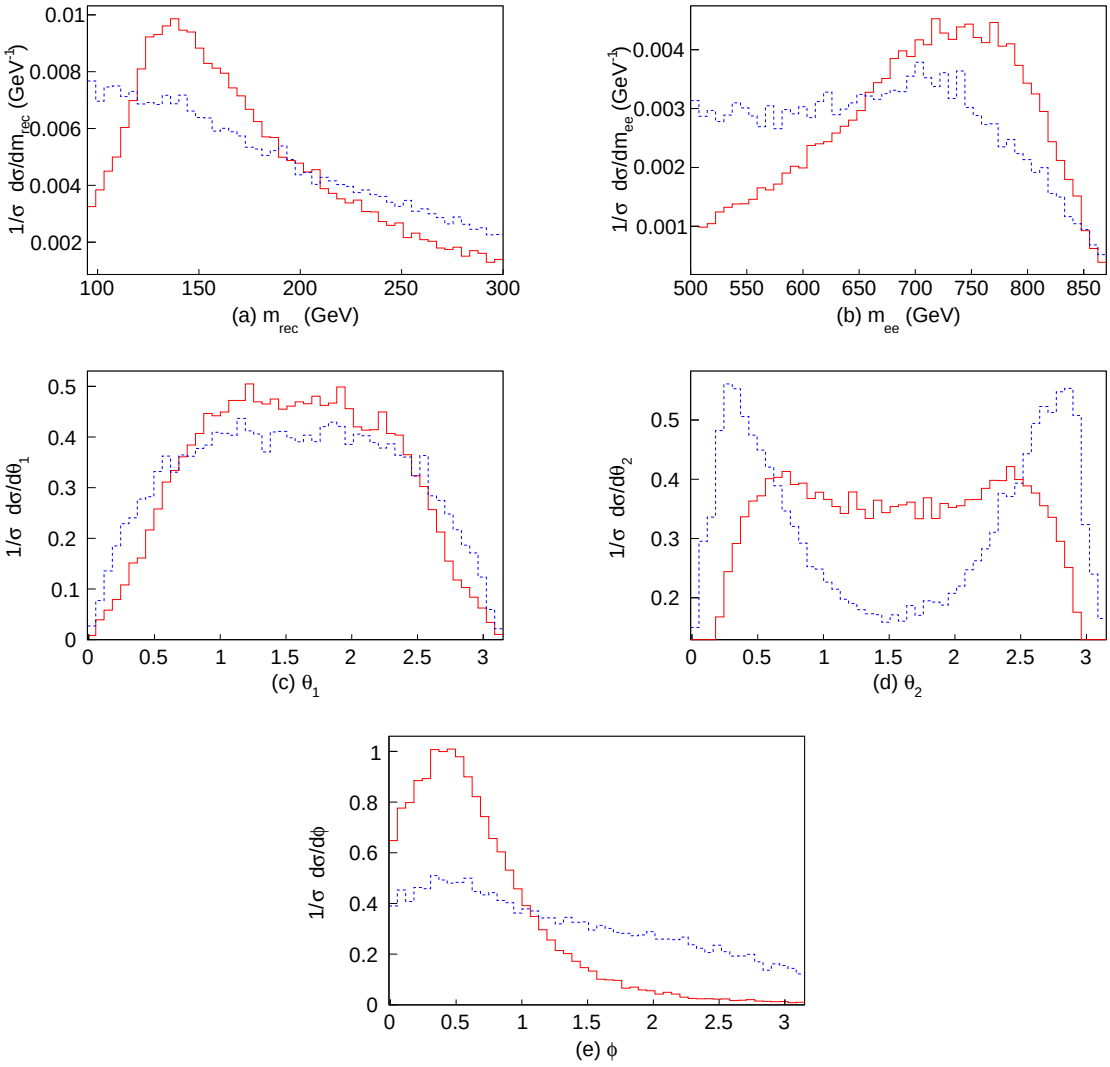

Figure 8: Comparison of signal (solid red) and total background (dashed blue) distributions for variables $m_{\rm rec}$, m_{ee}, θ_1, θ_2 and ϕ at $\sqrt{s} = 1$ TeV. Cut 1 in Table 4 is applied. For clarity, both signal and background distributions are normalized to unity.

Process	Generator level (fb)	Cut 1(fb)	Cut 2(fb)
$ee \to eeh$(Signal)	24.1	8.18	7.52
$ee \to ee\nu_e\nu_e$	978	31.5	17.2
$ee \to ee\nu_{\mu,\tau}\nu_{\mu,\tau}$	93.9	3.24	1.64
$ee \to eeqq$	2830	24.1	13.6
$ee \to eell$	6690	13.7	10.8
$ee \to ee\gamma\gamma$	3180	2.68	1.10
$ee \to ee\gamma$	175 000	4.73	2.28
Total background	189 000	80.0	46.6
$\delta\sigma/\sigma$	$\cdots$	3.6%	3.1%

Table 5: Cross sections for signal and background processes at ILC 1 TeV with 1000 fb^{-1} of integrated luminosity.

the 1 TeV case, the multivariate analysis increases the sensitivity to 2.5%. The likelihood profile for the 500 GeV (1 TeV) case is shown in the left (right) panel of Fig. 9.

2.2 IMPACT ON HIGGS PHYSICS

2.2.1 Higgs width and coupling Fits

Based on our results, the sensitivities on σ_z^{inc} which can be reached by studying the ZZ fusion channel at 500 GeV and 1 TeV ILC are 6.0% (8.2%) and 2.5% (3.1%) based upon MVA (cut-based) analyses, respectively. In combination this yields a 2.3% (2.9%) combined uncertainty on σ_z^{inc} from this production mode.

This is comparable to the current estimated precision of the ILC from studies of Zh associate production [51] (that is, σ_z^{inc} of 2.0% achieved by combining 2.6% and 3.0% uncertainties from 250 GeV and 500 GeV [60]). Thus, by combining the ZZ fusion and Zh measurements

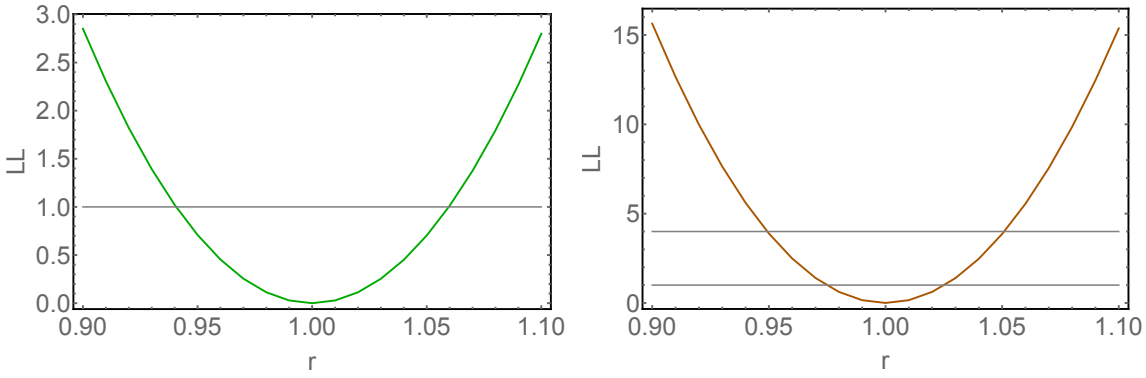

Figure 9: Five-dimensional Log likelihood as a function of the relative cross section r defined below Eq. (2.7) for the 500 GeV case (left) and the 1 TeV case (right). For both analyses, Cut 1 is applied.

we estimate a final sensitivity $\sigma_z^{\rm inc}$ to 1.5%, a 25% improvement over the Zh channel alone. This improvement refines many other derived quantities in the model-independent fit. We demonstrate the improvement for a few representative quantities in Table 6. We have performed a global 10-parameter model-independent fit following Ref. [48]. We compute sensitivities for the ILC alone and in combination with projected High Luminosity (HL)-LHC results. We take the optimistic projections for HL-LHC precision on cross sections from the CMS detector based on Ref. [59]. As discussed in detail in Ref. [48], twice the error of $\sigma_z^{\rm inc}$ propagates into the $\Gamma_{\rm tot}$ determination, and this error dominates for stages beyond the 250 GeV phase of the ILC. Our study at the ILC 250+500+1000 stage relatively improves the total width precision by 16%, Higgs to ZZ coupling by 25%, Higgs to WW coupling by 16%, and Higgs to $b\bar{b}$ coupling by 8%. For other couplings with less precision the $\sigma_z^{\rm inc}$ is not the largest source of uncertainty and less improvement is expected.

2.2.2 Operator analysis

New physics beyond the Standard Model (BSM) could give rise to modifications of the Higgs couplings. The proper framework to describe such possibilities in a model-independent

Relative error %	ILC 250+500		ILC 250+500+1000	
$\delta\sigma_{Zh}$	6.0%		2.5%	
Improvement		With HL-LHC		With HL-LHC
Γ	4.8 $\rightarrow$ 4.7	4.8 $\rightarrow$ 4.6	4.5 $\rightarrow$ 3.7	4.5 $\rightarrow$ 3.7
g_Z	0.99 $\rightarrow$ 0.94	0.99 $\rightarrow$ 0.94	0.98 $\rightarrow$ 0.75	0.98 $\rightarrow$ 0.75
g_W	1.1 $\rightarrow$ 1.1	1.1 $\rightarrow$ 1.1	1.1 $\rightarrow$ 0.89	1.1 $\rightarrow$ 0.88
g_b	1.5 $\rightarrow$ 1.5	1.5 $\rightarrow$ 1.5	1.3 $\rightarrow$ 1.2	1.3 $\rightarrow$ 1.1

Table 6: The improvement on selected coupling precisions by incorporating our ZZ fusion analysis from a typical 10-parameter model-independent fit. We show both the ILC exclusive results and ILC combined with the optimistic CMS HL-LHC input [59]. For details of fitting scheme and combination scheme, see Ref. [48]. The results for ILC 250/500/1000 (GeV) assume 250/500/1000 fb^{-1} integrated luminosities.

manner is the effective field theory approach. With respect to the SM gauge symmetry, such effects are expressed by dimension-six Higgs operators after integrating out heavy particles or loop functions [61, 62, 63, 64].[1] The operators modifying Higgs to ZZ couplings are naturally of particular interest in our case. This is partly because it will be one of the most precisely determined quantities through a recoil-mass measurement and partly because it is one of the key couplings that could help reveal the underlying dynamics of electroweak symmetry breaking. Certain operators may have different momentum dependence and thus measurements of differential cross sections may be more sensitive to the new effects.[2] The ILC is expected to have several operational stages with different center-of-mass energies, and the high-precision measurement achievable from ZZ fusion will contribute to our knowledge of these different operators.[3]

To demonstrate this important feature, we consider the following two representative

[1]For recent reviews of these operators, see e.g., Refs. [65, 66, 67, 163]. Many of these operators not only contribute to Higgs physics, but also modify electroweak precision tests simultaneously [69, 70, 71, 72].

[2]For discussions of the effects on Higgs decays due to these operators, see Ref. [73].

[3]Assuming existence of a single operator at a time, limits can be derived, see, e.g., [74].

operators

$$\mathcal{O}_H = \partial^\mu(\phi^\dagger\phi)\partial_\mu(\phi^\dagger\phi), \qquad \mathcal{O}_{HB} = g' D^\mu\phi^\dagger D^\nu\phi B_{\mu\nu}, \tag{2.8}$$

with

$$\mathcal{L}^{dim-6} \supset \frac{c_H}{2\Lambda^2}\mathcal{O}_H + \frac{c_{HB}}{\Lambda^2}\mathcal{O}_{HB}, \tag{2.9}$$

where ϕ is the SM SU(2)$_L$ doublet and Λ is the new physics scale. The coefficients c_H and c_{HB} are generically of order unity. Following the convention for comparison with existing studies [64, 67, 69, 70, 71, 72], we adopt the scaled coefficients $\bar{c}_H = \frac{v^2}{\Lambda^2}c_H$ and $\bar{c}_{HB} = \frac{m_W^2}{\Lambda^2}c_{HB}$. This translates to generic values of $\bar{c}_H \approx 0.06$ and $\bar{c}_{HB} \approx 0.006$ for $\Lambda = 1$ TeV.

The operator $\mathcal{O}_H$ modifies the Higgs-ZZ coupling in a momentum-independent way at lowest order. This operator renormalizes the Higgs kinetic term and thus modifies the Higgs coupling to any particles universally [75, 76]. Equivalently, one may think of rescaling the standard model coupling constant. In contrast, the operator $\mathcal{O}_{HB}$ generates a momentum-dependent Higgs-ZZ coupling. This leads to a larger variation of the production rate versus c.m. energy for the Zh process than the ZZ fusion because of the energy difference in the intermediate Z bosons. Consequently, the corresponding deviations of the cross sections are approximately

$$\begin{aligned}
\text{ILC 250 GeV}: \quad & \tfrac{\Delta\sigma}{\sigma}(Zh) && \approx -\bar{c}_H - 4.5\,\bar{c}_{HB}, \\
\text{ILC 500 GeV}: \quad & \tfrac{\Delta\sigma}{\sigma}(Zh) && \approx -\bar{c}_H - 25\,\bar{c}_{HB}, \\
& \tfrac{\Delta\sigma}{\sigma}(e^-e^+h) && \approx -\bar{c}_H + 1.1\,\bar{c}_{HB}, \\
\text{ILC 1 TeV}: \quad & \tfrac{\Delta\sigma}{\sigma}(e^-e^+h) && \approx -\bar{c}_H + 2.4\,\bar{c}_{HB}.
\end{aligned} \tag{2.10}$$

Such operators receive direct constraints from the LHC from similar production processes [69, 70], off-shell Higgs-to-ZZ measurement [77], etc., all of which lack desirable sensitivities due to the challenging hadron collider environment. Based on an analysis of current data the coefficient $\bar{c}_{HB}$ is excluded for values outside the window $(-0.045, 0.075)$[4] and $\bar{c}_H$ is far less constrained [69, 70].

[4]The window is $(-0.053, 0.044)$ for single-operator analysis. This smallness of the difference between the marginalized analysis and single-operator analysis illustrates that this operator mainly affects Higgs physics and thus other electroweak precision observables do not provide much information.

We only list above the cross sections which can be precisely measured at different ILC stages, with corresponding polarizations taken into account. The distinction between ZZ fusion(e^-e^+h) and Zh-associated production with Z decaying to electron-positron pairs is easily made by applying a minimal m_{ee} cut above m_Z.

In Fig. 10 we plot the expected constraints on the constants $\bar{c}_H$ and $\bar{c}_{HB}$ from the Zh and ZZ processes measured at the ILC, assuming only these two constants among the six-dimensional terms are nonzero. We show the 95% C.L. contours for different measurements. The dashed(dot-dashed) blue line represents the contour from Zh-associated measurement at ILC 250 GeV(500 GeV). The red line represents the contour from combined ZZ fusion measurements at ILC 500 GeV and 1 TeV. One can see that at a given energy for a simple production mode only a linear combination of the two operators is constrained, resulting in a flat direction in the contours. However, measurements of Zh at two different energies would allow us to measure both simultaneously, as shown in the gray contour. Moreover, the addition of the ZZ information at 1 TeV would offer *significant* improvements as shown in the yellow contour. This allows us to measure $\bar{c}_H$ and $\bar{c}_{HB}$ at the level of 0.04 and 0.004 respectively. Much of the improvement comes from the fact that in ZZ fusion, in contrast to Zh-associate production, the $\mathcal{O}_{HB}$ operator contributes with the opposite sign of the $\mathcal{O}_H$ operator. We note here such indirect measurements would strongly constrain BSM physics which are otherwise difficult to test, such as singlet-Higgs assisted baryogenesis [78], "neutral naturalness" [79, 80, 76], etc.

2.3 CONCLUSIONS

To summarize, the ZZ fusion channel for Higgs measurement could provide valuable information for precision studies of the Higgs width and couplings because of the logarithmic increase of the total cross section versus the center-of-mass energy as seen in Fig. 5. Although the signal suffers from large radiation-induced smearing at high energies it can be observed with good precision at a 1 TeV run and benefits from a multivariate analysis. We have also demonstrated the sensitivity to probe higher-dimensional operators at the ILC, which are

usually not covered by conventional global fits. We find:

(i) The inclusive cross section of the ZZ fusion channel can be measured to 2.5% at 1 TeV. This is competitive with the best estimate of Higgsstrahlung measurement at 250 GeV, as shown in Secs. 2.1.3 and 4.2.4.

(ii) Combing the ZZ fusion and Higgsstrahlung channels, the model-independent measurement of the inclusive cross section can be improved to 1.5% with a commensurate improvement of the Higgs width determination, as shown in Sec. 2.2.1.

(iii) Sensitivities on the inclusive cross section $\sigma_Z^{\rm inc}$ at multiple energies also offer the possibility to distinguish contributions from different higher-dimensional operators induced by BSM physics. We demonstrate the ability to simultaneously constrain two operators whose effects are difficult to observe at the LHC, as shown in Sec. 2.2.2. Including the ZZ fusion channel provides as large as 50% relative improvement for the constraint on the chosen operators compared to the Zh-associated production channel alone.

In the preceding analysis and discussion, we have shown the appreciable impact of including the ZZ fusion channel at the ILC for Higgs physics. Full detector simulations may be desirable to further the study of this signal mode.

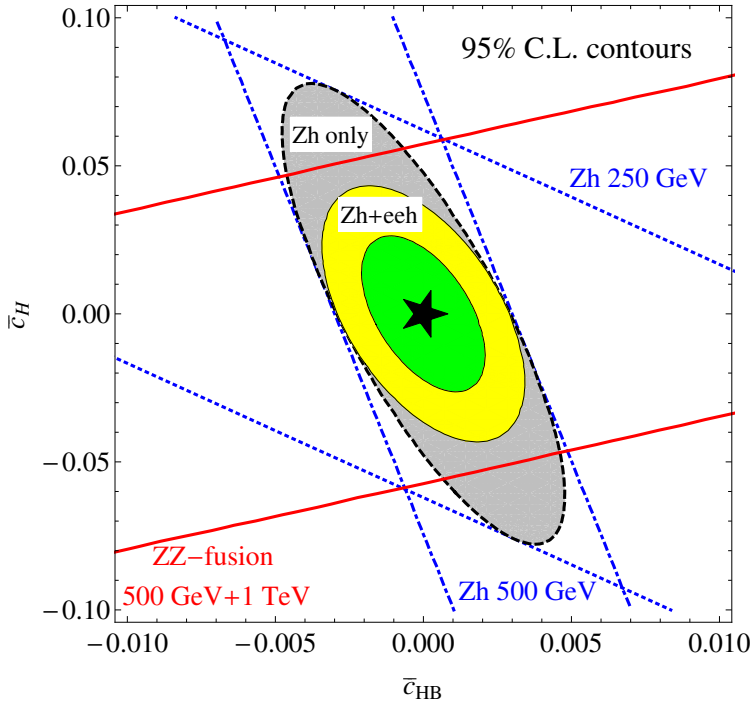

Figure 10: Constraints on coefficients of dimension-six operators $\bar{c}_H$ and $\bar{c}_{HB}$ with and without the inclusion of the ZZ fusion channel. The dashed and dot-dashed lines represent 2σ deviations from zero in the Zh channel at 250 and 500 GeV (blue lines), respectively. The solid (red) lines indicates the constraint from ZZ fusion for 500 GeV plus 1 TeV. The outer (black-dashed) contour shows the constraint from combined Zh measurements and the middle (yellow) and inner (green) contours show the combined 2σ and 1σ results with ZZ fusion included.

3.0 HIGGS DECAY TO LIGHT JETS AT THE LHC

In this chapter we describe with some detail our study of Higgs decay to a pair of light un-tagged jets $h \to jj$, in the associated production channel as in Eq. (1.18). We will exploit the leptonic final state decays of the electroweak gauge bosons, and employ a hadronic tag for the Higgs boson while optimizing the mass reconstruction. We argue that a 1σ sensitivity of 1 (or 4) times the SM value with statistic (or systematic) uncertainties can be achieved for the case where the Higgs decays to un-tagged jets. This is achieved with a judicious choice of kinematic discriminants and a combination of the final state channels. Together with $h \to b\bar{b}$ and $h \to c\bar{c}$ studies, the un-tagged channel puts an independent dimension of bound in the space of branching ratios of Higgs decays to quarks and gluons. Assuming a well measured ggh coupling at the end of HL-LHC [125], the result further puts comparable but independent constraints on the light-quark Yukawa couplings. We also estimate that this channel may offer a better probe to the strange-quark Yukawa coupling.

The remains of the chapter proceed as follows, Section 3.1 specifies the signal and dominant background processes. Section 3.2 describes and presents the detailed analyses and gives the main results in terms of the cut-efficiency tables and figures. In the same section, we also study how to control the systematic errors for the large backgrounds. Section 3.3 describes an alternate search strategy based on momentum balance discriminants. Section 3.4 calculates the signal sensitivity and presents obtained constraints on Higgs couplings to quarks and gluons in a correlated manner, while Section 3.5 summarizes and concludes.

3.1 SIGNAL AND BACKGROUND PROCESSES

As discussed above, the promising channel in which to study the Higgs decay to light jets is the associated production with an electroweak gauge boson W or Z, which subsequently decays to leptons. Depending on the production mechanisms and the final states, we consider the following subprocesses

$$q\bar{q} \to W^{\pm}h \to \ell^{\pm}\nu + jj, \tag{3.1}$$

$$q\bar{q},\ gg \to Zh \to \begin{cases} \ell^{+}\ell^{-} + jj, \\ \nu\bar{\nu} + jj, \end{cases} \tag{3.2}$$

where $\ell = e, \mu$ and $j = g$ or u, d, s. Practically, j is a gluon as expected in the SM. We thus generically denote the SM signal by $Vh(gg)$, whenever convenient. In our calculations, events are generated with MadGraph at the leading order, with "NNPDF23_nlo_as_0119_qed" as the PDF set [138]. For the $gg \to Zh$ process via the quark loops, we use Madgraph_NLO [139] and Madspin [140]. This channel contributes about $10\% - 20\%$ to the total Zh production rate. We apply an overall rescaling of QCD K-factors to the signal processes, to match the total NNLO QCD and NLO EW cross section results taken from summary of Higgs cross section working group [137]. The K-factors are about 2 and 1.2 for the gg and $q\bar{q}$, respectively. We include the finite masses for the fermions running in the loop in the gg initiated process. Some care is needed regarding the gg process because of its different transverse momentum (p_T) dependence and sensitivity to new physics contribution in the loop as discussed in Ref. [141]. In Fig. 11, we compare the Higgs boson transverse momentum distributions for the signal processes $q\bar{q} \to Zh$ and $gg \to Zh$. The $q\bar{q}$-initiated channel peaks at $p_{T(h)} \approx 50$ GeV, a typical mass scale associated with the final state particles of Zh. The gg-initiated channel peaks at around $p_{T(h)} \approx 150$ GeV, due to the top mass threshold enhancement. The differential cross section of gg drops faster than $q\bar{q}$ with increasing $p_{T(h)}$, due to the destructive interference between the triangle and box diagrams.

The Higgs is further decayed according to the branching ratios listed in Ref. [137]. Events are then showered and hadronized using PYTHIA6 [142], and run through DELPHES [143]

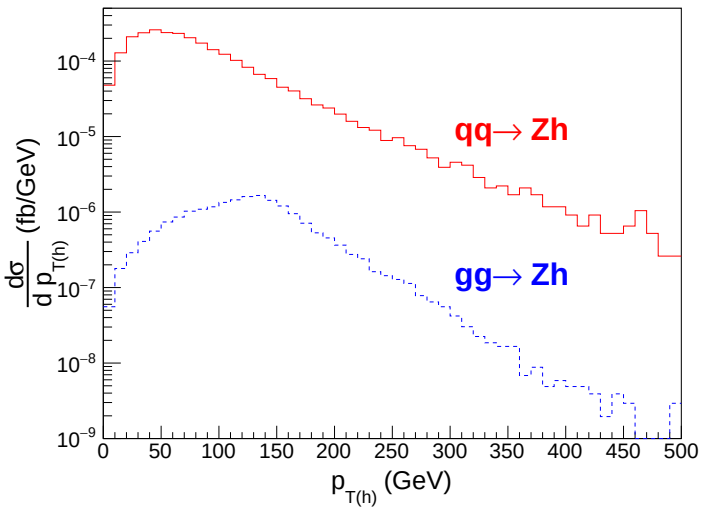

Figure 11: Higgs boson transverse momentum distribution for the signal processes $qq \to Zh$ (upper solid curve) and $gg \to Zh$ (lower dashed curve) at the 14 TeV LHC.

for detector simulation and jet reconstruction. For the SM backgrounds, we mainly consider the dominant irreducible background process $V + jj$ at LO, where the V decays and contributes accordingly to the three signal channels. At the generator level, we apply some basic cuts on the jets to remove infrared and collinear divergences for the QCD background processes

$$p_{T(j)} > 20 \text{ GeV}, \quad |\eta_j| < 3, \quad R_{jj} > 0.4. \tag{3.3}$$

The hadronic jets are reconstructed with anti-kt jet algorithm with a cone size $R = 0.4$. In our future analyses, we will be considering a relatively boosted Higgs recoiling off of the vector boson. Therefore, to improve the simulation statistics, we also add a generator-level cut on the vector boson

$$p_{T(V)} > 150 \text{ GeV}. \tag{3.4}$$

In Table 7 we give the cross sections used for our signal and background processes including the basic cuts in Eq. (3.3) and with various p_T thresholds for the vector boson. The first is the total cross section with no $p_{T(V)}$ cut, the second and third demand $p_{T(V)}$ cuts

σ (fb)	cuts Eq. (3.3)	+ Eq. (3.4)	+ $p_{T(V)} > 200$ GeV
$q\bar{q} \to Zh \to \ell^+\ell^- \, gg$	3.5	0.39	0.17
$gg \to Zh \to \ell^+\ell^- \, gg$	0.71	0.20	6.2×10^{-2}
$q\bar{q} \to Zjj \to \ell^+\ell^- \, jj$	2.5×10^5	1.2×10^4	4.8×10^3
$q\bar{q} \to Wh \to \ell\nu \, gg$	20	2.3	0.99
$q\bar{q} \to Wjj \to \ell\nu \, jj$	2.5×10^6	1.0×10^5	3.9×10^4
$pp \to t\bar{t} \to \ell\nu jj b\bar{b}$	1.1×10^5	1.5×10^4	5.7×10^3
$q\bar{q} \to Zh \to \nu\nu \, gg$	11	1.2	0.50
$gg \to Zh \to \nu\nu \, gg$	2.1	0.60	0.18
$q\bar{q} \to Zjj \to \nu\nu \, jj$	7.4×10^5	3.6×10^4	1.4×10^4

Table 7: Cross sections in units of fb for signal and dominant background processes, with the parton-level cuts of Eq. (3.3), and boosted regions $p_{T(V)} > 150,\ 200$ GeV.

of 150 and 200 GeV respectively. No cuts on the final state leptons are applied for the table.

A few remarks are in order. Although we have re-weighted our events by the K-factors to account for the NNLO QCD/NLO EW corrections for the signal rate, we could not claim the theoretical accuracy to this level, in particular in the extreme kinematic region as in Eq. (3.4). Indeed, perturbative calculations tend to lead to harder p_T spectrum than our approximation via the final state radiation (FSR) or the initial state radiation (ISR) as in PYTHIA. On the other hand, the extended $p_{T(V)}$ spectrum is rather smooth and the good experimental measurement with the large data sample would make the imprecise knowledge from theory less crucial. As for the higher order corrections to the hadronic Higgs decay, we believe that the effects are not significant given the color-singlet nature of the Higgs boson and our rather inclusive treatment of the final-state jets, as discussed in detail in later sections.

3.2 SIGNAL SELECTION

In further studying the signal characteristics in Eqs. (3.1) and (3.2), we categorize the channels according to the zero, one, or two charged leptons from the vector boson decays. In addition, the signal has two leading jets from the Higgs decay, with invariant mass of the Higgs boson. At high $p_{T(h)}$, the distance between the two hadronic jets can be estimated as

$$R_{jj} \approx \frac{1}{\sqrt{z(1-z)}} \frac{m_h}{p_{T(h)}}, \tag{3.5}$$

where $z,\ 1-z$ are the momentum fraction of the two jets. The LO parton-level distributions of three kinematic discriminants for the Zh channel, the transverse momentum $p_{T(Z)}$, the jet separation R_{jj}, and the di-jet invariant mass m_{jj}, are shown in Fig. 12, comparing the signal (solid) and dominant background (dashed), after the generator-level cuts as in Eqs. (3.3) and (3.4). Obviously, $p_{T(Z)}$ is singular for the QCD background as seen in Fig. 12(a). The two jet separation R_{jj} in Fig. 12(b) shows the either collinear feature from the parton splitting in the final state radiation (FSR) or back-to-back near π due to the initial state radiation (ISR) for the background process, and is narrowly populated near $2m_h/p_{T(h)}$ for the signal. The resonance bump near m_h is evident as in Fig. 12(c). Because of the small rate, the signal curves have been scaled up by a factor of 5000. We also show an event scatter plot in Fig. 12(d), where the (red) dense band with crosses presents the signal events and the (blue) dots show the background events. We see the strong correlation between the boosted $p_{T(Z)}$ and collimated jets with smaller R_{jj}.

To suppress the huge QCD di-jet backgrounds, we must optimize the reconstruction of the Higgs mass. There are two common methods to reconstruct hadronic decays of Higgs boson depending on the kinematical configurations. One is the sub-structure (fat-jet) approach: an early example for Higgs search in $b\bar{b}$ channel was introduced in Ref. [130]. Because of the highly boosted nature of the Higgs boson, a fat-jet identified as the hadronic decay products of the Higgs boson is first selected. Various jet substructure observables and techniques such as mass-drop and filtering [130], pruning [144], trimming [145], N-subjettiness [146] etc. can be applied on the fat-jet to further improve the reconstruction of the invariant mass. For a recent review, see Ref. [147]. The other approach is to simply resolve the leading jets.

This is the common practice when the Higgs is produced not far from the threshold, and the Higgs is identified as the sum of the two leading jets. Experimentally, the anti-kt jet algorithm, given its regular jet shape, gives good reconstruction of hadronic jets, and is the default hadronic jet reconstruction algorithm used at ATLAS/CMS. The $Vh(b\bar{b})$ search at LHC is currently carried with the two resolved jet with anti-kt $R = 0.4$ method. In a recent analysis [148] the two methods are compared for the $Wh, h \to bb$ process for LHC14 in the kinematic region 200 GeV $< p_{T(h)} <$ 600 GeV. The resolved approach is better in the 200 GeV $< p_T <$ 300 GeV range. The jet-substructure approach is significantly better in the $p_T >$ 600 GeV. The results are qualitatively expected, since the high p_T corresponds to a smaller cone-size of the fat-jet as argued in Eq. (3.5).

Since the signal events tend to populate near the kinematic threshold, we will exploit the resolved method with two hard jets. However, additional QCD radiations from the highly energetic jets are not negligible. Kinematically, it gives a reconstructed di-jet mass peak smeared towards lower value. Some related effects including the NLO correction is studied in Ref. [149]. We thus propose a modification of the two-jet-resolved method by including possible additional jets in the decay neighborhood – a "resolved Higgs-vicinity" method. After clustering the jets with anti-kt $\Delta R = 0.4$, two leading p_T jets are clustered as the "Higgs-candidate". Then additional jets j' are also clustered to the "Higgs candidate" in sequence of angular vicinity, whenever $R_{Hj'} \leq R_{\rm max}$. For the rest of the analyses, we choose

$$R_{\rm max} = 1.4. \tag{3.6}$$

The optimal method is to select events with two leading p_T jets that satisfy $R_{jj} \leq R_{\rm max}$, and add to the di-jet system any sub-leading jets within the distance $R_{\rm max}$. In practice, we find that including one additional hard radiation in the decay is sufficient. In Fig. 13 we compare several resolved-jet methods in their reconstruction of the Higgs mass, against the Vjj background. The central and hard jet requirements are $p_{T(j)} > 30$ GeV and $|\eta_j| < 2.5$. In Fig. 13(a), we reconstruct the Higgs with the two leading p_T jets and veto events with more than two central hard jets. As shown in the plot, the veto method removes the background most efficiently, the cut also reduces the signal significantly. Fig. 13(b) shows the 2jet-inclusive case, which is the same as (a) but does not veto additional jets. It improves the

signal rate, but the signal mass peak is still smeared to the lower value. Fig. 13(c) is the "resolved Higgs-vicinity" method, which adds the additional hard jet, and sharpens the mass peak to help increase the overall $S/\sqrt{B}$ sensitivity.

We study the sensitivity to pile-up contamination of this reconstruction method. In Fig. 14, we compare it with the two jet resolved method adding pile-up samples in DELPHES. As expected, the additional-jet method is more sensitive to the pile-up jets, yet still retains a slight advantage even under pile-up value $\langle\mu\rangle = 140$ [150].

In the following, we describe the searches with the detailed signal and background analyses, for the channels with two, one and zero charged leptons, respectively. For simplicity, we use 2 jets reconstruction of the mass peak from now on.

3.2.1 $\ell^+\ell^- + jj$ channel

For the two-lepton channel, we simulate the signal processes as in Eq. (3.2) with $Z \to \ell^+\ell^-$, $h \to gg$. We require exactly one pair of charged leptons $\ell^\pm = e^\pm$ or $\mu^\pm$, same flavor, opposite charge, along with at least two energetic jets. The dominant background is by far from $Z + jj$. The two leading p_T jets are required to be close by having a separation less than $R_{\rm max} = 1.4$, and an invariant mass between 95 and 150 GeV. They satisfy the following acceptance cuts

- 2 leptons with $p_{T(l)} > 30$ GeV and $|\eta_l| < 2.5$
- $p_{T(\ell\ell)} > 200$ GeV
- at least 2 jets with $p_{T(j)} > 30$ GeV and $|\eta_j| < 2.5$
- $R_{j_1 j_2} < 1.4$
- 95 GeV$< m_h <$ 150 GeV

The di-jet mass window around m_h is chosen to optimize the $S/\sqrt{B}$ at HL-LHC. Table 8 shows the efficiency of applying the sequence of cuts. The overall efficiencies are about 14%, 7.6%, for the $q\bar{q}$, gg initiated signal processes, respectively, and about 1.9% for the background process. We would like to point out that from only the statistical sense, the signal sensitivity $S/\sqrt{B}$ would not be notably increased from the generator level results to

that with final cuts. However, the fact that the background is reduced by around two orders of magnitude helps to control the systematic uncertainties, as we will discuss later.

3.2.2 $\ell^{\pm} + \not{E}_T + jj$ channel

For the one-lepton channel, we look at signal process in Eq. (3.1) with $W \to \nu\ell,\ h \to gg$. The dominant backgrounds are $W + jj$ and $t\bar{t}$. Similar to the last section, the acceptance cuts are

- one lepton $p_{T(\ell)} > 30$ GeV and $|\eta_\ell| < 2.5$
- $p_{T(\nu\ell)} > 200$ GeV, $\not{E}_T > 30$ GeV
- at least 2 jets with $p_{T(j)} > 30$ GeV and $|\eta_j| < 2.5$
- $R_{j_1 j_2} < 1.4$
- 95 GeV $< m_h <$ 150 GeV.

The W transverse momentum $p_{T(\nu\ell)}$ can be reconstructed from the charged lepton plus the missing transverse momentum $\not{E}_T$. Table 9 shows the cut-flow at various stages of the cuts applied. The overall efficiencies are about 18% for the $q\bar{q}$ initiated signal process, and about 2.5%, 2.5% for the $Wjj,\ t\bar{t}$ background processes, respectively.

3.2.3 $\not{E}_T + jj$ channel

The zero-lepton channel is studied with signal processes as in Eq. (3.2) with $Z \to \nu\nu,\ h \to gg$. The dominant background again mainly is $Z + jj$. Similar to the above, the cuts acceptance are

- lepton veto with $p_{T(\ell)} > 30$ GeV $|\eta_\ell| < 2.5$
- $\not{E}_T > 200$ GeV
- at least 2 jets with $p_{T(j)} > 30$ GeV $|\eta_j| < 2.5$
- $R_{j_1 j_2} < 1.4$
- 95 GeV $< m_h <$ 150 GeV.

The $\not{E}_T$ is essentially from $p_{T(Z)}$. Table 10 shows the cut-flow at various stages of the cuts applied. The overall efficiencies are about 23%, 15%, for the $q\bar{q}$, gg initiated signal processes, respectively, and about 4.5% for the background process.

Results presented in the above three sections have been double checked by other approaches.

3.2.4 Background control

As calculated earlier and presented in the previous tables, the signals for $h \to gg$ in the SM associated with W/Z to leptons at the 3000 fb^{-1} HL-LHC may lead to sizable event rates, with about 200 events for the $\ell^+\ell^-$ channel, 1300 events for the $\ell^\pm\nu$ channel, and 1200 events for the $\nu\nu$ channel, respectively. However, the difficulty is the overwhelmingly large SM background, with a signal-to-background ratio at the order of 10^{-4}. As such, one must be able to control the systematic errors to sub-percent in order to reach statistically meaningful result. This is an extremely challenging job, and one would not be able conclude without real data to show the detector performances. On the other hand, there are ideas to shoot at the goal. Here we adopt one of the commonly considered methods and demonstrate our expectations.

For the two lepton and $\not{E}_T$ channel, the dominant background is the SM $Z + jj$ production. With current selection, the two jet invariant mass spectrum is smoothly decreasing within a range of $[60, 300]$ GeV and our signal region lies between 95 GeV and 150 GeV. Making use of the well-measured side-bands, the estimation of background contribution in the signal region could be obtained directly from a fit to the m_{jj} distribution. We generated Z+jets samples with MadGraph generator corresponding to 10 fb^{-1} and passed the events through PYTHIA and DELPHES to simulate the parton shower and ATLAS detector effect. We adopt a parameterization ansatz to fit the distribution in the m_{jj} range from 60 GeV to 300 GeV

$$f(z) = p_1(1-z)^{p_2} z^{p_3}, \tag{3.7}$$

where p_i are free parameters and $z = m_{jj}/\sqrt{s}$. This ansatz is found to provide a satisfactory fit to the generated Z+jets MC simulation at 14 TeV, as shown in Fig. 15.

In order to estimate the uncertainty of background determination for 3000 fb^{-1} integrated luminosity, we take this three-parameter function in Eq. (3.7) as the baseline to generate the data-like spectrum following Poisson fluctuation. Figure 16 shows the generated spectra for 300 fb^{-1} and 3000 fb^{-1}. We fit these spectra with three-parameter, four-parameter and five-parameter functions within the range of $[60, 300]$ GeV but excluding the signal region $[95, 150]$ GeV. The fitting results and uncertainties are summarized in Figure 17 and Table 11. Besides the three-parameter function, four-parameter and five-parameter functions are tested as below

$$f(z) = p_1(1-z)^{p_2} z^{p_3+p_4\log(z)}, \quad f(z) = p_1(1-z)^{p_2} z^{p_3+p_4\log(z)+p_5\log^2(z)}. \tag{3.8}$$

We also vary the fitting range from $[60, 300]$ GeV to $[70, 250]$ GeV and $[80, 200]$ GeV to test the stability, which are summarized in Table 12. If we consider the variation due to this fitting range as another source of systematics, the uncertainty of background estimation of $Z(\ell\ell)$+jets for 3000 fb^{-1} is 0.33%. The uncertainty considered here includes the fitting uncertainty, fitting function variation and fitting range variation, which is largely depending on the statistics of side-band region. The background uncertainty from fitting is dominated by the statistics of side-band regions, which is proportional to the background yield. It is reasonable to assume the jet mass spectrum to be independent of the leptonic decay details of the vector bosons. To the first-order estimation, the uncertainties of $Z(\nu\nu)$+jets and $W(\nu\ell)$+jets are comparable at the order of 0.1%. We thus summarize the systematic percentage uncertainties for the three leptonic channels as

$$Z(\ell^+\ell^-)+jj:\ 0.33\%; \quad W(\ell^\pm\nu)+jj:\ 0.10\%; \quad Z(\nu\nu)+jj:\ 0.13\%. \tag{3.9}$$

As seen for example in Table 9 for the one-lepton channel, the $t\bar{t}$ background is sub-dominant yet not negligible. There are other smaller and non-negligible processes such as semi-leptonic decays of di-boson, which are not included in our current studies since they would not change our conclusions. Full simulation and control shall be required on all the relevant processes once the data is available. Similar to the comment at the end of Sec. 3.1, we could only claim the theoretical accuracy at the LO for the background processes, given

the complicated kinematical acceptance. However, we argue that for our purpose of estimating the signal sensitivity, it suffices to say that the di-jet invariant mass distribution for backgrounds is smooth in the signal region, fitted with simple functions as done above.

3.3 ALTERNATIVE DISCRIMINANTS WITH MISSING ENERGIES

We note that a momentum balance discriminant has been proposed in Ref. [151] as a useful kinematic variable in processes where a new resonant particle is produced in association with a SM vector boson radiated in an initial state, $pp \to R + V$. The transverse momenta of these states should balance

$$p_T^R - p_T^V = 0. \tag{3.10}$$

Due to detector effects and radiation, the measured momentum balance is not perfect and it is particularly more severe for the background since the QCD processes tend to have larger radiation. This is a useful kinematic discriminant between the signal and background [151]. However it is not applicable whenever there is missing energy in the event. In fact, the definition of the missing transverse energy in an event is the negative of the vector sum of the visible p_T. In the above example it offers only a tautology for the momentum balance discriminant. We offer, in the case of events with significant missing energy, a new discriminant to capture the kinematic features of the event. We define this discriminant by calculating the scalar sum of the transverse momenta of the visible particles in the event, and then subtracting the missing transverse energy

$$TvQ \equiv \Sigma_i |p_{Ti}| - |\not{E}_T|. \tag{3.11}$$

This is a version of a momentum balance discriminant, referred as TvQ (Transverse event Quality). Since the missing momentum in an event is defined by the negative of the vector sum $|\Sigma_i \vec{p}_{Ti}|$, the quantity TvQ is the difference between the scalar and vector sums of the visible p_T in the event. TvQ tends to be small when the observable particles are a highly collimated collinear bunch, while it takes a large value when the observable particles spread out and when $R + V$ production is near the kinematical threshold.

It would be more intuitive to look at the signal and background in a two dimensional space of discriminants. Consider the $\not{E}_T$ signal from $pp \to Zh \to \nu\nu\ gg$. We plot the event population in the $p_{T(jj)} - TvQ$ plane as shown in Fig. 18. We see that in the signal sample (blue crosses), regions of large visible p_T correlate with the zero value of TvQ. Events with high boost, and therefore columnated Higgs decay products, correlate with lower values of TvQ as predicted. The QCD background sample Z+jets (red dots), on the other hand, tends to further spread out.

Another simple discriminant, somewhat correlated with TvQ for the Zh final state is a transverse angular variable, ϕ_{Zh} defined as the angle between the missing transverse energy vector and the vector sum of the visible p_T. This is clearly motivated since we expect the Z and h states to be nearly back to back in the event, in contrast to the QCD multiple jet events. We examined the selective cuts (-30 GeV $< TvQ <$ 10 GeV) or ($\pi - 0.5 < \phi_{Zh} < \pi + 0.5$) and found them effective in separating the signal from the backgrounds. In exploiting more kinematical variables in some treatment like Boosted-decision-Tree technique (BDT) or Neural Networks (NN), those discriminative variables may be taken into consideration.

3.4 RESULTS AND DISCUSSION

3.4.1 Signal significance

As we see from the cut-flow tables 8-10, the Vjj backgrounds are dominant. We calculate the signal statistical significance as

$$\mathcal{S} = \frac{N_{\rm sig}}{\sqrt{N_{\rm bkg}}}, \tag{3.12}$$

with the statistical uncertainty of the dominant background as the only uncertainty. The combined significance of the $Vh(gg)$ signal is shown in Table 13. The three leptonic channels from the V decays give comparable contributions. The two-charged-lepton channel has the smallest signal strength, but cleaner in signal identification. The one and zero-charged-lepton channels show good reconstruction and contribute better sensitivities. Adding the

$0, 1, 2$ charged-lepton channels, the pure statistical estimation gives a 0.82σ significance, which indicates how challenging an observation of the SM $Vh(gg)$ signal could be.

When the signal rate and S/B is small, one must worry about the systematic uncertainties for the measurements. As discussed in length in Sec. 3.2.4, we rely on the precision sideband fit to control the systematics in the signal region near $m_{jj} \sim m_h$. If ϵ_B is the fitted background percentage uncertainty, we then assume the systematic error to be $\epsilon_B \times N_{\rm bkg}$. We thus present a different significance dominated by the systematics, defined as

$$\mathcal{S}_{\rm sys} = \frac{N_{\rm sig}}{\epsilon_B \times N_{\rm bkg}}, \tag{3.13}$$

As shown in Sec. 3.2.4, with 3000 fb^{-1} of data and m_{jj} signal mass window taken as $95 - 150$ GeV, we have $\epsilon_B = 0.33\%,\ 0.10\%,\ 0.13\%$ for the two, one and zero lepton channels, respectively. The results with this significance estimation are also shown in Table 13. The outcome is worse than the statistical-error-only treatment. We would also hope the further reduction of non-statistic uncertainties with more dedicated background fitting schemes, once real data is available from experiments.

3.4.2 Bounds on the branching fractions and correlations with $h \to b\bar{b},\ c\bar{c}$

The interpretation of these results to bound on individual Higgs decay channels needs further discussion. Thus far, we have only simulated $h \to gg$ as the Higgs decay channel, since it dominates the SM branching fraction of the Higgs decay to light jets. Practically, however, contributions from mis-tagged $h \to b\bar{b}$, $h \to c\bar{c}$, and possible light-quark pairs are all accumulated in the events and should be taken into account correlatively. Thus, the signal we have been searching for in this study really is $h \to j'j'$ where j' is an "un-tagged jet" including possible b, c and j (g, u, d, s) contributions.

Listed in Table 14 are the working points for the tagging/mis-tagging efficiencies assuming that different observable event categories listed as different rows are un-correlated. For instance, a b quark will be tagged as a b with a probability of $\epsilon_{bb} = 70\%$, and mis-tagged as a c and an un-tagged j' with $\epsilon_{cb} = 13\%$ and $\epsilon_{j'b} = 17\%$, and so on. Here the subscript a denotes the jet-tagged flavor category, and i denotes the parton as the source channel. The

numbers are the same as in Category "c-tagging I" of Table 1 in Ref. [131], as reasonable estimates for the experimental performance at the 14 TeV LHC, and for consistency of later comparison. We extend to the double-tagged event categories with corresponding Higgs branching fraction channels as,

$$e_{ai} = \frac{\epsilon_{ai}^2 \times (\mathrm{BR})_i}{\sum_j \epsilon_{aj}^2 \times (\mathrm{BR})_j}. \tag{3.14}$$

We show in Table 15 the percentage contributions of these decay channels $h \to ii$ in each experimentally tagged category a. For instance, a pair of un-tagged jets in category $j'j'$ will have a probability of 74% from the SM Higgs decay to a pair of gluons, and 16% or 10% from $b\bar{b}$ or $c\bar{c}$, respectively. With the current tagging efficiency, we translate the significance 0.82σ on $\mathrm{BR}(h \to jj)$ to the un-tagged signal category $\mathrm{BR}(h \to j'j')$ by rescaling as

$$\mathcal{S}_{j'} = \frac{\mathcal{S}_j}{e_{j'j}} = \frac{0.82\sigma}{74\%} = 1.1\sigma, \tag{3.15}$$

that accounts for mis-tagged $b\bar{b}$, $c\bar{c}$ contributions as well. In other words, if an observation of $h \to j'j'$ were made in the future LHC run, the interpretation for individual channels would be based on Table 15, with updated tagging efficiencies.

As is customary, we define the signal strength for a decay channel $h \to ii$ as

$$\mu_i = \frac{\mathrm{BR}(h \to ii)}{\mathrm{BR}^{\mathrm{SM}}(h \to ii)}, \tag{3.16}$$

where we consider $ii = b\bar{b}$, $c\bar{c}$, and jj. Assuming each category is statistically independent and following Gaussian statistics. We combine the three categories to get the three dimensional contour constraint on $\{\mu_b, \mu_c, \mu_j\}$ correlatively based on the relation

$$\begin{aligned} \mathcal{S}^2 > \sum_a \chi_a^2 &= \sum \frac{(x_a - \overline{x}_a)^2}{\sigma_a^2} \\ &= \sum_a \frac{(\sum_i \epsilon_{ai}^2 \mathrm{BR}_i N_{\mathrm{sig}}^{prod} - \sum_i \epsilon_{ai}^2 \mathrm{BR}_i^{\mathrm{SM}} N_{\mathrm{sig}}^{prod})^2}{(\sqrt{N_{\mathrm{bkg}}})^2} \\ &= \sum_a \frac{(\sum_i e_{ai}\ \mu_i - 1)^2}{(1/\mathcal{S}_a)^2} \end{aligned} \tag{3.17}$$

where $\mathcal{S}_a$ is the significance from each category identified by experiments, and e_{ai} are the double efficiencies from each decay channel i in category a given in Table 15.[1] We take $\mathcal{S}_a = (11,\ 1.35,\ 1.1\ (0.35))$ for the three categories, assuming only statistical errors with 3000 fb^{-1} data. The first number is from Table 12 in the ATLAS MC study [124], making use of "One+Two-lepton" combined sensitivity. The second number comes from Fig. 2(a) of Ref. [131], the extrapolated study on the same MC dataset assuming the same tagging efficiency. Assuming most of the sensitivity on μ_c comes from the double c-tagged category, we likewise rescale the number with $e_{c'c}$ and a $\sqrt{2}$ since they consider 2×3000 fb^{-1} data from two experiments. The third number is from our current "Zero+One+Two-lepton" un-tagged jets study, with the number in parenthesis including the systematic error. The fully correlated signal strengths are plotted in Fig. 19, for (a) a 3-dimensional contour in (μ_b, μ_c, μ_j) at 1σ, (b) the projected contour on the $\mu_j - \mu_c$ plane with statistical error only, and (c) with systematical error dominance. The shadowed contour regions are the projection of the 3D contour (μ_b, μ_c, μ_j) onto the μ_c-μ_j plane at 1σ and 2σ, and the solid ovals are for a fixed value $\mu_b = 1$. Allowing μ_b to float, the contour regions are slightly larger than the ovals. We note that certain values of the parameter space plane are excluded when BR($h \to bb$) + BR($h \to cc$) + BR($h \to jj$) > 1 and where our SM production assumption breaks down. This is represented in the plots by the gray shaded region. The 95% Confidence Level (CL) global upper bounds (approximately 2σ) on the branching fractions with statistical errors (systematic errors) for 3000 fb^{-1} with respect to the SM predictions can be obtained as

$$\mathrm{BR}(h \to jj) \leq 4\ (9) \times \mathrm{BR}^{SM}(h \to gg), \tag{3.18}$$

$$\mathrm{BR}(h \to c\bar{c}) < 15 \times \mathrm{BR}^{SM}(h \to c\bar{c}), \tag{3.19}$$

Although this bound on the $h \to gg$ channel is not nearly as strong as that from the production fit $gg \to h$ assuming the SM value, our study and results lay out the attempt of the search for the direct decay of the Higgs boson to gluons and the light quarks. The result for $c\bar{c}$ is comparable with the best existing extrapolations [152, 131], although adding the un-tagged category slightly improve the constraints on the c-quark Yukawa coupling, as expected.

[1] Note the different efficiencies defined in Tables 14 and 15, with the normalizations $\sum_a \epsilon_{ai} = 1$ in categories, and $\sum_i e_{ai} = 1$ in channels.

Further improvements can be made by including the production of the vector boson fusion (VBF) [153] and $t\bar{t}h$ [154]. They are the sub-leading contributions to the $h \to jj$ study at Run I and become more important production channels at Run II [155]. Our study includes for simplicity only double-tagged categories, and single b or c tagged categories can be further included as done in the recast by Ref. [156]. Statistics can be further improved by analysis with likelihood fitting, BDT, etc. once data is available.

3.4.3 Bounds on light-quark Yukawa couplings

So far, possible contributions from light quarks (u, d, s) have been ignored in accordance with the SM expectation. The bound on $h \to jj$ in Eq. (3.18) can be translated into those for the light quark Yukawa couplings. Assuming the SM ggh coupling, and varying one light quark Yukawa y_q at a time, we translate our bound on μ_j to the Yukawa couplings for light quarks u, d, s by scaling the branching fraction with $\mu_q \propto y_q^2$. Our results of the bounds on the Yukawa couplings are shown in Table 16. There have been attempts to probe the light quark Yukawa couplings in the literature [157, 152, 158, 159, 160, 161]. Recent studies on the inclusive Higgs production and its spectra of $p_{T(h)}$ and y_h claim various improved constraints on the couplings [152, 158], compared to constraints from a global fit [162]. The upper bounds from our study of Higgs decay to light jets are comparable to those derived from the Higgs production kinematics, as also shown in Table 16, and thus provide complementary information to the existing approaches. The SM Yukawa coupling for the light quarks are taken to be proportional to their individual $\overline{\text{MS}}$ running masses, which we evolve with N^{4}LO QCD from the PDG definition at 2 GeV [163] to the Higgs mass at 125 GeV.[2]

[2] There is however a discrepancy of the values used for the light quark running mass in the literature [157, 160, 152]. For instance, using the input from PDG, we find the strange quark mass to be $\overline{m}_s(m_h) = 53$ MeV, whereas the other adopted values are 83 MeV at the scale m_h [160], $\overline{m}_s(m_h/2) \sim 48$ MeV [157], and $\overline{m}_s(m_h/2) \sim 57$ MeV [152].

3.5 SUMMARY AND CONCLUSIONS

We have carried out a detailed study of the Higgs boson decay to light un-tagged jets in the vector boson associated channel $pp \to Vh$, with $h \to gg$ and $V = W^{\pm}$, Z decaying to leptons at the 14 TeV HL-LHC with 3000 fb^{-1}. To differentiate the di-jet signal from the huge SM QCD backgrounds, we have maximized the signal sensitivity by combining searches in the 0, 1 and 2-leptonic decay channels of the vector bosons. We used MadGraph, PYTHIA, and DELPHES for the signal and background simulations. Our findings can be summarized as follows.

- In Sections 3.2.1-3.2.3, we optimized the kinematical cuts according to the individual signal channels to enhance the $S/\sqrt{B}$ as well as S/B. The boosted kinematics for the di-jet signal has the advantage to improve S/B, while to keep the $S/\sqrt{B}$ roughly the same. We proposed the "di-jet-vicinity" Higgs mass reconstruction method as seen in Fig. 13, and tested its effectiveness against the pile-up effects as in Fig. 14.
- In Sec. 3.2.4, we studied in great detail on how to control the systematic errors by making use of the side-bands with a few fitting functions. We found that with 3000 fb^{-1}, it is conceivable to achieve the sub-percent level systematic uncertainties, as given in Eq. (3.9). It would be crucially important to take advantage of the large statistics and to keep the systematics under control.
- We may reach about 1σ combined significance for the un-tagged di-jet channel, as shown in Table 13 and in Eq. (3.15). We also considered the correlation with mis-tagged events from $h \to b\bar{b}$, $c\bar{c}$ channels, as discussed in Sec. 3.4.2
- Assuming the SM Vh production, our results can be translated to upper bounds on the branching fractions of 4 and 15 times the SM values for BR($h \to gg$) and BR($h \to c\bar{c}$), respectively, at 95% CL, seen in Eqs. (3.18) and (3.19).
- Exploiting our results, indirect upper bounds on light-quark Yukawa couplings can be extracted, as summarized in Table 16, and compared with the currently existing literature.
- We pointed out that there are other variables to explore. Kinematic discriminants like TvQ and ϕ_{Zh} as discussed in Sec. 3.3 may be among them. In the hope to improve

the simple cut-based analyses, multiple variable methods like BDT and NN would be promising. Addition of other production channels such as VBF and $t\bar{t}h$ will also help to strengthen the bounds.

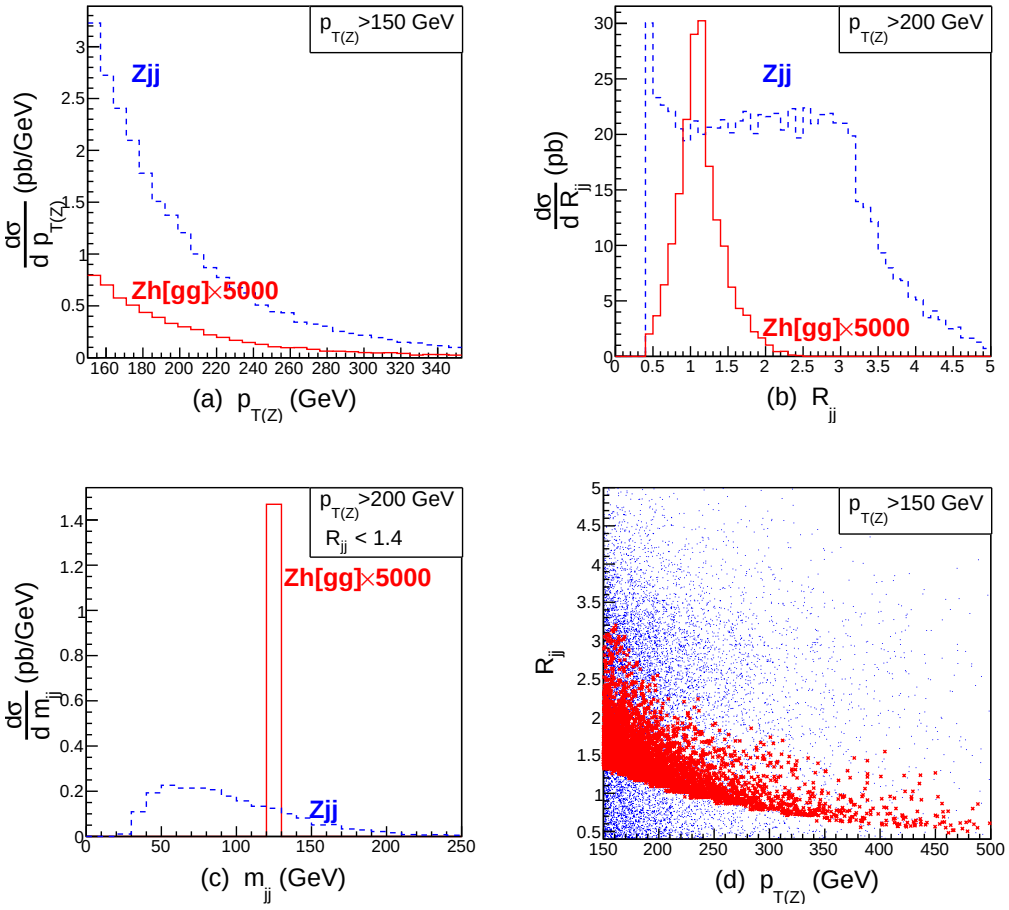

Figure 12: Kinematical distributions of the signal process $pp \to Zh, h \to gg$ (solid curves, scaled up by a factor of 5000) and the leading background $pp \to Zjj$ (dashed curves) for (a) $p_{T(Z)}$, (b) R_{jj}, (c) m_{jj}, and (d) event scatter plot in $R_{jj} - p_{T(Z)}$ plane, with the (red) dense band with crosses as the signal events and (blue) dots as the background. Generator level cuts of Eqs. (3.3) and (3.4) have been applied.

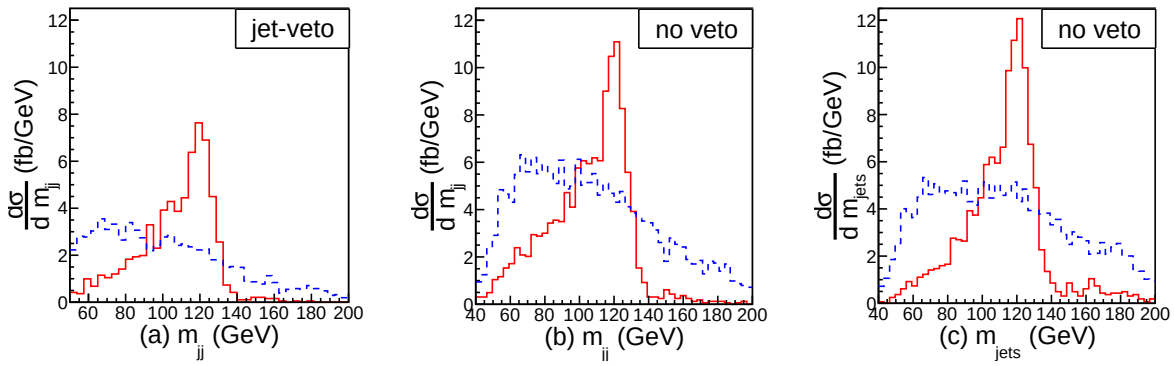

Figure 13: Invariant mass distributions m_{jj} of the signal process $pp \to Zh, h \to gg, Z \to \ell\ell$ (solid curves, scaled up by a factor of 5000) and the leading background $pp \to Zjj$ (dashed curves) for (a) with 2 jets only, (b) with 2 leading jets to reconstruct m_{jj}, (c) with 2 leading jets plus other jets together to reconstruct m_{jets}. All selection cuts as in Sec. 3.2.1 except for m_h cut are applied.

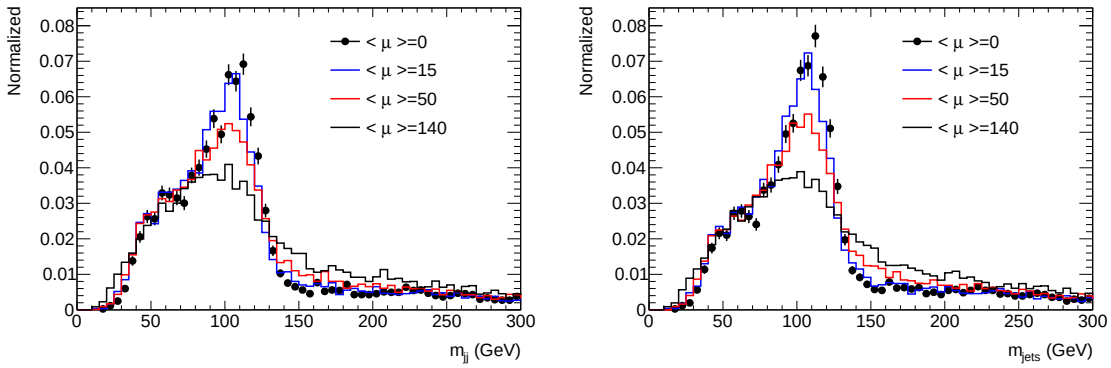

Figure 14: Invariant mass distributions constructed from (a) two-jet events and (b) three-jet events with different pile-up values $\langle\mu\rangle = 0, 15, 50, 140$, respectively.

cut eff (%)	$q\bar{q} \to Zh \to \ell^+\ell^- gg$	$gg \to Zh \to \ell^+\ell^- gg$	$q\bar{q} \to Zjj \to \ell^+\ell^- jj$
σ (fb)	3.9×10^{-1}	2.0×10^{-1}	$1.2{\times}10^4$
2 leptons	59%	52%	40%
≥ 2 jets	51%	49%	32%
$70 < m_{ll} < 110$	50%	49%	31%
$p_{T(\ell\ell)} > 200$ GeV	26%	23%	16%
$R_{j_1 j_2} < 1.4$	21%	12%	5.3%
$95 < m_h < 150$ GeV	14%	7.6%	1.9%
final (fb)	5.4×10^{-2}	1.5×10^{-2}	$2.4{\times}10^2$

Table 8: The consecutive cut efficiencies for signal $\ell^+\ell^-\ jj$ and dominant background processes at the LHC.

cut eff (%)	$q\bar{q} \to Wh \to \ell\nu gg$	$q\bar{q} \to Wjj \to \ell\nu jj$	$t\bar{t} \to \ell\nu jjb\bar{b}$
σ (fb)	2.3	$1.0{\times}10^5$	$1.5{\times}10^4$
$\not{E}_T > 30$ GeV	94%	87%	93%
1 lepton	72%	52%	62%
$p_{T(\ell\nu)} > 200$ GeV	39%	24%	26%
≥ 2 jets	35%	20%	22%
$R_{j_1 j_2} < 1.4$	27%	6.8%	11%
$95 < m_h < 150$ GeV	18%	2.5%	2.5%
final (fb)	4.1×10^{-1}	2.5×10^3	3.7×10^2

Table 9: The consecutive cut efficiencies for signal $\ell^\pm \not{E}_T\ jj$ and dominant background processes at the LHC.

cut eff (%)	$q\bar{q} \to Zh \to \nu\nu gg$	$gg \to Zh \to \nu\nu gg$	$q\bar{q} \to Zjj \to \nu\nu jj$
σ (fb)	1.2	6.0×10^{-1}	$3.6{\times}10^{4}$
$\not{E}_T > 200$ GeV	49%	44%	42%
≥ 2 jets	45%	43%	35%
$R_{j_1 j_2} < 1.4$	36%	25%	12%
$95 < m_h < 150$ GeV	23%	15%	4.5%
final (fb)	2.7×10^{-1}	8.9×10^{-2}	1.6×10^{3}

Table 10: The consecutive cut efficiencies for signal $\not{E}_T\ jj$ and dominant background processes at the LHC.

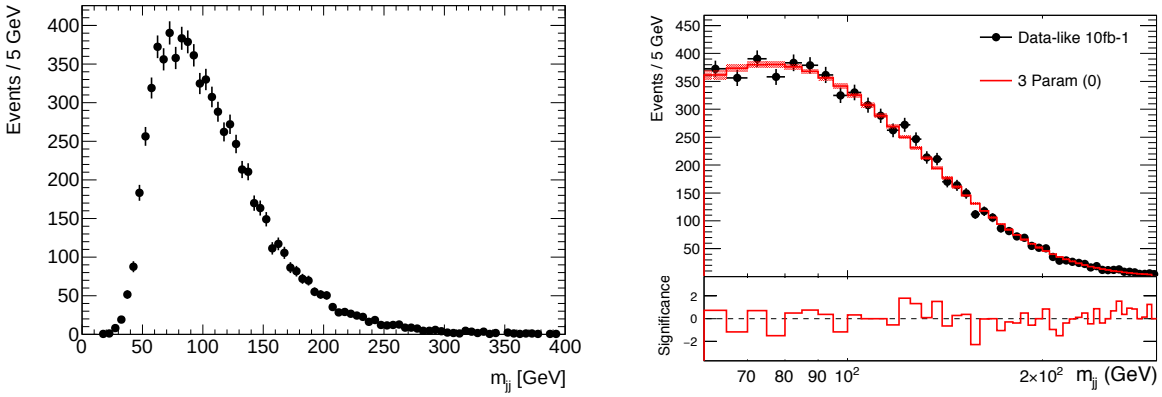

Figure 15: Invariant mass distribution m_{jj} for $Z(\ell^+\ell^-)$+jets at the 14 TeV LHC for (a) MC simulated events normalized to 10 fb^{-1}, and (b) fitted spectrum from three-parameter ansatz function in Eq. (3.7) range from 60 GeV to 300 GeV (solid curve).

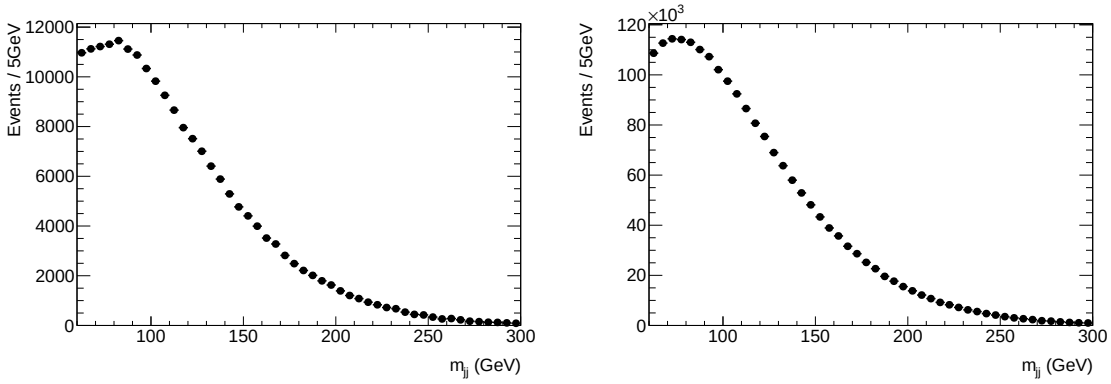

Figure 16: Generated distribution from three-parameter ansatz function in Eq. (3.7) for m_{jj} with (a) 300 fb^{-1}, (b) and 3000 fb^{-1} (right).

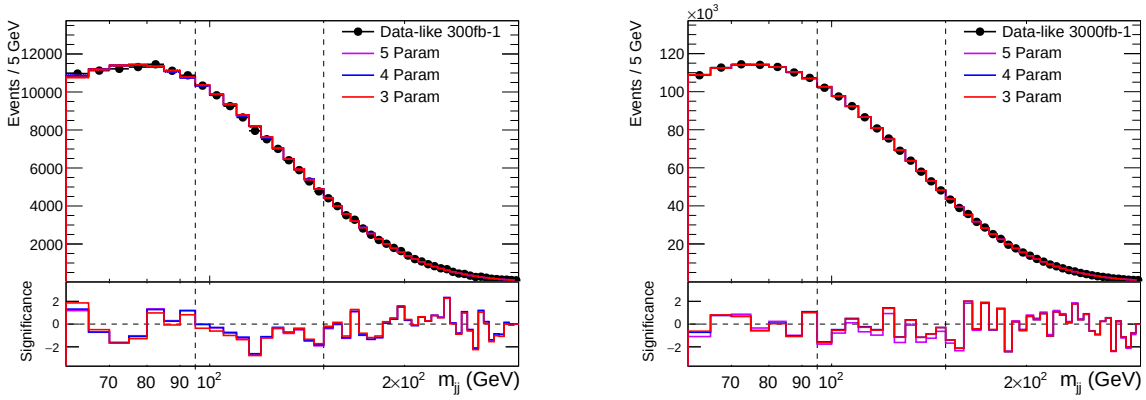

Figure 17: Fitted results for 300 fb^{-1} (left) and 3000 fb^{-1} (right).

Background	300 fb^{-1}	3000 fb^{-1}
Expectation	8.29×10^4	8.26×10^5
3-parameter	$(8.39 \pm 0.05) \times 10^4$	$(8.28 \pm 0.01) \times 10^5$
4-parameter	$(8.38 \pm 0.05) \times 10^4$	$(8.27 \pm 0.01) \times 10^5$
5-parameter	$(8.39 \pm 0.04) \times 10^4$	$(8.29 \pm 0.01) \times 10^5$
Uncertainty	1.32%	0.21%

Table 11: Fitted results for the background rates from various fitting functions as in Eqs. (3.7) and (3.8).

3000 fb^{-1}	True	$[60, 300]$ GeV	$[70, 250]$ GeV	$[80, 200]$ GeV
3-parameter	8.26×10^5	$(8.28 \pm 0.01) \times 10^5$	$(8.26 \pm 0.03) \times 10^5$	$(8.27 \pm 0.05) \times 10^5$

Table 12: Fitted results for the background rate from various fitting ranges by the fitting function in Eq. (3.7).

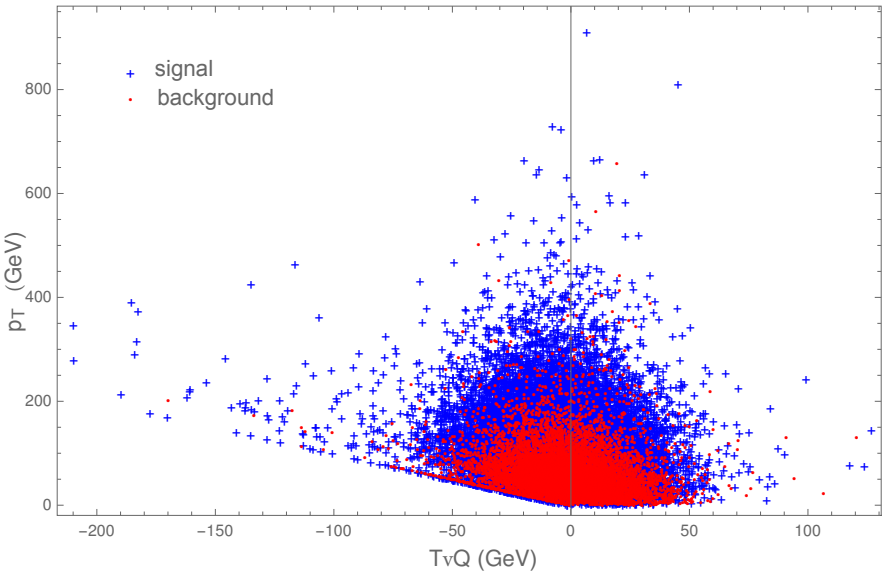

Figure 18: Scatter plot of 10000 events for the signal (blue crosses) and background (red dots) in the visible $p_T - TvQ$ plane.

σ (fb)	$\ell^+\ell^- + jj$	$\ell^\pm + \not{E}_T + jj$	$\not{E}_T + jj$	combined
Vh signal	7.0×10^{-2}	4.1×10^{-1}	3.6×10^{-1}	
Vjj background	2.4×10^{2}	2.5×10^{3}	1.6×10^{3}	
$\mathcal{S}$	0.25	0.61	0.49	0.82
$\mathcal{S}_{\text{sys}}$	0.09	0.17	0.17	0.26

Table 13: Signal significance achieved from each channel and combined results for both statistics and systematics dominance.

ϵ_{ai}	b-quark	c-quark	$j = g, u, d, s$
b-tag	70%	20%	1.25%
c-tag	13%	19%	0.50%
un-tag $j'j'$	17%	61%	98.25%

Table 14: Flavor tagging efficiency

e_{ai}	$h \to b\bar{b}$	$h \to c\bar{c}$	$h \to jj$
bb-tag	99.6%	0.4%	0%
cc-tag	90.4%	9.6%	0%
un-tag j'	16%	10%	74%

Table 15: Fraction of SM decay channels

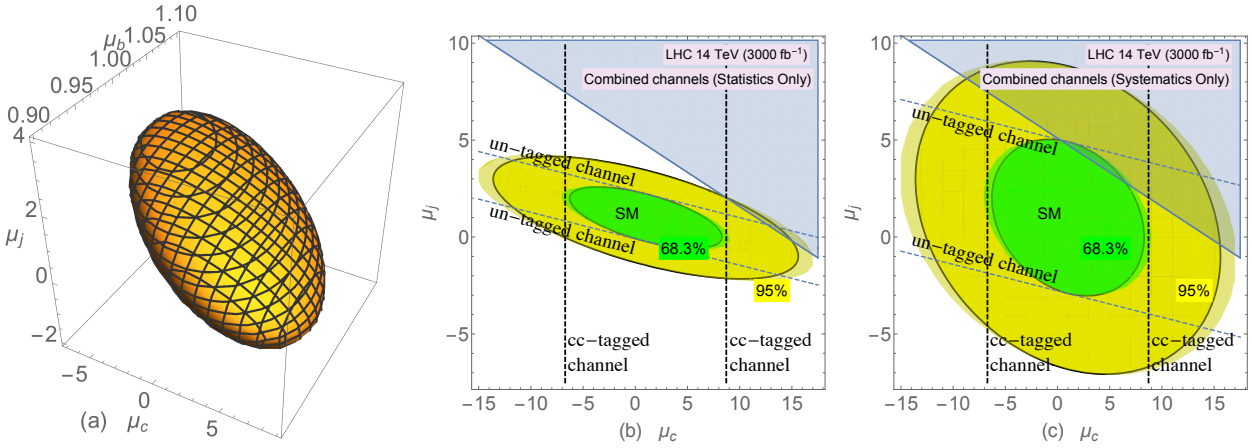

Figure 19: Signal strengths in correlated regions for (a) 1σ contour in 3-dimension (μ_b, μ_c, μ_j), (b) and (c) contours in μ_c-μ_j plane, for statistics only and including systematic uncertainties, respectively. The shadowed contour regions are the projection of the 3D contour (μ_b, μ_c, μ_j) onto the μ_c-μ_j plane at 1σ and 2σ, and the solid ovals are for fixing $\mu_b = 1$. The grey triangle area at the upper right corner is unphysical BR($h \to bb$) + BR($h \to cc$) + BR($h \to jj$) > 1.

$\mathcal{L}(\text{fb}^{-1})$	$\overline{\kappa}_u$ (κ_u)	$\overline{\kappa}_d$ (κ_d)	$\overline{\kappa}_s$ (κ_s)
300 (un-tagged $j'j'$)	1.2 (2600)	1.2 (1200)	1.2 (61)
3000 (un-tagged $j'j'$)	0.65 (1500)	0.65 (680)	0.65 (34)
Current Global Fits [162]	0.98 (2200)	0.97 (1000)	0.70 (37)
300 [158]	0.36 (820)	0.41 (430)	
3000 [152]			0.58 (30)

Table 16: Extrapolated upper bounds at 95% CL on the light-quark Yukawa couplings $\overline{\kappa}_q = y_q/y_b^{\text{SM}}$ $(\kappa_q = y_q/y_q^{\text{SM}})$ for $q = u, d, s$.

4.0 ANTLER TOPOLOGY FOR MASS DETERMINATION

This chapter is a bit digression from the theme of Higgs measurements at colliders. The study is however in the same spirit and methodology of making use of the clean kinematic reconstruction at lepton colliders. Instead of SM properties, we target directly at a BSM scenario where the probable dark matter candidate particle is pair produced from cascade decay of heavier resonances. The lepton collider here offers the opportunity to determine the masses of these new particles to a high precision.

4.1 MOTIVATION

With the discovery of the Higgs boson at the LHC [81], we know that the SM as an effective field theory can be valid up to a very high scale. Nevertheless, there are strong indications that the SM is incomplete. Certain observed particle physics phenomena cannot be accounted for within the SM. Among them, the discovery and characterization of the dark matter (DM) particle may be one of the most pressing issues.

The existence of dark matter has been well established through a combination of galactic velocity rotation curves [82], the cosmic microwave background [83], Big Bang nucleosynthesis [84], gravitational lensing [85], and the bullet cluster [86]. As a result of these observations, we know that dark matter is non-baryonic, electrically neutral and composes roughly 23% of the energy and 83% of the matter of the universe.

Among the many possibilities for dark matter [87], weakly interacting massive particles (WIMPs) are arguably the most attractive because of the so-called WIMP miracle: to get

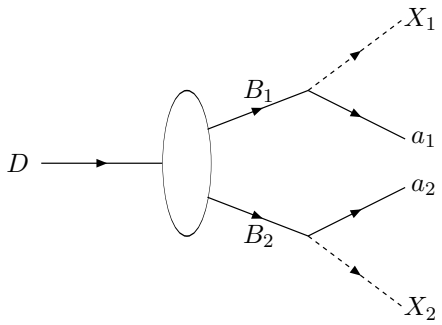

Figure 20: The antler decay diagram of a heavy particle D into two visible particles a_1 and a_2 and two invisible particles X_1 and X_2 through on-shell intermediate particles B_1 and B_2.

the relic abundance right, a WIMP mass is roughly

$$M_{\rm WIMP} \lesssim \frac{g^2}{0.3}\ 1.8\ {\rm TeV}, \tag{4.1}$$

which miraculously coincides with the new physics scale expected from the "naturalness" argument for electroweak physics. Therefore, there is a high hope that the search for a dark matter particle may be intimately related to the discovery of TeV scale new physics.

Direct searches of weak scattering of dark matter off nuclear targets in underground labs have been making great progress in improving the sensitivity to the DM mass and couplings, most recently by the XENON [88], LUX [89] and SuperCDMS [90] collaborations. WIMPs can also be produced at colliders either directly in pairs or from cascade decays of other heavier particles. Since a WIMP is non-baryonic and electrically neutral, it does not leave any trace in the detectors and thus only appears as missing energy. In order to establish a DM candidate convincingly, it is ultimately important to reach consistency between direct searches and collider signals for the common parameters of mass, spin and coupling strength.

It is very challenging to determine the missing particle mass at colliders due to the under-constrained kinematical system with two missing particles in an event. It is particularly difficult at hadron colliders because of the unknown partonic c.m. energy and frame. There exist many attempts to determine the missing particle mass at the LHC, such as endpoint

methods [91], polynomial methods [92], M_{T2} methods [93], and the matrix element method [94]. Recently, we studied the "antler decay" diagram [95], as illustrated in Fig. 20 with a resonant decay of a heavy particle D into two parity-odd particles (B_1 and B_2) at the first step, followed by each B_i's decay into a missing particle X_i and a visible particle a_i. In our study, we found that a resonant decay through the antler diagram develops cusps in some kinematic distributions and the cusp positions along with the endpoint positions determine the missing particle mass as well as the intermediate particle mass [95, 96, 97].

As motivated earlier, we focus on lepton colliders [98, 99, 100, 101], in which the antler topology applies. The initial state is well-defined with fixed c.m. energy and c.m. frame. This allows various antler processes without going through a resonant decay of a heavy particle D. We consider kinematic variables such as the angle and the energy of a visible particle for the mass determination. We also show that the invariant mass of two invisible particles, which can be indirectly reconstructed using the recoil mass technique, is crucial for the mass measurement and the SM background suppression. The energy sum of the two visible particles or of the two invisible particles will also be shown to be equally powerful. At a linear e^+e^- collider, the available beam polarization can additionally be used to suppress the SM background and enhance the sensitivity of the mass measurement.

Two common methods of the missing mass measurement have been studied in the literature for e^+e^- collisions:

1. The lepton energy endpoints in cascade decays [102];
2. The photon energy endpoint in the direct WIMP pair production associated with a photon [103].

In comparison, we find that our results from the antler topology can be at least comparable to the energy endpoint method and do much better than the single photon approach. For the sake of illustration, we will concentrate on the minimal supersymmetric standard model (MSSM) and consider the scenario where the lightest neutralino $\tilde{\chi}_1^0$ is the lightest supersymmetric particle (LSP) and, therefore, stable in the framework of a R-parity conserving scenario. We consider two MSSM processes that satisfy the antler topology: pair production of scalar muons (smuons) and that of charginos. In order to be as realistic as possible

with the kinematical construction, we analyze the effects of the initial state radiation (ISR), beamstrahlung, acceptance cuts, and detector resolutions on the observables. We adopt the log-likelihood method based on Poisson statistics to quantify the precision of the mass measurements. We find that this method optimizes the sensitivity to the mass parameters in the presence of these realistic effects.

We note that the scanning through the pair production threshold could give a much more accurate determination for the intermediate parent mass [104]. With this as an input, one could improve the measurement of the missing particle mass by the energy endpoint method or by the Antler technique. However, the threshold scan would require *a priori* knowledge of the intermediate particle mass, and would need more integrated luminosity to reach such a high sensitivity [104]. Our proposed method does not assume to know any masses, and our outputs would benefit the design of the threshold scan.

For benchmark scenarios, we first show smuon pair production as an example of massless visible particles in section 4.2. We reproduce the expected kinematical features numerically and illustrate the effects of the acceptance cuts on the final state observable particles. Other realistic effects including full spin correlation, SM backgrounds, ISR, beamstrahlung, and detector resolutions are considered. Adopting the log-likelihood method based on the Poisson probability density, we quantify the accuracy with which the missing particle mass measurement may be determined in section 4.2.4. In section 4.3, chargino pair production is studied, as an example of massive visible particles with a hadronic final state. In section 4.4, we give a summary and draw our conclusions.

4.2 MASSLESS VISIBLE PARTICLE CASES: SMUON PAIR PRODUCTION

We start from a state with a fixed c.m. energy $\sqrt{s}$, which produces two massive particles B_1 and B_2, followed by each B's decay into a visible particle a and an invisible heavy particle

X, as depicted in Fig. 20. In e^+e^- collisions, it is realized as

$$\begin{aligned} e^+e^- \;\; &\to \;\; B_1 + B_2, \\ &\qquad B_1 \to a_1 + X_1, \quad B_2 \to a_2 + X_2. \end{aligned} \tag{4.2}$$

For simplicity, we further assume that B_1 and B_2 (X_1 and X_2) are identical particles to each other:

$$m_{B_1} = m_{B_2} \equiv m_B, \quad m_{X_1} = m_{X_2} = m_X. \tag{4.3}$$

We review the kinematic cusps and endpoints of antler processes in Appendix B. There we present the general analytic expressions for six kinematic variables in terms of the masses.

For the massless observable particles a_1 and a_2 in this section, we present the feature based on the previous discussions and demonstrate the observable aspects for the missing mass measurements at the ILC. Throughout the chapter, we choose to show the results for the c. m. energy

$$\sqrt{s} = 500\,\text{GeV}.$$

4.2.1 The kinematics of cusps and endpoints

A lepton collider is an ideal place to probe the charged slepton sector of the MSSM. To illustrate the basic features of cusps and endpoints at the ILC, we consider smuon pair production. In principle, the scalar nature of the smuon can be determined by the shape of the total cross section near threshold and the angular distributions of the final muons [105]. There are two kinds of smuons, $\tilde{\mu}_L$ and $\tilde{\mu}_R$, scalar partners of the left-handed and right-handed muons respectively. A negligibly small mass of the muon suppresses the left-right mixing and thus makes $\tilde{\mu}_L$ and $\tilde{\mu}_R$ the mass-eigenstates. The smuon pair production in e^+e^- collisions is via s-channel diagrams mediated by a photon or a Z boson. Since the exchanged particles are vector bosons, the helicities of e^+ and e^- are opposite to each other, and only two kinds of pairs, $\tilde{\mu}_R^+\tilde{\mu}_R^-$ and $\tilde{\mu}_L^+\tilde{\mu}_L^-$, are produced. If the lightest neutralino $\tilde{\chi}_1^0$ has a dominant Bino component, $\tilde{\mu}_R$ predominantly decays into $\mu\tilde{\chi}_1^0$. The decay of $\tilde{\mu}_L \to \mu\tilde{\chi}_1^0$

Label	$\tilde{\mu}_R$	$\tilde{\mu}_L$	$\tilde{\chi}_1^0$	$\tilde{\chi}_2^0$	$\tilde{\chi}_3^0$	$\tilde{\chi}_4^0$	$\tilde{\chi}_1^\pm$	$\tilde{\chi}_2^\pm$
`Case-A` (`Case-B`)	158	636 (170)	141	529	654	679	529	679
`Case-C`	–	–	139	235	504	529	235	515

Table 17: Illustrative SUSY mass spectrum for `Case-A`, `Case-B` (as introduced in Sec. 4.2.1) and `Case-C` (as introduced in Sec. 4.3). All of the masses are in units of GeV.

is also sizable. At the ILC, the process $e^+e^- \to \tilde{\mu}_R\tilde{\mu}_R/\tilde{\mu}_L\tilde{\mu}_L \to \mu\tilde{\chi}_1^0 + \mu\tilde{\chi}_1^0$ has a substantial rate. The final state we observe is

$$e^+e^- \to \mu^+\mu^- + \not{E}. \tag{4.4}$$

This is one good example of the antler process. However, we note that the leading SM process, W^+W^- production followed by $W \to \mu\nu_\mu$, is also of the antler structure.

For illustrative purposes of the signals, we consider two benchmark points for the MSSM parameters, called `Case-A` and `Case-B`, as listed in Table 17. These two cases have the same mass spectra, except for the $\tilde{\mu}_L$ mass. In `Case-A`, $\tilde{\mu}_L$ is too heavy for the pair production at $\sqrt{s} = 500\,\text{GeV}$. We have a simple situation where the new physics signal for the final state in Eq. (4.4) involves only $\tilde{\mu}_R\tilde{\mu}_R$ production. In `Case-B`, the $\tilde{\mu}_L$ mass comes down close to the $\tilde{\mu}_R$ mass, with a mass gap of about 10 GeV. In this case with $m_{\tilde{\mu}_R} \simeq m_{\tilde{\mu}_L}$, the cross section of $\tilde{\mu}_R\tilde{\mu}_R$ production is compatible with that of $\tilde{\mu}_L\tilde{\mu}_L$ production. This is because the left-chiral and right-chiral couplings of the smuon to the Z boson, say $g^L_{\tilde{\mu}\tilde{\mu}Z}$ and $g^R_{\tilde{\mu}\tilde{\mu}Z}$ respectively, are accidentally similar in size:

$$g^L_{\tilde{\mu}\tilde{\mu}Z} = \frac{-1 + 2\sin^2\theta_W}{2\sin\theta_W\cos\theta_W} \approx -0.64, \quad g^R_{\tilde{\mu}\tilde{\mu}Z} = \frac{\sin\theta_W}{\cos\theta_W} \approx 0.55. \tag{4.5}$$

In `Case-B`, three signals from $\tilde{\mu}_R\tilde{\mu}_R$, $\tilde{\mu}_L\tilde{\mu}_L$, and W^+W^- all have the same antler decay topology. The goal is to disentangle the information and achieve the mass measurements of $\tilde{\mu}_R$, $\tilde{\mu}_L$, and $\tilde{\chi}_1^0$.

It is noted that the LHC searches for slepton direct production does not reach enough sensitivity with the current data yet [106] and would be very challenging in Run-II as well

$\sqrt{s}$	500 GeV		
Production channel	$\tilde{\mu}_R\tilde{\mu}_R$	$\tilde{\mu}_L\tilde{\mu}_L$	W^+W^-
input (m_B, m_X)	$(158, 141)$	$(170, 141)$	$(m_W, 0)$
$\lvert\cos\Theta\rvert_{\max}$	0.77	0.73	0.95
$(m_{\mu\mu}^{\min}, m_{\mu\mu}^{\text{cusp}}, m_{\mu\mu}^{\max})$	$(0, 12, 91)$	$(0, 21, 137)$	$(0, 13, 487)$
$(m_{\text{rec}}^{\min}, m_{\text{rec}}^{\text{cusp}}, m_{\text{rec}}^{\max})$	$(408, 445, 488)$	$(363, 413, 479)$	$(0, 13, 487)$
$(E_\mu^{\min}, E_\mu^{\max})$	$(6, 46)$	$(11, 69)$	$(7, 243)$
$(E_{\mu\mu}^{\min}, E_{\mu\mu}^{\text{cusp}}, E_{\mu\mu}^{\max})$	$(12, 52, 92)$	$(21, 79, 137)$	$(13, 250, 487)$

Table 18: The values of various kinematic cusps and endpoints as seen in Fig. 21, for the mass parameters in Table 17. All of the masses and energies are in units of GeV.

for the parameter choices under consideration, due to the small signal cross section, large SM backgrounds, and the disfavored kinematics of the small mass difference. On the other hand, once crossing the kinematical threshold at a lepton collider, the slepton signal could be readily established.

In Table 18, we list the values of various kinematic cusps and endpoints for the five variables discussed above. The mass spectra of the $\tilde{\mu}_R\tilde{\mu}_R$ antler and the W^+W^- antler apply to both `Case-A` and `Case-B`, while that of $\tilde{\mu}_L\tilde{\mu}_L$ applies only to `Case-B`. With the given masses, all of the minimum, cusp, and maximum positions are determined. They are considerably different from each other, indicating important complementarity of these kinematic variables.

In Fig. 21, we show the normalized distributions of (a) $m_{\mu\mu}$, (b) m_{rec}, (c) $\cos\Theta$, (d) E_μ, and (e) $E_{\mu^+} + E_{\mu^-}$ for $\tilde{\mu}_R\tilde{\mu}_R$, $\tilde{\mu}_L\tilde{\mu}_L$, and W^+W^- production at the ILC with a c.m. energy of 500 GeV. To appreciate the striking features of the distributions, we have only considered the kinematics here. The full results including spin correlations, initial state radiation (ISR), beamstrahlung, and detector smearing effects will be shown, beginning in section 3.3. First, the m_{aa} distributions for $\tilde{\mu}_R\tilde{\mu}_R$, $\tilde{\mu}_L\tilde{\mu}_L$, and W^+W^- production do not show a clear cusp.

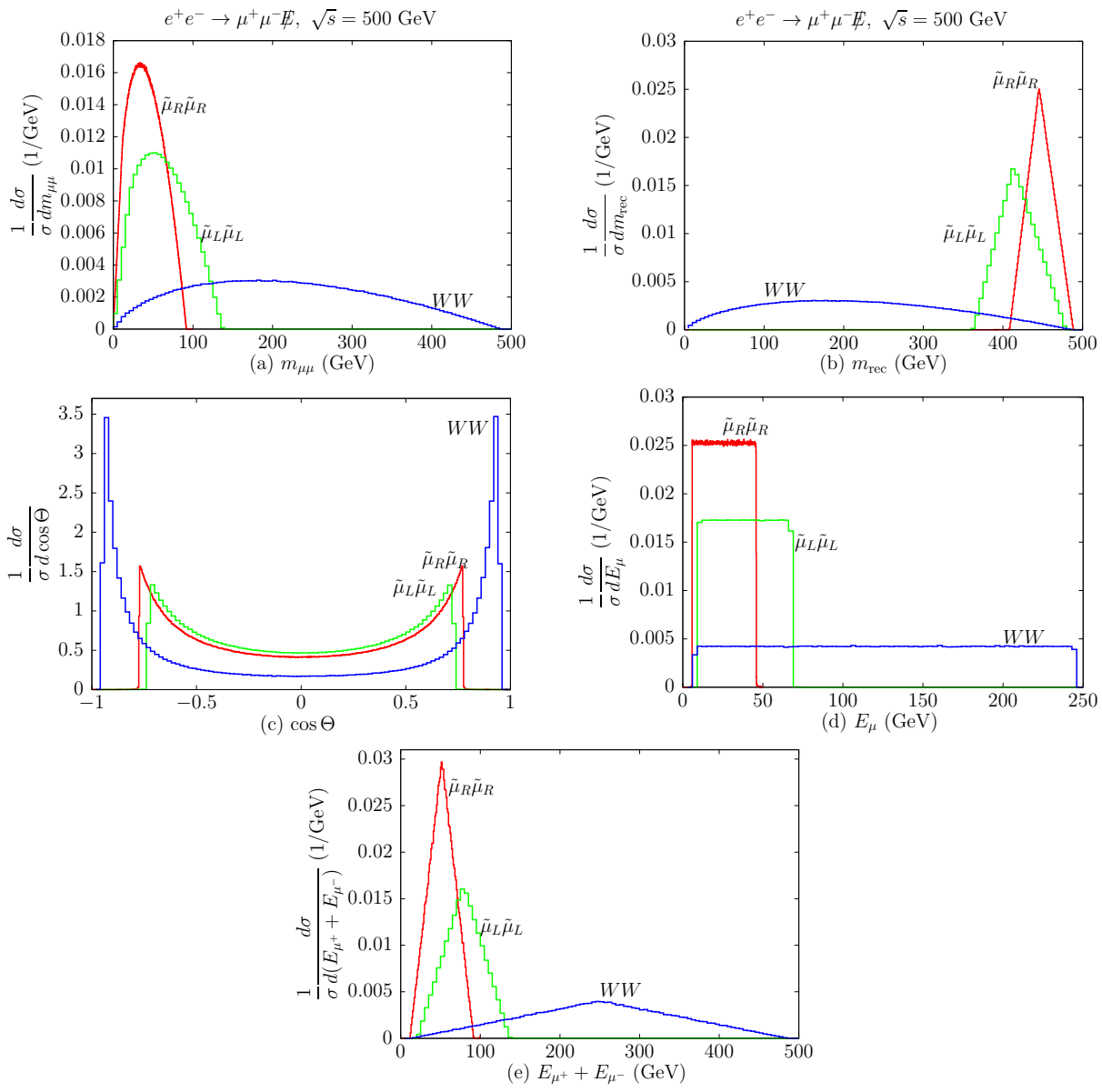

Figure 21: The normalized distributions of (a) $m_{\mu\mu}$, (b) $m_{\rm rec}$, (c) $\cos\Theta$, (d) E_μ and (e) $E_{\mu^+} + E_{\mu^-}$ for the three cases in Table 18, *i.e.*, for $\tilde{\mu}_R\tilde{\mu}_R$, $\tilde{\mu}_L\tilde{\mu}_L$ and W^+W^- production at $\sqrt{s} = 500\,\text{GeV}$. Here we consider only the kinematics without spin correlations.

This is because the c.m. energy is too high compared with the intermediate mass to reveal the m_{aa} cusp, which would become pronounced when $m_B > 0.44\sqrt{s}$ [95]. For $B = \tilde{\mu}_R$, a sharp m_{aa} cusp requires $\sqrt{s} \lesssim 360\,\text{GeV}$. On the contrary, the $m_{\rm rec}$ distributions for $\tilde{\mu}_R\tilde{\mu}_R$

and $\tilde{\mu}_L\tilde{\mu}_L$ in Fig. 21(b) are of the shape of a sharp triangle. This is attributed to the massive X. For W^+W^- production, the missing particles are massless neutrinos, therefore, the m_{aa} distribution is the same as the $m_{\rm rec}$ distribution.

The $\cos\Theta$ distributions of $\tilde{\mu}_R\tilde{\mu}_R$, $\tilde{\mu}_L\tilde{\mu}_L$, and W^+W^- in Fig. 21(c) present the same functional behavior, proportional to $1/\sin^3\Theta$. There are two sharp points where the cusp and the maximum merge, which correspond to $\pm|\cos\Theta|_{\rm max}$. The $\tilde{\mu}_R\tilde{\mu}_R$ and $\tilde{\mu}_L\tilde{\mu}_L$ processes have similar values of $|\cos\Theta|_{\rm max}$, while the W^+W^- process peaks at a considerably larger value. Figure 21(d) shows the energy distribution of one visible particle μ. The distributions for the smuon signals are flat due to their scalar nature, while the flat distribution for the W^+W^- channel is artificial due to the neglect of spin correlation. We will include the full spin effects from section 4.2.3 and on.

In principle, the two measurements of $E_\mu^{\rm min}$ and $E_\mu^{\rm max}$ can determine the two unknown masses m_B and m_X. However the minimum of E_a can be below the detection threshold as in the $\tilde{\mu}_R$ case of $E_\mu^{\rm min} \simeq 5.8\,{\rm GeV}$. One may thus need another independent observable to determine all the masses. In addition, over-constraints on the involved masses are very useful in establishing the new physics model.

The distribution of $E_{\mu\mu}(\equiv E_{\mu^+}+E_{\mu^-})$ in Fig. 21(e) is different from the individual energy distribution: the former is triangular while the latter is rectangular. For $\tilde{\mu}_R\tilde{\mu}_R$ and $\tilde{\mu}_L\tilde{\mu}_L$, the E_{aa} distributions are localized so that the pronounced cusp is easy to identify. For W^+W^-, however, the E_{aa} distribution is widespread.

In order to further understand the singular structure, we examine four representative configurations in terms of $(\cos\theta_1, \cos\theta_2)$, where θ_1 and θ_2 are the polar angle of a_1 and a_2 in the rest frame of their parent particles B_1 and B_2, respectively. The correspondence of each corner to a singular point is as follows:

1D configuration	m_{aa}	$m_{\rm rec}$	E_{aa}	E_{XX}
(i) $\overset{a_2}{\Longleftarrow}$ $\overset{B_2}{\longleftarrow}$ $\overset{e^+e^-}{\bullet}$ $\overset{B_1}{\longrightarrow}$ $\overset{a_1}{\Longrightarrow}$	max	min	max	min
(ii) $\overset{a_2}{\Longrightarrow}$ $\overset{B_2}{\longleftarrow}$ $\overset{e^+e^-}{\bullet}$ $\overset{B_1}{\longrightarrow}$ $\overset{a_1}{\Longleftarrow}$	cusp	max	min	max
(iii) $\overset{a_2}{\Longrightarrow}$ $\overset{B_2}{\longleftarrow}$ $\overset{e^+e^-}{\bullet}$ $\overset{B_1}{\longrightarrow}$ $\overset{a_1}{\Longrightarrow}$	min	cusp	cusp	cusp
(iv) $\overset{a_2}{\Longleftarrow}$ $\overset{B_2}{\longleftarrow}$ $\overset{e^+e^-}{\bullet}$ $\overset{B_1}{\longrightarrow}$ $\overset{a_1}{\Longleftarrow}$	min	cusp	cusp	cusp

(4.6)

4.2.2 The effects of acceptance cuts

In a realistic experimental setting, the previously discussed kinematical features may be smeared, rendering the cusps and endpoints less effective for extracting the mass parameters. We now study the effects of the acceptance cuts.

We first explore the effects due to a missing transverse momentum ($\not{p}_T$) cut, which is essential to suppress the dominant SM background of $e^+e^- \to e^+e^-\mu^+\mu^-$ with the outgoing e^+e^- going down the beam line and not detected. Obviously, the $\not{p}_T$ cut removes some events, reducing the event rate. In addition, the $\not{p}_T$ cut does not apply evenly over the distribution. The positions of the cusp and endpoints can be shifted in some cases.

In Fig. 22, we show the effects of a $\not{p}_T$ cut on the distributions of $m_{\mu\mu}$, $m_{\rm rec}$, $\cos\Theta$, E_μ, and $E_{\mu\mu}$. We normalize each distribution by the total cross section without other kinematic cuts. First, the $m_{\mu\mu}$ distributions with various $\not{p}_T$ cuts are shown in Fig. 22(a) for $\sqrt{s} = 500\,\text{GeV}$ and in Fig. 22(f) for $\sqrt{s} = 350\,\text{GeV}$. The $m_{\mu\mu}$ cusp in the higher c.m. energy case does not present a notable feature while the lower energy case with $\sqrt{s} = 350\,\text{GeV}$ has a more pronounced cusp shape. With a $\not{p}_T > 10\,\text{GeV}$ cut, the m_{aa} distribution retains its triangular shape, but starts to lose the true cusp and maximum positions. The shift is a few GeV. If $\not{p}_T > 20\,\text{GeV}$, the sharp cusp is smeared out and the $m_{\mu\mu}^{\rm max}$ position is shifted by about 10 GeV. In both cases, the $m_{\mu\mu}^{\rm min}$ remains intact. The $m_{\rm rec}$ distribution in Fig. 22(b), on the contrary, keeps its triangular shape even with a high $\not{p}_T$ cut. It is interesting to note that the $\not{p}_T$ cut shifts the $m_{\rm rec}^{\rm min}$ and $m_{\rm rec}^{\rm max}$ while keeping the $m_{\rm rec}^{\rm cusp}$ position fixed. Figure 22(e) presents the distribution of the summed energy of the two visible particles, which are still triangular after the $\not{p}_T$ cut. The cusp position is retained, but the minimum and maximum positions are shifted.

We note that $\not{p}_T$ cut does not affect the positions of the variables $m_{\mu\mu}^{\rm min}$, $m_{\rm rec}^{\rm cusp}$, and $E_{\mu\mu}^{\rm cusp}$ appreciably, which all correspond to the kinematical configurations (*iii*) and (*iv*) in Eq. (17). Here the two visible particles (a_1a_2) move in the same direction, and two invisible particles (X_1X_2) move also in the same direction, opposite to the a_1a_2 system. A $\not{p}_T$ cut would not change the system configuration. In contrast, for the configurations (*i*) and (*ii*) in Eq. (17), a_1 and a_2 are moving in the opposite direction, and a cut on the X_1X_2 system alters the

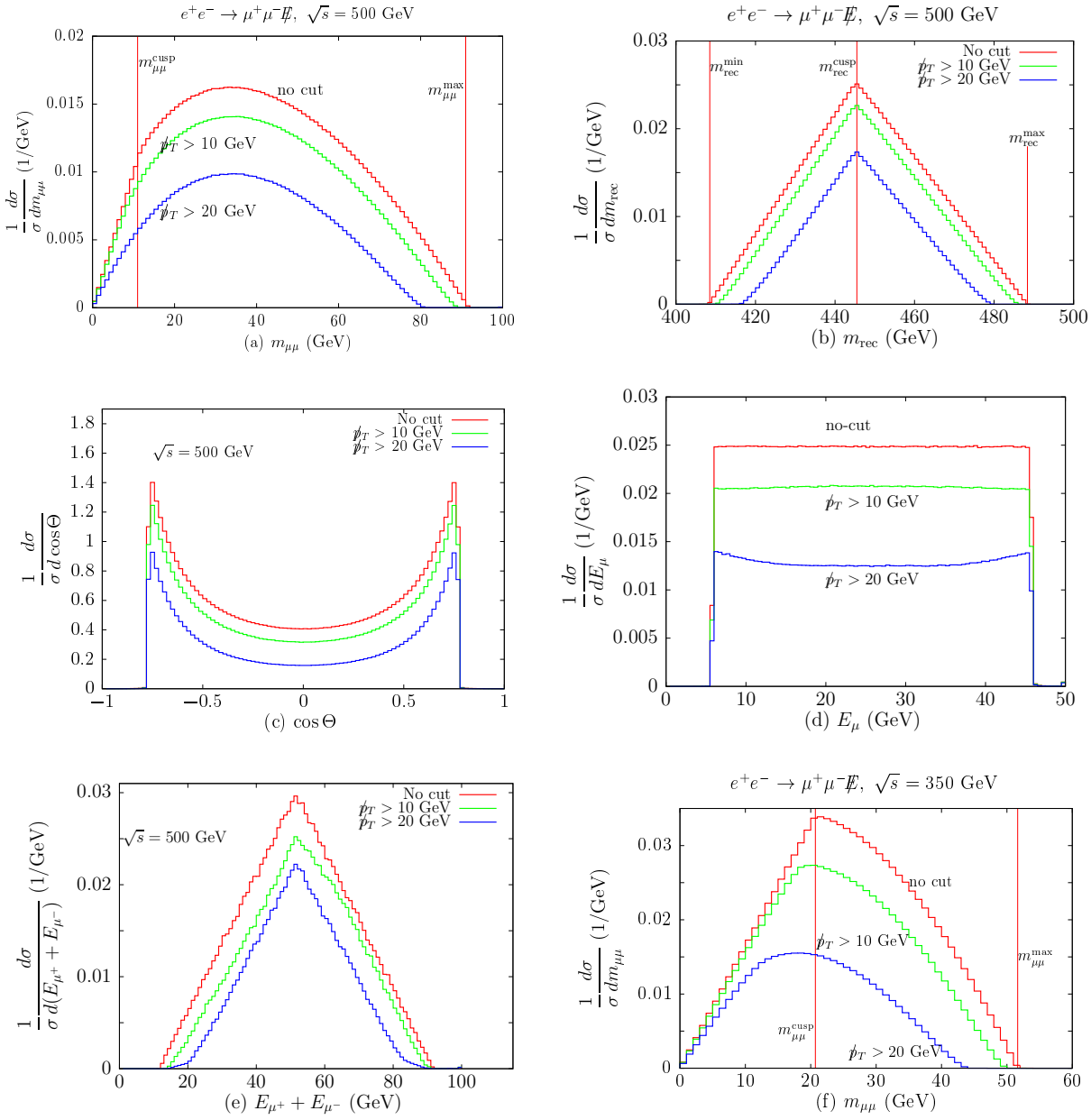

Figure 22: `Case-A` for $e^+e^- \to \tilde{\mu}_R\tilde{\mu}_R \to \mu^+\mu^- + \not{E}$. Effects due to various $\not{p}_T$ cuts on (a) $m_{\mu\mu}$, (b) $m_{\rm rec}$, (c) $\cos\Theta$, (d) E_μ, and (e) $E_{\mu^+} + E_{\mu^-}$ distributions without spin-correlation and other realistic effects at $\sqrt{s} = 500\,\text{GeV}$. Each distribution is normalized by the total cross section. Panel (f) for the $m_{\mu\mu}$ distribution is set to 350 GeV for comparison.

individual particle as well as the configuration appreciably.

The least affected variable is the $\cos\Theta$ distribution in Fig. 22(c). The $|\cos\Theta|_{\max}$ positions remain the same, and the $\not{p}_T$ cut removes the data nearly evenly all over the distribution. Figure 22(d) shows the E_μ distribution under the $\not{p}_T$ cut effects. Similar to the case of $\cos\Theta$, the $\not{p}_T$ cut reduces the whole rate roughly uniformly, and the box-shaped distribution is still maintained.

Figure 23 presents the five kinematic distributions with the effects of the E_a cut. The normalization is done with the total cross section without any cut. Two $m_{\mu\mu}$ distributions are presented, one for $\sqrt{s} = 500\,\text{GeV}$ in Fig. 23(a) and the other for $\sqrt{s} = 350\,\text{GeV}$ in Fig. 23(f). Both retain its maximum position after the E_a cut. However, the $m_{\mu\mu}$ cusp position is shifted by a sizable amount, approximately 10 GeV for $E_a > 15\,\text{GeV}$ cut at $\sqrt{s} = 350\,\text{GeV}$. This behavior is the same for the $E_{\mu\mu}$ distribution in Fig. 23(e). The m_{rec} distribution in Fig. 23(b) behaves oppositely: the maximum and cusp positions are shifted while the minimum position is retained. Therefore, the E_a cut does not change the one-dimensional configuration (i) of Eq. (4.6).

The $\cos\Theta$ distributions under the E_a cuts are shown in Fig. 23(c). The locations of $|\cos\Theta|_{\max}$ remain approximately the same, but the sharp cusps are reduced somewhat. Finally the E_a distribution in Fig. 23(d) shows the expected shift of its minimum into the lower bound on E_a. Note that some data satisfying $E_a > E_a^{\text{cut}}$ are also cut off, since the E_a cut has been applied to both of the final leptons. In summary, the acceptance cut distorts the kinematic distributions, and shifts the singular positions. When we extract the mass information from the endpoints, these cut effects must be properly taken into account.

4.2.3 Mass measurements with realistic considerations

4.2.3.1 Backgrounds and simulation procedure For our signal of $e^+e^- \to \mu^+\mu^- + \not{E}$, there are substantial SM backgrounds. The main irreducible SM background is W boson pair production, $e^+e^- \to W^+W^- \to \mu^+\nu_\mu\mu^-\bar{\nu}_\mu$. The next dominant mode is ZZ production, $e^+e^- \to ZZ \to \mu^+\mu^-\nu_i\bar{\nu}_i$ where ν_i denotes a neutrino of all three flavors. The W^+W^- background is larger than the ZZ background by a factor of about 20. In the following

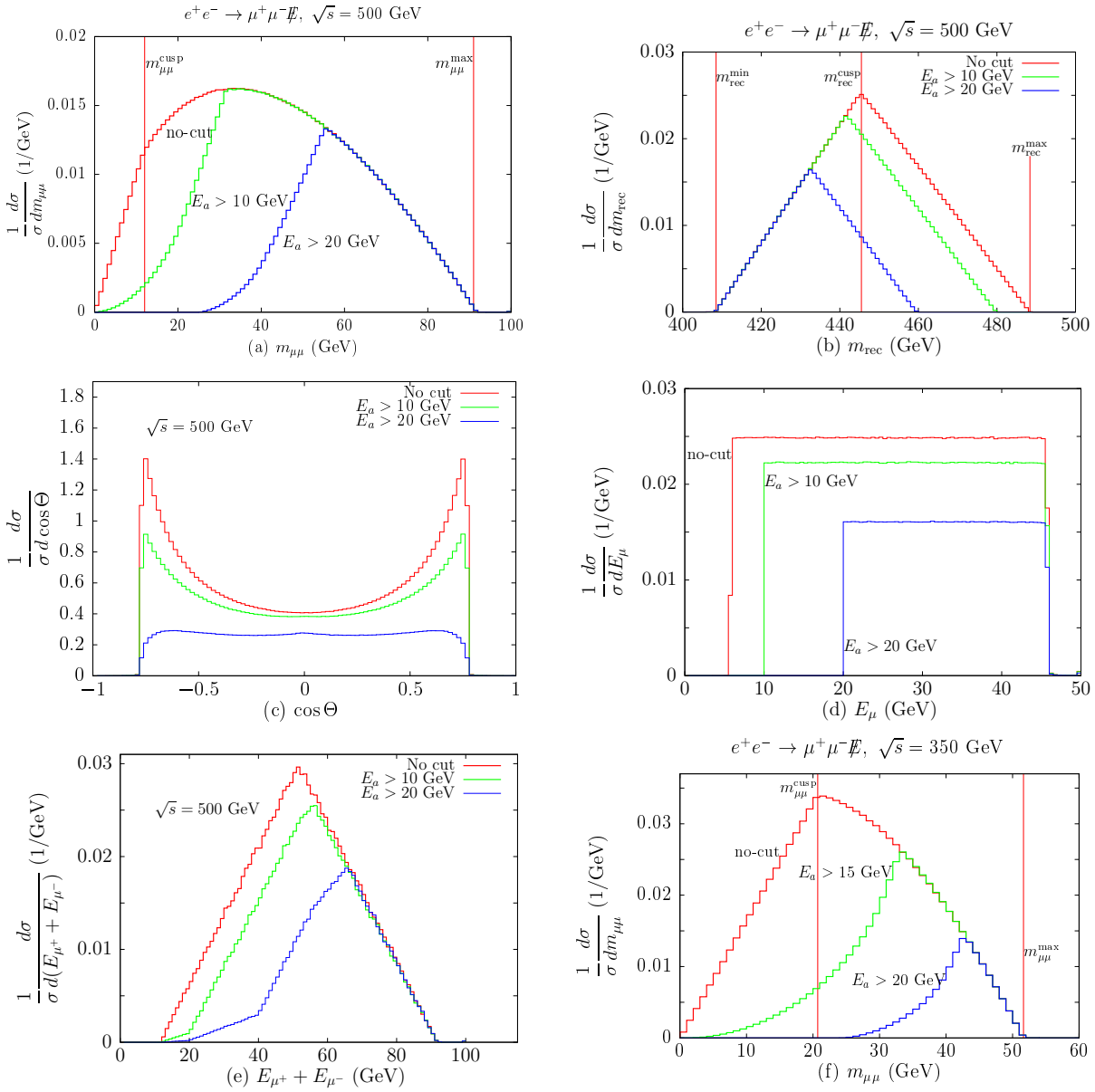

Figure 23: `Case-A` for $e^+e^- \to \tilde{\mu}_R\tilde{\mu}_R \to \mu^+\mu^-\not{E}$. Effects due to various E_a cuts on the (a) $m_{\mu\mu}$, (b) $m_{\rm rec}$, (c) $\cos\Theta$, (d) E_μ, and (e) $E_{\mu^+} + E_{\mu^-}$ distributions without spin-correlation and other realistic effects at $\sqrt{s} = 500\,\text{GeV}$. Each distribution is normalized by the total cross section without any other acceptance cut. Panel (f) for the $m_{\mu\mu}$ distribution is set to 350 GeV for comparison.

numerical simulation, we include the full SM processes for the final state $\mu^+\mu^-\nu\bar{\nu}$.

Another substantial SM background is from $e^+e^- \to e^+e^-\mu^+\mu^-$ where the outgoing e^+ and e^- go down the beam pipe and are missed by the detectors. It is mainly generated by Bhabha scattering with the incoming electron and positron through a t-channel diagram. This background could be a few orders of magnitude larger than the signal. However, a cut on the missing transverse momentum can effectively remove it. The maximum missing transverse momentum in this background comes from the final electron and positron, each of which retains the full energy ($\sqrt{s}/2$ each) and moves within an angle of 1° with respect to the beam pipe (at the edge of the end-cap detector coverage). As a result, most of these background events lie within

$$(\not{p}_T)_{\text{beam line } e^+e^-} \lesssim 3 \times 250\,\text{GeV} \times \sin(1^\circ) \simeq 15\,\text{GeV}. \tag{4.7}$$

We thus design our basic acceptance cuts for the event selection

$$\begin{aligned} \texttt{Basic cuts:} \qquad & E_a \geq 10\,\text{GeV}, \quad \not{p}_T \geq 15\,\text{GeV}, \\ & |\cos\theta_\ell^{\text{cm}}| \leq 0.9962, \quad m_{aa} \geq 1\,\text{GeV}, \quad m_{\text{rec}} \geq 1\,\text{GeV}. \end{aligned} \tag{4.8}$$

The angular cut on θ_ℓ^{cm} requires that the observed lepton lies within 5° from the beam pipe. This angular acceptance and the invariant mass cut on the lepton pair regularize the perturbative singularities. We also find that the $\not{p}_T$ cut removes the background from $e^+e^- \to e^+e^-\tau^+\tau^-$ [109].

In principal, the full SUSY backgrounds should be included in addition to the $\tilde{\mu}_R$ and $\tilde{\mu}_L$ signal pair production. There are many types of SUSY backgrounds. The dominant ones are the production of $\tilde{\chi}_1^0\tilde{\chi}_{j\geq 2}^0$ followed by the heavier neutralino decay of $\tilde{\chi}_{j\geq 2}^0 \to \ell^+\ell^-\tilde{\chi}_1^0$. However, their contributions are negligible with our mass point and event selection.

At the ILC environment, it is crucial to consider the other realistic factors in order to reliably estimate the accuracy for the mass determination. These include the effects of ISR, beamstrahlung [110] and detector resolutions. For these purposes, we adopt the ILC-Whizard setup [111], which accommodates the SGV-3.0 fast detector simulation suitable for the ILC [116].

4.2.3.2 `Case-A`: $\tilde{\mu}_R\tilde{\mu}_R$ pair production For the mass spectrum in `Case-A`, Fig. 24 presents a full simulation of the five kinematic distributions at $\sqrt{s} = 500\,\text{GeV}$ with the basic cuts in Eq. (4.8). The solid (red) line denotes our signal of the resonant production of a $\tilde{\mu}_R\tilde{\mu}_R$ pair. The dashed (blue) line is the total distribution including our signal and the SM backgrounds.

The $m_{\mu\mu}$ distribution from our signal in Fig. 24(a) does not reveal the best feature of the antler process. Its cusp is not very pronounced and its maximum is submerged under the dominant Z pole. As discussed before, this is because the c.m. energy of 500 GeV is too high compared with the smuon mass. On the contrary, the $m_{\rm rec}$ distribution in Fig. 24(b) separates our signal from the SM backgrounds well. A sharp triangular shape is clearly seen above the SM background tail. This separation is attributed to the weak scale mass of the missing particle X. If X were much lighter such as $M_X \simeq 10\,\text{GeV}$, the cusp position in the $m_{\rm rec}$ distribution of the signal would be shifted to a lower value and thus overlap with that of the large W^+W^- background.

Figure 24(c) presents the $\cos\Theta$ distributions with the W^+W^- background and the $\tilde{\mu}_R\tilde{\mu}_R$ signal. However, the highest point of $\cos\Theta$ (the cusp location) is shifted from the location of the $|\cos\Theta|_{\rm max}$ in Table 18, by about $2 \sim 3\%$. This is from the kinematical smearing due to ISR and beamstruhlung effects.

Figure 24(d) shows the muon energy distribution, which consists of two previously box-shaped distributions. Our signal distribution, which is expected to be flat for a scalar boson, is distorted by ISR. The SM background, mainly the W^+W^- background, shows a more tilted distribution, which has additional effects from spin correlation. The reason for the tilted distribution toward higher E_μ is that the W^+W^- production has the largest contribution from the production of $W_L^-W_R^+$ mediated by a t-channel neutrino [113]. Here W_L^- (W_R^+) denotes the left-handed (right-handed) negatively (positively) charged W boson. W_L^- has the left-handed coupling of ℓ_L^--$\bar{\nu}_R$-W_L^- so that the decayed ℓ_L^- moves along the parent W^- direction and the $\bar{\nu}$ in the opposite direction. The ℓ^- tends to have higher energy. Even though the E_μ distribution is not flat both for the signal and the backgrounds, their maximum positions are the same as predicted in Table 18. However, the minimum position for the W^+W^- distribution is below the acceptance cut while the minimum for the $\tilde{\mu}_R\tilde{\mu}_R$

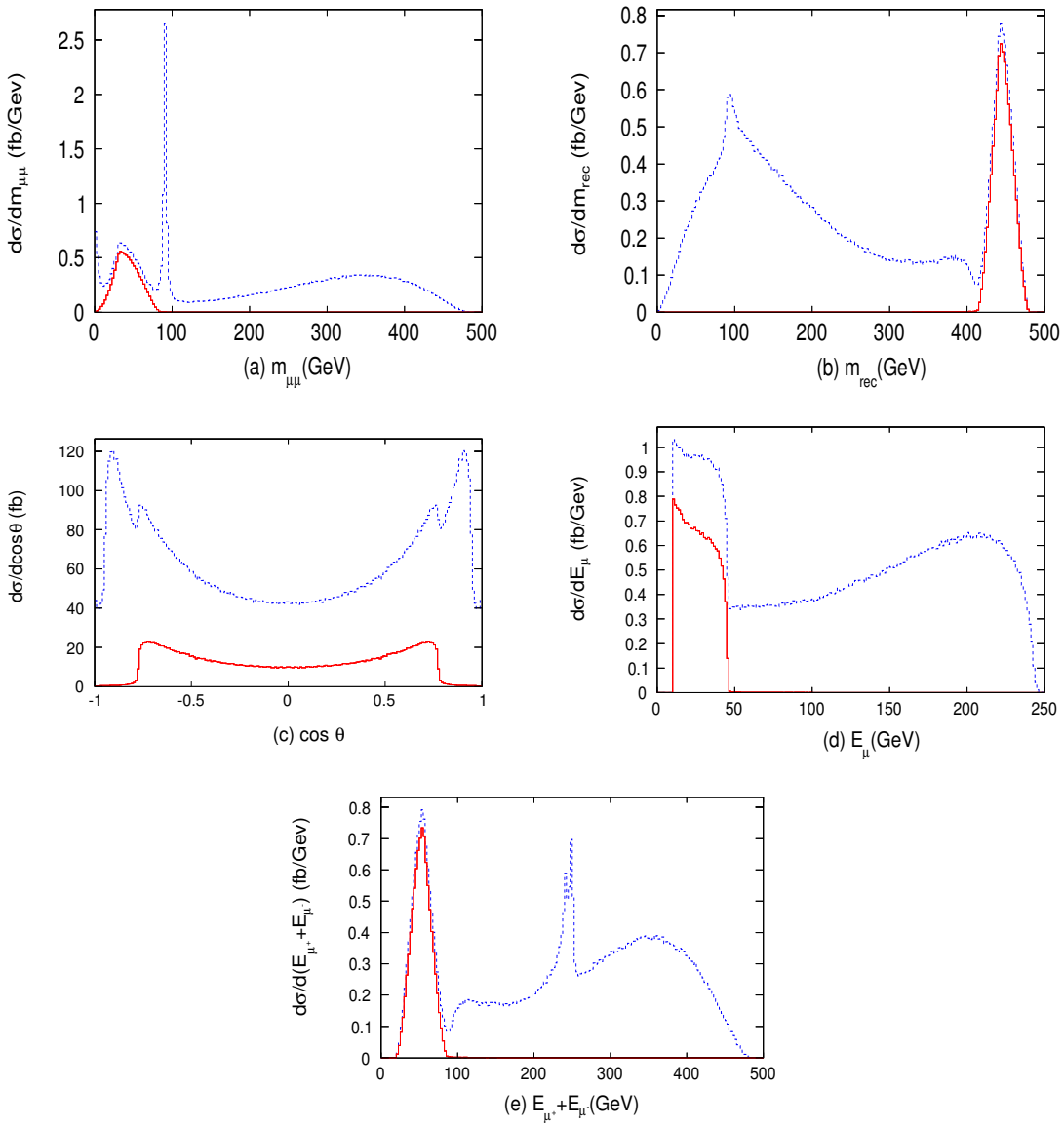

Figure 24: `Case-A` for $e^+e^- \to \tilde{\mu}_R\tilde{\mu}_R \to \mu^+\mu^-\not{E}$. Basic acceptance cut on the (a) $m_{\mu\mu}$, (b) $m_{\rm rec}$, (c) $\cos\Theta$, (d) E_μ, and (e) $E_{\mu^+} + E_{\mu^-}$ distributions with spin-correlation and other realistic effects. The c.m. energy is set to $\sqrt{s} = 500\,\text{GeV}$ for all distributions. The solid (red) line denotes our signal of the resonant production of a $\tilde{\mu}_R$ pair. The dashed (blue) line is the total event including our signal and the SM backgrounds.

signal is approximately the same as the cut. The measurement of these minima becomes problematic. As a result, the other kinematic observables discussed here are essential in the measurement of these masses.

Finally Figs. 24(e) presents the energy sum of two visible particles. The distribution for our signal is triangular and separated from the SM backgrounds. Even in the full and realistic simulation, the cusps and endpoints of the signal are very visible. In fact, the signal part of the distribution takes a very similar form to that of $m_{\rm rec}$.

Understanding those kinematic distributions of our signal is of great use to suppress the SM background. For example, we apply an additional cut of

$$m_{\rm rec} > 350\,{\rm GeV}, \tag{4.9}$$

and present the distributions of the same five kinematic variables in Fig. 25. Our signal, denoted by the solid (red) lines, remains intact since $m_{\rm rec}^{\rm min} = 408\,{\rm GeV}$ for $\tilde{\mu}_R\tilde{\mu}_R$. On the other hand, a large portion of the SM background is excluded. The antler characteristics of our signal emerge in the total distributions. We can identify all of the cusp structures.

4.2.3.3 `Case-B`: production of $\tilde{\mu}_R\tilde{\mu}_R$ and $\tilde{\mu}_L\tilde{\mu}_L$ We now consider the more complex `Case-B`, where three different antler processes ($\tilde{\mu}_R\tilde{\mu}_R$, $\tilde{\mu}_L\tilde{\mu}_L$, and W^+W^-) are simultaneously involved. In Fig. 26, we present five distributions for `Case-B` at $\sqrt{s} = 500\,{\rm GeV}$. Here, the $m_{\rm rec} > 350\,{\rm GeV}$ cut has been applied to suppress the main SM backgrounds from W^+W^-. The solid (red) line is the $\tilde{\mu}_R\tilde{\mu}_R$ signal, the dotted (purple) line is from $\tilde{\mu}_L\tilde{\mu}_L$. Finally, the dashed (blue) line is the total differential cross section including our two signals and the SM backgrounds. Note that the total rate for $\tilde{\mu}_R\tilde{\mu}_R$ is compatible with that for $\tilde{\mu}_L\tilde{\mu}_L$.

In Fig. 26(a), we show the $m_{\mu\mu}$ distributions. As expected from the previous analyses, the $\tilde{\mu}_R\tilde{\mu}_R$ signal leads to a cusp structure, while $\tilde{\mu}_L\tilde{\mu}_L$ and W^+W^- do not due to the specific mass and energy relations. On the contrary, the $m_{\rm rec}$ distribution for $\tilde{\mu}_R\tilde{\mu}_R$ denoted by the solid (red) curve and that for $\tilde{\mu}_L\tilde{\mu}_L$ by the dotted (purple) curve do show a triangle: see Fig. 26(b). The SM background is well under-control after the stringent cuts. The challenge is to extract the hidden mass information from the observed overall (dashed blue) curve as a combination of the twin peaks. It is conceivable to achieve this by a fitting procedure

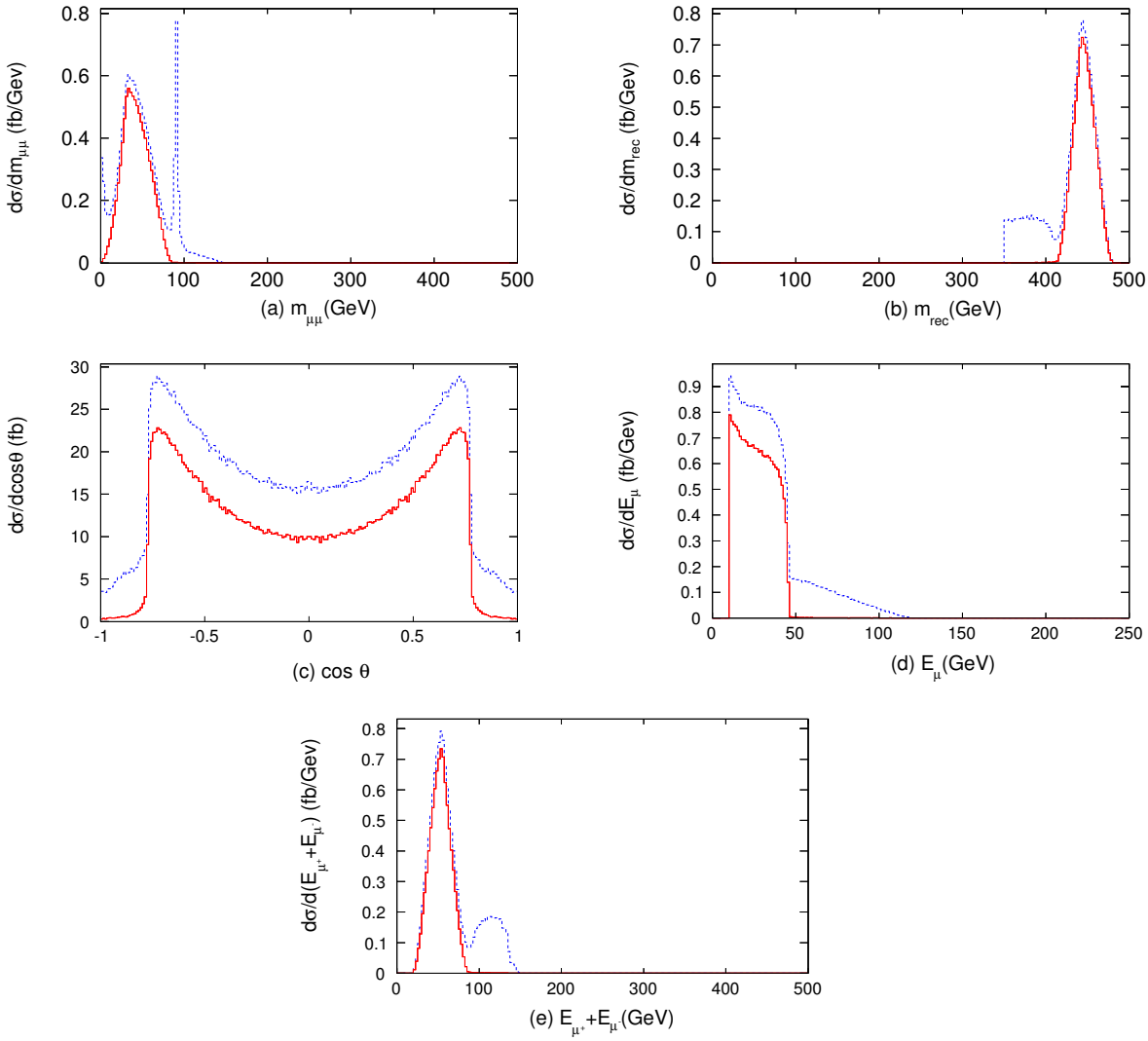

Figure 25: `Case-A` for $e^+e^- \to \tilde{\mu}_R\tilde{\mu}_R \to \mu^+\mu^-\not{E}$. The effect of an additional cut of $m_{\rm rec} > 350\,{\rm GeV}$ on the (a) $m_{\mu\mu}$, (b) $m_{\rm rec}$, (c) $\cos\Theta$, (d) E_μ, and (e) $E_{\mu^+} + E_{\mu^-}$ distributions with spin-correlation and other realistic effects. The c.m. energy is set to $\sqrt{s} = 500\,{\rm GeV}$ for all distributions. The solid (red) line denotes our signal of the resonant production of a $\tilde{\mu}_R$ pair. The dashed (blue) line is the total differential cross section including our signal and the SM backgrounds.

based on two triangles. Instead, as done below, we demonstrate another approach by taking advantage of the polarization of the beams.

Figure 26(c) presents the $\cos\Theta$ distribution. The visible $\cos\Theta$ cusp is usually attributed to the lighter intermediate particles ($\tilde{\mu}_R$ in our case). A larger $|\cos\Theta|_{\rm max}$ comes from a smaller m_B with a given c.m. energy. We see that, with our parameter choice, $\tilde{\mu}_R\tilde{\mu}_R$ and $\tilde{\mu}_L\tilde{\mu}_L$ lead to a similar value of $|\cos\Theta|_{\rm max}$, which differ by about 5%.

The E_μ distribution, with the energy endpoint in Fig. 26(d), is known to be one of the most robust variables. Two box-shaped distributions are added to create a two-step stair. Although ISR and beamstrahlung smear the sharp edges, the observation of the two maxima should be quite feasible. On the other hand, the determination of $E_\mu^{\rm min}$ could be more challenging if the acceptance cut for the lepton lower energy threshold overwhelms $E_\mu^{\rm min}$ for $\tilde{\mu}_R\tilde{\mu}_R$, and makes it marginally visible for $\tilde{\mu}_L\tilde{\mu}_L$.

Finally, we present the energy sum distribution of two visible particles in Figs. 26(e). The individual distribution from $\tilde{\mu}_R\tilde{\mu}_R$ and $\tilde{\mu}_L\tilde{\mu}_L$ production leads to impressive sharp triangles, as those in Fig. 26(b). The challenge is, once again, to extract the two unknown masses from the observed summed distribution. We next discuss beam polarization as a way to accomplish this.

All of the distributions show that the two entangled new physics signals as well as the SM backgrounds limit the precise measurements of the cusps and endpoints. The polarization of the electron and positron beams can play a critical role in disentangling this information. The current baseline design of the ILC anticipates at least 80% (30%) polarization of the electron (positron) beam. By controlling the beam polarization, we can suppress the SM backgrounds and distinguish the two different signals. For the $\tilde{\mu}_R\tilde{\mu}_R$ signal, our optimal setup is $\mathcal{P}_{e^-} = +80\%$ and $\mathcal{P}_{e^+} = -30\%$, denoted by $e_R^- e_L^+$, while for the $\tilde{\mu}_L\tilde{\mu}_L$ signal we apply $\mathcal{P}_{e^-} = -80\%$ and $\mathcal{P}_{e^+} = +30\%$ denoted by $e_L^- e_R^+$.

Figure 27 shows how efficient the right-handed electron beam is at picking out the $\tilde{\mu}_R\tilde{\mu}_R$ signal. For the suppression of the SM backgrounds, we apply the cut of $m_{\rm rec} \geq 350\,{\rm GeV}$. As before, the solid (red) line corresponds to $\tilde{\mu}_R^+\tilde{\mu}_R^-$, the dotted (purple) line to $\tilde{\mu}_L^+\tilde{\mu}_L^-$. The dashed (blue) line is the total differential cross section including our signal and the SM backgrounds. The nearly right-handed electron beam suppresses the SM background as

well as the $\tilde{\mu}_L\tilde{\mu}_L$ signal. Only the $\tilde{\mu}_R\tilde{\mu}_R$ signal stands out. The main SM background is through the resonant W^+W^- production. The left-handed coupling of e-ν_e-W is suppressed by the right-handed electron beam. Another interesting feature is that the Z-pole in the $m_{\mu\mu}$ distribution is also very suppressed. A significant contribution to the Z-pole is from $e^+e^- \to \nu_e\bar{\nu}_e Z$ process where Z is via WW fusion. Again the left-handed coupling of the charged current is suppressed by the right-handed electron beam.

The advantage of the cusp is clearly shown here. Its peak structure is not affected. However, the endpoints $m_{\rm rec}^{\rm min}$, $E_\mu^{\rm min}$, and $E_{\mu\mu}^{\rm max}$ do overlap with the backgrounds, although the right-handed polarization removes a large portion of the SM backgrounds. We also observe that $m_{\rm rec}^{\rm max}$, $E_\mu^{\rm max}$, and $E_{\mu\mu}^{\rm min}$ are not contaminated. In summary, the mass measurement of $\tilde{\mu}_R$ and $\tilde{\chi}_1^0$ through the cusps and endpoints is well benefitted by the right-handed polarization of the electron beam.

The left-handed $\tilde{\mu}_L\tilde{\mu}_L$ signal is more difficult to probe since its left-handed coupling is the same as the SM background. In Fig. 28, we set $\mathcal{P}_{e^-} = -80\%$ and $\mathcal{P}_{e^+} = +30\%$ with the additional cut of $m_{\rm rec} > 350\,{\rm GeV}$. From the $m_{\mu\mu}$ distribution, we see that the Z-pole is still strongly visible and the round $m_{\mu\mu}^{\rm cusp}$ for the $\tilde{\mu}_L\tilde{\mu}_L$ signal is very difficult to identify. The total $m_{\rm rec}$ distribution in Fig. 28(b) does not show the sharp triangular shape of the antler decay topology either. The individual triangular shapes of the $\tilde{\mu}_R\tilde{\mu}_R$ and $\tilde{\mu}_L\tilde{\mu}_L$ signals along with the SM background are combined into a rather featureless bump-shaped distribution. Although there is a peak point, it is hard to claim as a cusp. The $\cos\Theta$ distribution in Fig. 28(c) shows one of the most characteristic features of the antler topology. Two sharp cusps appear, which correspond to the $\tilde{\mu}_L\tilde{\mu}_L$ signal.

The total E_μ distribution in Fig. 28(d) does not provide quite a clean series of rectangular distributions. The mixture of different contributions from $\tilde{\mu}_R\tilde{\mu}_R$, $\tilde{\mu}_L\tilde{\mu}_L$ and W^+W^- along with the smearing makes reading the maximum points more difficult. The $E_\mu^{\rm min}$ position of the $\tilde{\mu}_L\tilde{\mu}_L$ signal, which is near the kinematic cut, is mixed with the SM backgrounds and the $\tilde{\mu}_R\tilde{\mu}_R$ signal. Finally, the total $E_{\mu\mu}$ distribution loses the triangular shape of the $\tilde{\mu}_L\tilde{\mu}_L$ signal: see Fig. 28(e). Nevertheless the peak position coincides with the cusp position for both energy sum distributions. We can identify them with the cusps.

4.2.4 The mass measurement precision

In order to estimate the achievable precision of a measurement of the masses in the presence of realistic effects, we analyze the distributions we have discussed here using the log-likelihood method based on Poisson statistics. A benefit of a log-likelihood analysis is that it compares the full shape of the distribution, not just the position of the cusps and endpoints which, as we have seen, can be smeared and even moved due to realistic collider effects. For our log-likelihood calculation, since we have shown that the background can be almost totally removed by appropriate cuts, we focus on comparing one signal to another with different masses for the smuon and neutralino.

We calculate the log-likelihood as

$$LL(N;\nu) = 2\sum_i \left[N_i \ln\left(\frac{N_i}{\nu_i}\right) + \nu_i - N_i \right] \tag{4.10}$$

where ν_i is the expected number of events in bin i with the masses set according to `Case-A` and N_i is the number of events expected in bin i for the alternate mass point. For each distribution, we use 50 bins. We take the integrated luminosity to be 100 fb^{-1} and find that the number of signal events is sufficiently large that the probability distribution of the log-likelihood approximates well a χ^2 distribution. We then find that the 95% confidence level value for each log-likelihood is $LL_{95\%} = 67.5$. We scan over the masses of the smuons and neutralinos in steps of 0.25 GeV, calculate the log-likelihood for each mass point, and plot the contour where it is equal to 67.5 in Fig. 29 for four kinematical variables assuming `Case-A`. These are the 95% confidence lines for each kinematical variable considered separately.

Considering the kinematics variables of $m_{\mu\mu}$ (red), m_{rec} (blue), $\cos\Theta$ (green), and E_μ (purple), we present the 95% C.L. allied contours in the parameter space of $(\Delta m_{\tilde{\chi}_1^0}, \Delta m_{\tilde{\mu}_R})$ in Fig. 29. All the variables are roughly equally good at measuring the two masses, leading to an accuracy of approximately ± 0.5 GeV (for clarity of the presentation, we have left out the contours for $E_{\mu\mu}$ and $E_{\rm rec}$).

We also find that our kinematical variables are very sensitive if we vary one mass parameter with the other fixed. However, the determination for the two masses is correlated, as seen from Fig. 29 with a linear band rather than a closed ellipse in the plotted region.

This is due to the fact that the cusps and endpoints depend on the masses mainly as a ratio rather than independently, as can be seen in Eqs. (B.4), (B.7), and (B.9). The ellipse shape of the contour will become manifest when extending to larger regions.

We have also considered the effect of combining these measurements in a joint test-statistic including a calculation of the correlation between these variables. The magnitude of the correlation is quantified by the ratio of the off-diagonal term to the diagonal term of the covariance matrix. We found that the correlation among $m_{\rm rec}$, E_μ and $\cos\Theta$ was negligible (the off-diagonal terms of the covariance matrix was a few percent or smaller compared to the diagonal terms), the correlation between $m_{\rm rec}$ and $E_{\mu\mu}$ was small but non-negligible (the off-diagonal term was approximately 8% of the diagonal terms), and $E_{\mu\mu}$ and $E_{\rm rec}$ were fully correlated as expected (the off-diagonal term was the same size as the diagonal term). However, we did not find appreciable improvement in the precision of the mass measurements by combining the log-likelihoods. This is due partly to the correlation between these variables, partly to the differences in how the log-likelihood depends on each of these variables, and partly to the properties of the χ^2 distribution when test statistics with a large number of degrees of freedom are combined as we briefly explain in Appendix C.

4.3 MASSIVE VISIBLE PARTICLE CASE: CHARGINO PAIR PRODUCTION

It is quite likely that the DM particles will be accompanied by other massive observable final states in the decay process. Although the nature of the cusps is similar to the previous discussions, the characteristic features and their observability may be different. An important example of this type of kinematics is in chargino pair production followed by the chargino's decay into a W and a $\tilde{\chi}_1^0$. This process is a typical antler process, which is different from the smuon pair production in that the visible particle W is massive. In order to fully reconstruct the kinematics of the W, we consider the case where the W boson decays hadronically. Our

signal event selection is

$$e^+e^- \to \tilde{\chi}_1^+\tilde{\chi}_1^- \to W^+W^-\tilde{\chi}_1^0\tilde{\chi}_1^0 \to jj, jj + \tilde{\chi}_1^0\tilde{\chi}_1^0. \tag{4.11}$$

For illustrative purposes, we consider the `Case-C` in Table 17.

For the LHC searches of gaugino production, there is no sensitivity with the current data yet [107] for the parameter choices under consideration, due to the disfavored kinematics of the small mass difference and the large SM backgrounds. The upcoming Run II at 13 TeV will likely reach the sensitivity to cover this parameter region [108]. It is thus exciting to look forward to the LHC outcome. Should a SUSY signal be observed at the LHC, it would strongly motivate the ILC experiment to further study the SUSY property and to determine the missing particle mass as proposed in this work.

The distributions of the invariant mass of W^+W^- and $\tilde{\chi}_1^0\tilde{\chi}_1^0$ follow the same characteristic function where now the visible particle W is massive. The cusp and endpoint positions of these distributions can be obtained from Table 20. The $\cos\Theta$ distribution for the massive visible particle case does not present a sharp cusp or endpoint. The E_W distribution has a minimum and a maximum as in the massless visible particle case. The distribution of $E_{WW} = E_{W^+} + E_{W^-}$ also accommodates the maximum, cusp and minimum. In Table 19, we present the values of the cusps and endpoints for `Case-C`.

The reconstruction of the variables m_{WW}, $m_{\rm rec}$, and E_{WW} is straightforward in terms of the jets and the known collision frame. In order to reconstruct E_W and $\cos\Theta$, we split the jets into two pairs and require each pair to reconstruct an invariant mass near m_W. We then note that due to the symmetry of the antler decay topology, the E_{W^+} and E_{W^-} distributions are equal to each other and the $\cos\Theta$ distribution is symmetric with respect to an interchange of W^+ and W^-. As a result, the E_W and $\cos\Theta$ distributions can be obtained by averaging the distributions for each W.

In addition to our basic cuts outlined in Eq. (4.8), we have applied the following cuts

$$\begin{aligned} \Delta R_{jj} \equiv \sqrt{(\Delta\eta_{jj})^2 + (\Delta\phi_{jj})^2} \geq 0.4 \ , \\ |m_{jj} - m_W| < 5\Gamma_W \ , \quad m_{\rm rec} > 120\,{\rm GeV} \ , \end{aligned} \tag{4.12}$$

where the jet separation ΔR_{jj} is between all pairs of jets, m_{jj} is only between pairs of jets identified with the W, and the $m_{\rm rec} > 120\,{\rm GeV}$ cut removes most of the remaining SM background. Again, we adopt the standard simulation packages ILC-Whizard setup [111], including the SGV-3.0 fast detector simulation suitable for the ILC [116].

In Fig. 30, the solid (red) lines denote our chargino signal. The dotted (blue) lines give the total differential cross section including our signal and the SM backgrounds. The SM backgrounds are computed through the full two-to-six processes $e^+e^- \to jjjj\nu\bar{\nu}$ which includes the full spin correlation.

Figures 30(a) and (b) show the invariant mass distributions of four jets and two invisible particles, respectively. Realistic effects smear the sharp m_{jjjj} and $m_{\rm rec}$ distributions significantly. In particular, the locations of $m_{jjjj}^{\rm min}$ and $m_{\rm rec}^{\rm min}$ are shifted to lower values by about 20 GeV from the expected values with kinematics alone in Table 19. This is mainly due to detector smearing. The $m_{jjjj}^{\rm cusp}$ and $m_{jjjj}^{\rm max}$ are respectively in agreement with the $m_{WW}^{\rm cusp}$ and $m_{WW}^{\rm max}$ values in Table 19 but are significantly smeared. The $m_{\rm rec}^{\rm cusp}$ and $m_{\rm rec}^{\rm max}$ are larger by about 10 GeV than the expected values. As commented earlier, the $\cos\Theta$ distribution in Fig. 30(c) does not have a sharp cusp even before including realistic effects.

Figure 30(d) presents the E_{jj} distribution which is significantly smeared and the sharp edges are no longer visible due to jet energy resolution effects. The expected values of $E_W^{\rm min}$ and $E_W^{\rm max}$ cannot be read from this distribution. In Fig. 30(e), we show the distribution of E_{jjjj}. The expected triangular shapes can be seen but the sharp features are smeared due to the realistic considerations. Their minimum and maximum positions are moved to approximately 10 GeV lower and higher values, respectively, while the cusp position identified with the peaks remains near the expected values.

We perform a log-likelihood analysis for the massive visible particle case and present the 95% C.L. contours for the mass measurement of $\tilde{\chi}_1^0$ and $\tilde{\chi}_1^\pm$ in Fig. 31. Remarkable is that $m_{\rm rec}$ leads to the most precise mass measurement, not the commonly considered variable E_W, especially on the missing particle mass. The E_W measurement leads to about $\Delta m_{\tilde{\chi}_1^0} \simeq \pm 4$ GeV precision while the $m_{\rm rec}$ improves into ± 2 GeV. This is due to the fact that the cusp peak position is more stable with respect to detector smearing effects, compared with the sharp energy endpoint. The intermediate chargino mass precision is about 2 GeV

both by E_W and $m_{\rm rec}$. The mass measurement precision is not as good as that of the smuon pair production, because of inferior hadronic four jet measurement here.

To appreciate the improvement for the missing mass measurement with our antler approach, we have compared it with the standard "mono-photon" signal, $e^+e^- \to \gamma \not{E}$ [103, 114]. Although this is the most model-independent method, the measurement of the endpoint in a slowly-varying E_γ spectrum results in rather poor sensitivity. Besides the potential model-dependence of the signal cross section, we find that the background $e^+e^- \to \gamma\nu\bar{\nu}$ is about 100 times larger than the signal for the benchmark point of Ref. [114]. We have performed the log-likelihood analysis and find that the best accuracy for the lightest neutralino mass determination would be no better than about 50 GeV.

4.4 SUMMARY AND CONCLUSIONS

WIMP dark matter below or near the TeV scale remains a highly motivated option. To convincingly establish a WIMP DM candidate, it is ultimately important to reach consistency between direct searches and collider signals for the common parameters of mass, spin and coupling strength [115].

Through the processes of antler decay topology at a lepton collider, $e^+e^- \to B_1B_2 \to X_1a_1 + X_2a_2$, we studied a new method for measuring the missing particle mass (m_X) and the intermediate particle mass (m_B): the cusp method. With this special and yet common topology, we explored six kinematic experimentally accessible observables, m_{aa}, $m_{\rm rec} \equiv m_{XX}$, $\cos\Theta$, E_a, E_{aa} and $E_{\rm rec} \equiv E_{XX}$. Each of these distributions accommodates singular structures: a minimum, a cusp and a maximum. Their positions are determined by the kinematics only, *i.e.*, the masses of B, a, X and $\sqrt{s}$, providing a powerful method to measure the particle masses m_B and m_X. We presented the analytic expressions for their positions in terms of their masses in Appendix B. We chose to study the accuracy for the mass determination at a lepton collider with three benchmark scenarios in the framework of the MSSM, as listed in Table 17, and named `Case-A`, `Case-B`, and `Case-C`.

`Case-A` is the simplest illustration where only a right-handed smuon ($\tilde{\mu}_R$) pair is kine-

matically accessible. `Case-B` is slightly more complicated since both right-handed and left-handed ($\tilde{\mu}_L$) smuon pairs can be produced. We consider the clean leptonic final state of $\mu^+\mu^-\not{E}$ from the smuon decays. By presenting the signal kinematics, we first confirmed the analytic expressions numerically in Fig. 21. We showed that, except for m_{aa}, due to an anticipated kinematical reason, all the other variables yield the pronounced features of a cusp distribution. Although the SM background $e^+e^- \to W^+W^- \to \mu^+\nu_\mu\mu^-\bar{\nu}_\mu$ also results in the antler topology, the positions of the cusps are significantly different due to the massless missing particles, the neutrinos. This difference is used to separate the SM background very efficiently. Furthermore, we pointed out that the experimental acceptance cuts on the observable leptons may change the positions and the shapes of the cusps in a systematic and predictable way, as seen in Figs. 22 and 23.

Through a full simulation including spin correlation, the SM backgrounds, and other realistic effects, we studied how much of the idealistic features of the cusps and endpoints survive, and how well the cusp method determines the missing particle mass for a 500 GeV ILC. We found that the inevitable experimental effects of ISR, beamstrahlung and detector resolutions not only distort the characteristic distributions but also shift the cusp and endpoint positions, as seen in Figs. 24, 25 and 26. The beam polarization may be used to effectively separate the final state $\tilde{\mu}_R\tilde{\mu}_R$ and $\tilde{\mu}_L\tilde{\mu}_L$, as shown in Figs. 27 and 28. To optimize our statistical treatment, we exploited the log-likelihood method based on the Poisson probability function. The precisions for the mass measurement with various variables in `Case-A` were shown in Fig. 29. The accuracy could reach approximately ± 0.5 GeV for smuon pair production, and was comparable for the muon energy endpoint E_μ and the cusp in $m_{\rm rec}$, $E_{\mu\mu}$ or E_{XX}.

In `Case-C`, we studied the chargino pair production with $\tilde{\chi}_1^\pm \to W^\pm\tilde{\chi}_1^0$. We focused on the hadronic decay $W \to jj$ in order to effectively reconstruct the kinematics, and to explore the detector effects on the hadronic final state. The poor energy resolution for the hadronic final state of the W decay smears the cusp and endpoint quite significantly, as shown in Fig. 30. We found that the $m_{\rm rec}$, E_{jjjj} and $E_{\rm rec}$ cusps are more stable than the energy endpoint E_{jj} against realistic experimental effects, and thus provided a more robust mass determination reaching approximately ± 2 GeV. In the previous section, we also made a comparison with

the other proposed methods for determining the missing mass at a lepton collider. We see the merits of our approach.

Under the clean experimental environment and well-defined kinematics, a future high energy lepton collider may take advantage of the antler decay topology and provide an accurate determination for the missing particle mass consistent with the WIMP DM candidate.

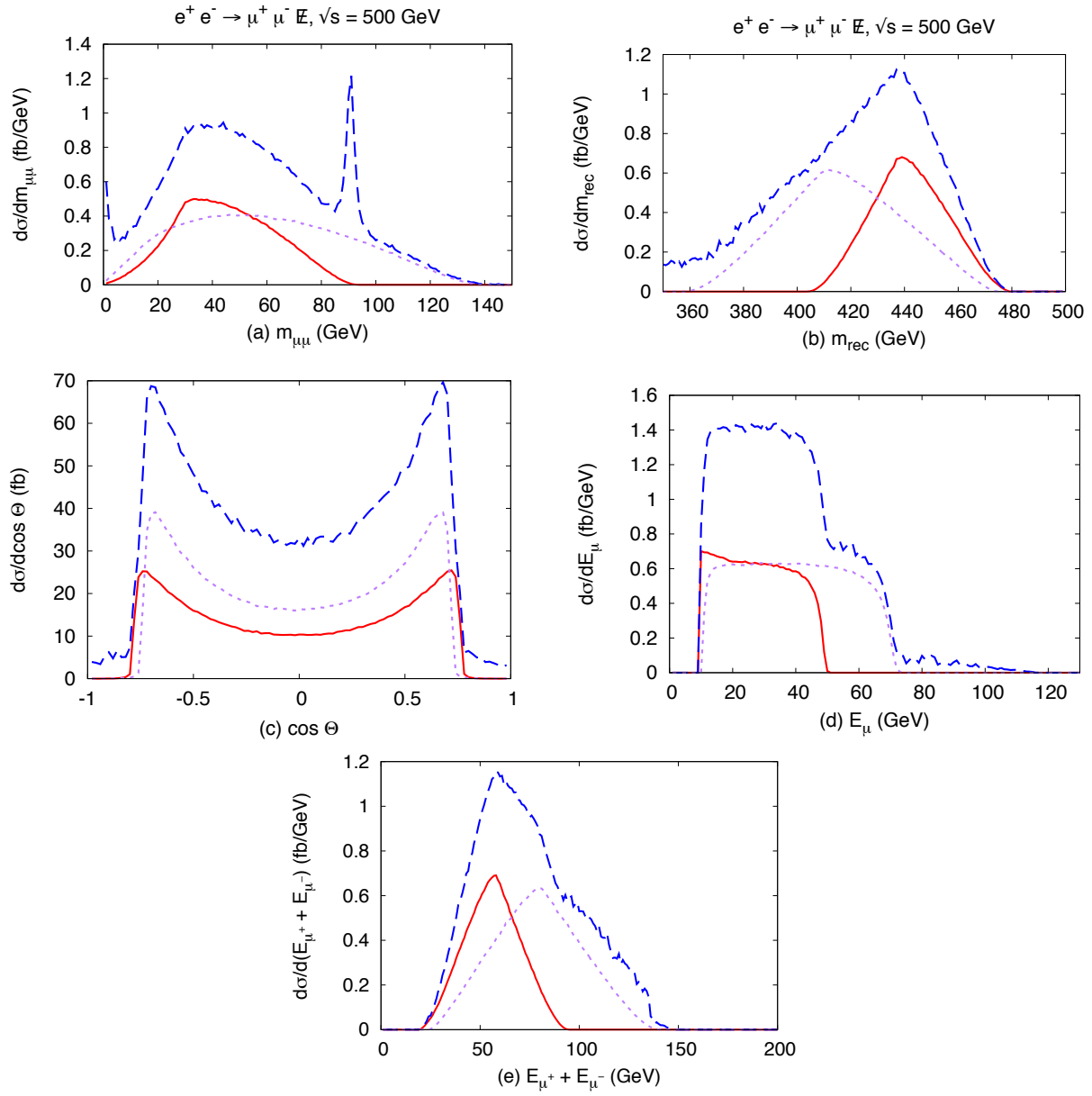

Figure 26: `Case-B` for $e^+e^- \to \tilde{\mu}_L\tilde{\mu}_L,\ \tilde{\mu}_R\tilde{\mu}_R \to \mu^+\mu^-\not{E}$. The additional cut of $m_{\rm rec} > 350\,\text{GeV}$ is included. We show the (a) $m_{\mu\mu}$, (b) $m_{\rm rec}$, (c) $\cos\Theta$, (d) E_μ, and (e) $E_{\mu^+} + E_{\mu^-}$ distributions with spin-correlation and other realistic effects. The c.m. energy is set $\sqrt{s} = 500\,\text{GeV}$ for all distributions. The solid (red) line corresponds to $\tilde{\mu}_R^+\tilde{\mu}_R^-$, the dotted (purple) line to $\tilde{\mu}_L^+\tilde{\mu}_L^-$. The dashed (blue) line is the total differential cross section including our signal and the SM backgrounds.

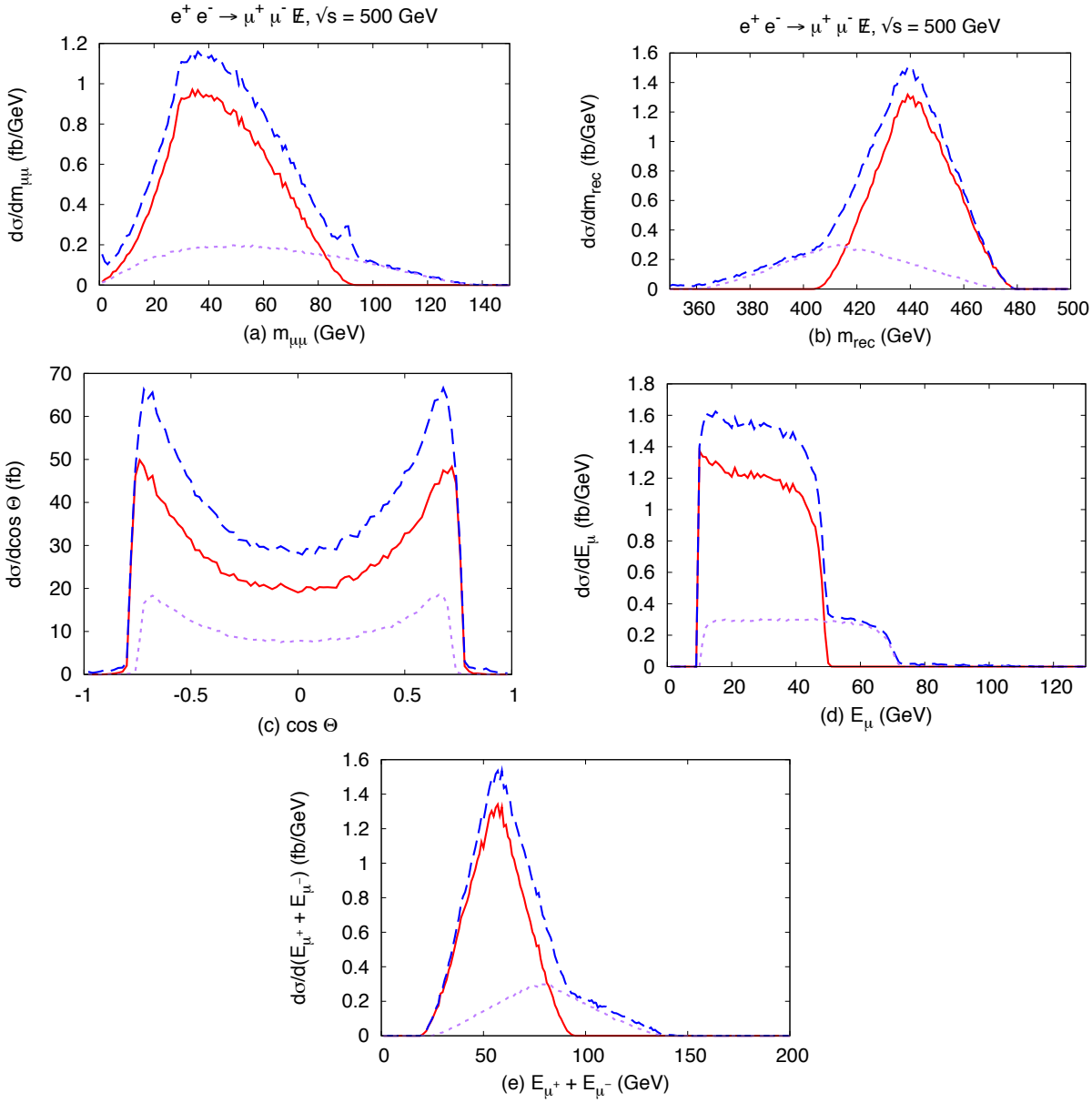

Figure 27: `Case-B` for $e^+e^- \to \tilde{\mu}_L\tilde{\mu}_L,\ \tilde{\mu}_R\tilde{\mu}_R \to \mu^+\mu^-\not{E}$. Effects of an additional cut of $m_{\rm rec} > 350\,\text{GeV}$ and polarizations $\mathcal{P}_{e^-} = +80\%$ and $\mathcal{P}_{e^+} = -30\%$ on the (a) $m_{\mu\mu}$, (b) $m_{\rm rec}$, (c) $\cos\Theta$, (d) E_μ, and (e) $E_{\mu^+} + E_{\mu^-}$ distributions with spin-correlation and other realistic effects. The c.m. energy is set to $\sqrt{s} = 500\,\text{GeV}$ for all distributions. The solid (red) line corresponds to $\tilde{\mu}_R^+\tilde{\mu}_R^-$, the dotted (purple) line to $\tilde{\mu}_L^+\tilde{\mu}_L^-$. The dashed (blue) line is the total differential cross section including our signal and the SM backgrounds.

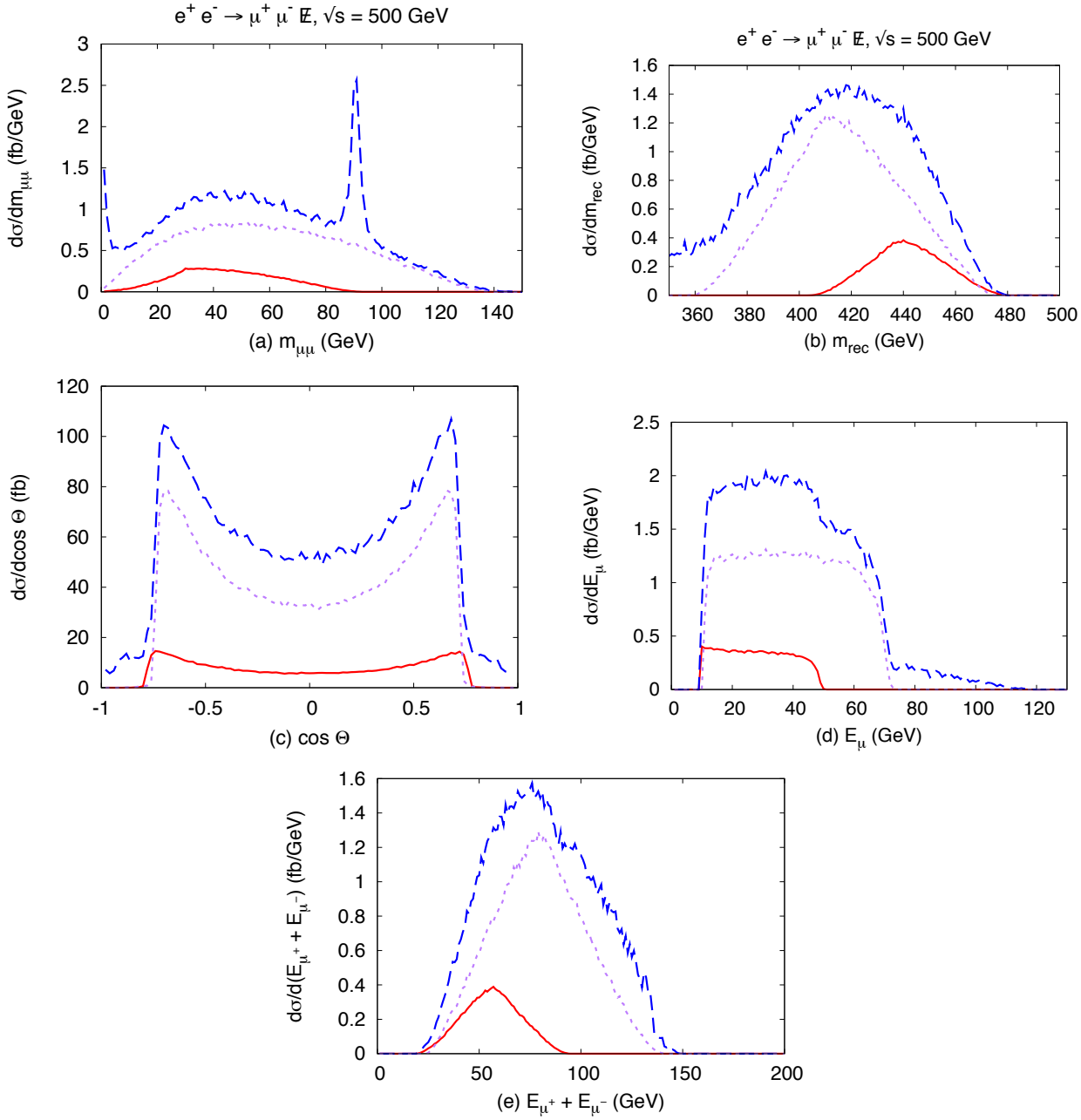

Figure 28: `Case-B` for $e^+e^- \to \tilde{\mu}_L\tilde{\mu}_L,\ \tilde{\mu}_R\tilde{\mu}_R \to \mu^+\mu^-\not{E}$. Effects of an additional cut of $m_{\rm rec} > 350\,\text{GeV}$ and polarizations $\mathcal{P}_{e^-} = -80\%$ and $\mathcal{P}_{e^+} = +30\%$ on the (a) $m_{\mu\mu}$, (b) $m_{\rm rec}$, (c) $\cos\Theta$, (d) E_μ, and (e) $E_{\mu^+} + E_{\mu^-}$ distributions with spin-correlation and other realistic effects. The c.m. energy is set to $\sqrt{s} = 500\,\text{GeV}$ for all distributions. The solid (red) line corresponds to $\tilde{\mu}_R^+\tilde{\mu}_R^-$, the dotted (purple) line to $\tilde{\mu}_L^+\tilde{\mu}_L^-$. The dashed (blue) line is the total event including our signal and the SM backgrounds.

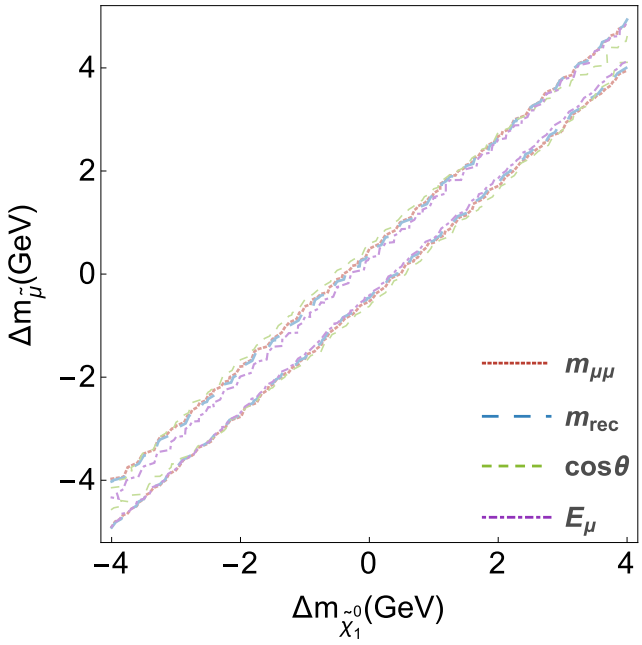

Figure 29: For `Case-A` for $e^+e^- \to \tilde{\mu}_R\tilde{\mu}_R \to \mu^+\mu^-\not{E}$, the 95% C.L. contours for the precision of the mass measurement in the parameter space of $(\Delta m_{\tilde{\chi}_1^0}, \Delta m_{\tilde{\mu}_R})$. An additional cut of $m_{\rm rec} > 350\,\text{GeV}$ on the distributions with spin-correlation and other realistic effects are included. The c.m. energy is set to $\sqrt{s} = 500\,\text{GeV}$ for all distributions and the integrated luminosity is $100\,\text{fb}^{-1}$.

$\sqrt{s}$	Channel	(m_B, m_X, m_a)	$(m_{WW}^{\rm min}, m_{WW}^{\rm cusp}, m_{WW}^{\rm max})$	$(m_{\rm rec}^{\rm min}, m_{\rm rec}^{\rm cusp}, m_{\rm rec}^{\rm max})$
500	$\tilde{\chi}_1^+\tilde{\chi}_1^-$	$(235, 139, m_W)$	$(161, 171, 221)$	$(279, 296, 338)$
		$(E_W^{\rm min}, E_W^{\rm max})$	$(E_{WW}^{\rm min}, E_{WW}^{\rm cusp}, E_{WW}^{\rm max})$	$(E_{XX}^{\rm min}, E_{XX}^{\rm cusp}, E_{XX}^{\rm max})$
		$(81, 111)$	$(162, 190, 221)$	$(278, 309, 338)$

Table 19: The values of various kinematic cusps and endpoints for the mass parameters in the `Case-C`. All the masses and energies are in units of GeV.

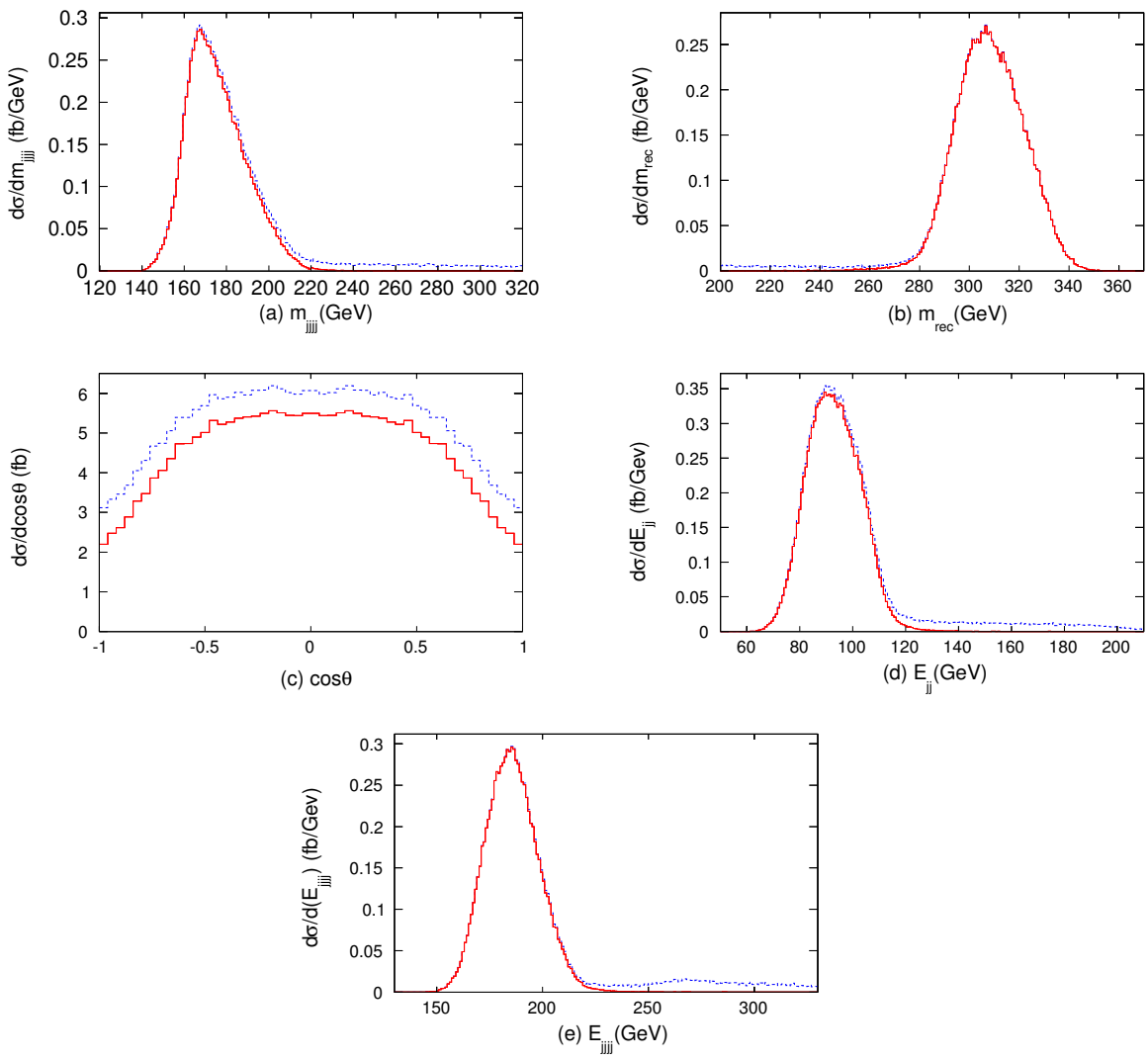

Figure 30: `Case-C` for $e^+e^- \to jj, jj + \not{E}$ with an additional cut of $m_{\rm rec} \geq 120\,\text{GeV}$ and $|m_{jj} - m_W| < 5\Gamma_W$. We show the (a) m_{jjjj}, (b) $m_{\rm rec}$, (c) $\cos\Theta$, (d) E_{jj}, and (e) E_{jjjj} distributions with spin-correlation and other realistic effects. The c.m. energy is set to $\sqrt{s} = 500\,\text{GeV}$ for all distributions. The solid (red) line denotes our signal of the resonant production of a chargino pair. The dashed (blue) line is the total differential cross section including our signal and the SM backgrounds.

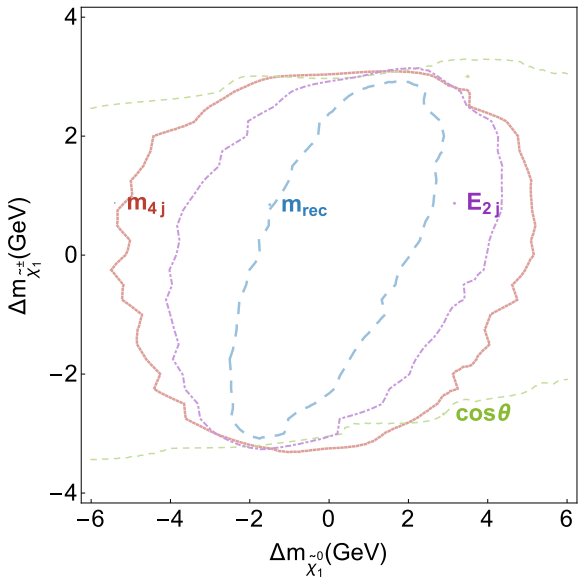

Figure 31: `Case-C` for $e^+e^- \to jj, jj + \not{E}$, the 95% C.L. contours for the precision of the mass measurement in the parameter space of $(\Delta m_{\tilde{\chi}_1^0}, \Delta m_{\tilde{\chi}_1^\pm})$. The additional cuts of $m_{\rm rec} \geq 120\,\text{GeV}$ and $|m_{jj} - m_W| < 5\Gamma_W$ are included in the distributions as well as spin-correlation and other realistic effects. The c.m. energy is set to $\sqrt{s} = 500\,\text{GeV}$ for all distributions and the integrated luminosity is $100\,\text{fb}^{-1}$.

5.0 CONCLUSIONS

After the Higgs boson discovery and initial measurements for the SM-like properties at the LHC Run I and Run II, it is imperative at the HL-LHC and future colliders to improve the precision and tackle the more challenging channels with Higgs production and the rare Higgs decays. In summary of this dissertation, I presented my study on the Higgs properties and measurements at current collider such as the LHC, and proposed future linear colliders. We proposed possible improvements to Higgs measurements both for its gauge and Yukawa couplings.

In Chapter 2, I presented our study on the HZZ coupling measurement through the ZZ-fusion process at a linear collider. It accomplishes a promising sensitivity for this gauge coupling in the Higgs sector. The total inclusive cross section can be measured to 2.5% at 1 TeV. Combined with the Higgsstrahlung channel at 250 GeV, the measurement of the cross section is further improved to 1.5%. This further helps constrain the Higgs total width measurement at colliders. The achieved sensitivity on HZZ coupling at 1 TeV also allows for distinguishing contributions from different higher-dimensional operators that have different energy dependences. Taken as an example two dimension-6 operators that are hardly constrained at the LHC, we showed that our study realizes as large as 50% relative improvement for the simultaneous constraints on these two operators, compared to the Zh-associated production channel alone.

In Chapter 3, being inspired to improve our understanding on the small Yukawa couplings of the Higgs sector, we proposed the challenging measurement of the Higgs decay to light jets at the LHC. The result is largely limited by the dominant systematic errors which we treat in detail with parametric fitting. The estimated sensitivity by the end of the HL-LHC run for the SM signal is 1σ. Accounting for the tagging efficiencies of different jet flavors,

combining with previous studies on $h \to b\bar{b},\ c\bar{c}$ channels, we are able to derive additional bounds from this di-jet decay measurement of the Higgs. The bounds correspond to 4 and 15 times the SM values for BR($h \to gg$) and BR($h \to c\bar{c}$), respectively, at 95% CL. Bounds on lighter Yukawa couplings can also be extracted and would provide independent constraints in a global fitting scheme. In optimizing our kinematics for the study, we proposed a "di-jet-vicinity" Higgs mass reconstruction method that improves the signal sensitivity and stays robust under simulated pile-up effects.

In Chapter 4, we investigated the missing mass determination possibilities at a linear collider. We tested a newly proposed cusp method on mass measurements for the antler processes. We studied several proposed kinematic variables that contain prominent cusps and end points structures in the distribution and did combined likelihood analysis. With the three benchmark scenarios we investigated, we indeed achieved comparable or better sensitivities compared to other methods. The accuracy reaches approximately ± 0.5 GeV for smuon pair production. In the case of chargino pair production with $\tilde{\chi}_1^{\pm} \to W^{\pm}\tilde{\chi}_1^0$ and $W \to jj$, we found that our cusps are more stable than the energy endpoints against realistic experimental effects, and thus provided a more robust mass determination reaching approximately ± 2 GeV sensitiviy on the chargino and neutralino masses.

In conclusion, the SM theory and current observations of the Higgs so far are consistent, but there is considerable room and motivation for new physics to appear as deviations in the Higgs sector. In many new theoretical scenarios such deviations would arise at a potentially detectable level either at LHC or possible future lepton colliders. Measurement of the Higgs couplings is thus a key tool in establishing departures from the SM, and in characterizing and distinguishing different new physics scenarios. Additionally, direct tackle of mass measurement and coupling determination for generic processes at colliders guide us in new physics collider searches.

For detection, both the current running hadron collider LHC, and lepton colliders have their advantages and disadvantages. Generally, the LHC or HL-LHC is our energy frontier in the foreseeable future, and it is an optimal machine to produce and give hints on new resonances. At the same time, it continues to improve our existing Higgs measurement. On the other hand at a lepton collider, with well-defined initial state and relatively clean

QCD background, higher precision measurement for rare Higgs processes will be possible, and precision measurement for more generic new physics processes can be carried out once above the production threshold.

Our study considered rare production and decay processes of the Higgs boson, and improved the Higgs coupling measurements with current and future colliders. With these improvements, the results can be interpreted as constraints on parameter space on specific model types. Model independently, we extrapolate the improved measurements on Higgs gauge coupling to constraints on wilson coefficients of gauge invariant dimension-6 operators.

The discovery and confirmation of the standard model have been a triumphant result of the close cooperation and parallel development between theory and experiments over the past few decades. The standard model has been a successful theory and it continues to be tested in collider experiments. At the same time it is challenged to accommodate and understand new phenomena ranging from neutrino masses, the inclusion of gravity, the history of the early universe, the symmetries or symmetry breaking that are present, and the existing astrophysical evidence of dark matter etc. To explore and to understand all these rich phenomena, the efforts will go on in our collider experiments to look for deviations from the current theory, in collecting evidences from astronomical observations, and in testing theories that may guide us towards the next revelation. Among the efforts, the Higgs sector of the theory, which solves the myth of the broken electroweak symmetry and pieces together the current standard model, will continue to be scrutinized and may provide us answers as to how the symmetry breaking happens in a larger picture.

APPENDIX A

CONSIDERATION OF ONE-PHOTON SENSITIVITY

As discussed in the main text, we find it useful to simply veto events with a single, isolated photon in addition to an electron-positron pair. This cut reduces the potentially large background arising from Bhabha scattering plus radiation which can pass the invariant mass and p_T cuts. This cut also reduces signal events where the Higgs decays to a single photon plus invisible particles, or a single photon plus additional particles which are lost down the beam pipe. In general we do not expect this to be a relevant effect since our final sensitivity for the model-independent cross section is 2.5% while the Standard Model processes which might contribute to such events are at the level of 10^{-3} branching fractions or less. Only order of magnitude enhancements to these channels from exotic physics would be relevant to our analysis and such enhancements are constrained by exclusive searches at the LHC and in future at the ILC.

Nevertheless, there may be some exotic model which would produce an observable effect in the inclusive measurement which is not ruled out by other searches. We note that if one wishes to preserve sensitivity to exotic channels which could produce a single isolated photon, it is possible to institute cuts which will remove almost all of the background while preserving a substantial fraction of any such Higgs decays. We find that, in the reconstructed Higgs rest frame, the isolated photon in the background sample is not isotropically distributed. The background photon usually appears collinear to the Higgs boost direction, and/or confined to be near the radial plane containing the beam and the Higgs boost vector. This is because the photon is recoiling against the e^-e^+ pair with a possible boost along the beam axis

due to additional unseen photons. We also find that measurement errors on the photon are typically larger in the polar angle than in the azimuthal direction. Thus one can largely remove this background by cutting on the polar (with respect to the Higgs boost) and azimuthal (measured with respect to the Higgs-beam plane) angles of a single extra photon in the Higgs rest frame. We find the problematic background can be reduced to the level of a few fb while preserving $\sim 60\%$ of any hypothetical Higgs decay signal, [1] since the photon from such a decay would be isotropically distributed in the Higgs rest frame. Hence any new physics signal large enough to affect the inclusive rate would still be observable, although underestimated.

We note that a cut similar in spirit to this one is already present in the widely used analysis of Higgsstrahlung-inclusive measurement at the 250 GeV ILC [50]. In that case additional single photons were removed by a "p_T balance" cut when the p_T of an isolated photon accounted for the bulk of the e^-e^+ pair p_T. However, since this more complicated approach does not materially change our results we present the simpler case of simply vetoing the single isolated photon as described in the main text.

[1] This fraction is relative to other decay channels not affected by the cut, since other cuts will affect all decays equally.

APPENDIX B

CUSPS AND ENDPOINTS OF THE ANTLER PROCESS

The kinematics is conveniently expressed by the rapidities η_j (equivalent to the speed $\beta = |\vec{p}|/E$), which specifies the four-momentum of a massive particle j from a two-body decay of $i \to j+k$ in the rest frame of the parent particle i as $p_j^{(i)} = m_j \left(\cosh\eta_j,\ \hat{p}_j^{(i)} \sinh\eta_j\right)$. Given two unknown masses in the process, the kinematics of Eq.(4.2) is determined by three rapidities of the intermediate particle B, the visible particle a, and the missing particle X, two of which are independent, given by

$$\cosh\eta_B = \frac{\sqrt{s}}{2m_B}, \quad \cosh\eta_a = \frac{m_B^2 - m_X^2 + m_a^2}{2m_a m_B}, \quad \cosh\eta_X = \frac{m_B^2 - m_a^2 + m_X^2}{2m_X m_B}. \tag{B.1}$$

Note that in the massless visible particle case ($m_a = 0$) the rapidity η_a goes to infinity. As discussed in general in reference [164], assuming a smooth square amplitude, kinematic singular points can arise in general when there are points with vanishing Jacobians when we project from the full phase space to certain observable spaces. The singular points show up as kinematic end points or cusps in the distribution, which serve as robust observables to measure unknown parameters in the kinematics.

In the case of antler topology, we find the distributions of the following six kinematic observables informative:

$$m_{aa}, \quad m_{\rm rec}, \quad \cos\Theta, \quad E_a, \quad E_{aa}, \quad E_{XX}. \tag{B.2}$$

(i) m_{aa} *distribution*: m_{aa} is the invariant mass of the two visible particles. This distribution accommodates three singular points: a minimum, a cusp, and a maximum. Their positions

	$\mathcal{R}_1: \ \eta_B < \frac{\eta_a}{2}$	$\mathcal{R}_2: \ \frac{\eta_a}{2} < \eta_B < \eta_a$	$\mathcal{R}_3: \ \eta_a < \eta_B$
$m_{aa}^{\min}$	$2m_a$		$2m_a \cosh(\eta_B - \eta_a)$
m_{aa}^{cusp}	$2m_a \cosh(\eta_B - \eta_a)$	$2m_a \cosh \eta_B$	
$m_{aa}^{\max}$	$2m_a \cosh(\eta_B + \eta_a)$		

Table 20: The cusp and endpoints of the invariant mass distribution m_{aa} in the three regions of c.m. energy and parameter space.

are not uniquely determined by the involved masses. They differ according to the relative scales of masses. There are three regions [96]

$$\mathcal{R}_1 : \eta_B < \frac{\eta_a}{2}, \quad \mathcal{R}_2 : \frac{\eta_a}{2} < \eta_B < \eta_a, \quad \mathcal{R}_3 : \eta_a < \eta_B. \tag{B.3}$$

The cusps and endpoints in the three regions are given in Table 20. The minimum endpoint is the same for $\mathcal{R}_1$ and $\mathcal{R}_2$ but different for $\mathcal{R}_3$. The cusp is the same for $\mathcal{R}_2$ and $\mathcal{R}_3$, which is different for $\mathcal{R}_1$. The maximum endpoints are the same for all three regions. The absence of *a priori* knowledge of the masses gives us ambiguity among $\mathcal{R}_1$, $\mathcal{R}_2$, and $\mathcal{R}_3$. For example we do not know whether the measured $m_{aa}^{\min}$ is $2m_a$ or $2m_a \cosh(\eta_B - \eta_a)$.

In the massless visible particle case, however, three singular positions are uniquely determined as

$$\begin{aligned} m_{aa}^{\min} &= 0\,, \\ m_{aa}^{\text{cusp}} &= m_B \left(1 - \frac{m_X^2}{m_B^2}\right) e^{-\eta_B}\,, \\ m_{aa}^{\max} &= m_B \left(1 - \frac{m_X^2}{m_B^2}\right) e^{\eta_B}\,. \end{aligned} \tag{B.4}$$

According to the analytic function for the m_{aa} distribution [95], the m_{aa} cusp is sharp only when the B pair production is near threshold, *i.e.*, when $0.443\sqrt{s} < m_B < 0.5\sqrt{s}$.

(*ii*) m_{rec} *distribution*: The invariant mass of two invisible particles, denoted by m_{rec}, can be measured through the relation

$$m_{\text{rec}}^2 \equiv m_{XX}^2 = s - 2\sqrt{s}\,(E_{a_1} + E_{a_2}) + m_{aa}^2. \tag{B.5}$$

The $m_{\rm rec}$ distribution is related to the invariant mass distribution of massive visible particles because of the symmetry of the antler decay topology. It also has three singular points, $m_{\rm rec}^{\rm min}$, $m_{\rm rec}^{\rm cusp}$, and $m_{\rm rec}^{\rm max}$. Their positions are as in Table 20, with replacement of $m_a \to m_X$ and $\eta_a \to \eta_X$.

(*iii*) E_a *distribution*: The energy distribution of one visible particle in the lab frame also provides important information about the masses. If the intermediate particle B is a scalar particle like a slepton, its decay is isotropic and thus produces a flat rectangular distribution. Two end points, $E_a^{\rm min}$ and $E_a^{\rm max}$, are determined by the masses:

$$E_a^{\rm max,min} = \frac{\sqrt{s}}{4}\left(1 - \frac{m_X^2 - m_a^2}{m_B^2}\right)\left(1 \pm \beta_B \sqrt{1 - \frac{4m_a^2 m_B^2}{(m_B^2 + m_a^2 - m_X^2)^2}}\right), \tag{B.6}$$

where β_B is defined by

$$\beta_B = \sqrt{1 - \frac{4m_B^2}{s}}. \tag{B.7}$$

Note that if $m_B \ll \sqrt{s}/2$ or $m_X \approx m_B$, then $E_a^{\rm min}$ can be very small, even below the experimental acceptance for observation.

(*iv*) E_{aa} *distribution*: The distribution of the combined energy of the $a_1 a_2$ system, $E_{aa} \equiv E_{a_1} + E_{a_2}$, is triangular, leading to three singular positions, $E_{aa}^{\rm min}$, $E_{aa}^{\rm cusp}$, and $E_{aa}^{\rm max}$, which are in terms of masses

$$\begin{aligned} E_{aa}^{\rm max,mix} &= 2m_a \cosh(\eta_a \pm \eta_B), \\ E_{aa}^{\rm cusp} &= 2m_a \cosh\eta_a \cosh\eta_B. \end{aligned} \tag{B.8}$$

For $m_a = 0$, we have simpler expressions as

$$\begin{aligned} E_{aa}^{\rm max,mix}\big|_{m_a=0} &= \frac{\sqrt{s}}{2}\left(1 - \frac{m_X^2}{m_B^2}\right)(1 \pm \beta_B), \\ E_{aa}^{\rm cusp}\big|_{m_a=0} &= \frac{\sqrt{s}}{2}\left(1 - \frac{m_X^2}{m_B^2}\right). \end{aligned} \tag{B.9}$$

(*v*) E_{XX} *distribution*: Although the energy of one invisible particle is not possible to measure, the sum of two invisible particle energies can be measured through

$$E_{XX} \equiv E_{X_1} + E_{X_2} = \sqrt{s} - E_{aa}. \tag{B.10}$$

The distribution of E_{XX} is a mirror image of the E_{aa} distribution, which is triangular with a sharp cusp.

(*vi*) $\cos\Theta$ *distribution*: Here Θ is the angle between the momentum direction of one visible particle (say a_1) in the c.m. frame of a_1 and a_2 and the c.m. moving direction of the pair in the lab frame. For $m_a \neq 0$, the $\cos\Theta$ distribution does not present a sharp cusp or endpoint [96]. If $m_a = 0$, however, the distribution has a simple functional form as

$$\left.\frac{d\Gamma}{d\cos\Theta}\right|_{m_a=0} \propto \begin{cases} \dfrac{1}{\sin^3\Theta}, & \text{for } |\cos\Theta| < \beta_B, \\ 0, & \text{otherwise,} \end{cases} \tag{B.11}$$

which accommodates two pronounced peaks where the cusp and the maximum endpoint meet at $\cos\Theta = \pm\beta_B$.

APPENDIX C

LOG-LIKELIHOOD COMBINATION

We have found that combining the log-likelihoods for our kinematic variables did not significantly improve the achievable accuracy of the mass measurement. The reason for this was a combination of the correlation between the variables, the slight differences in how the log-likelihood depended on each kinematic variable, and how the combination is affected by having a large number of bins in each log-likelihood, as we will now explain.

We have found that the log-likelihood for the variables $m_{\mu\mu}$, m_{rec}, E_{μ}, $E_{\mu\mu}$ and E_{rec} depends approximately quadratically on the mass difference Δm, where Δm is defined to be along the diagonal line with negative slope in Fig. 29,

$$LL = \alpha_{kv} \left(\Delta m\right)^2 \ , \tag{C.1}$$

where α_{kv} is a constant to be determined for each kinematic variable. We will consider the optimal situation where the kinematic variables are completely uncorrelated and α_{kv} is the same for each kinematic variable and set $\alpha_{kv} = \alpha$. In this case, the joint test statistic is the sum of the N individual test statistics

$$t_N = N\alpha \left(\Delta m\right)^2 \ . \tag{C.2}$$

If the number of bins n is large (which is a good approximation in our case with 50 bins for each log-likelihood), then the individual log-likelihoods and the joint test-statistic are well-approximated by Gaussian distributions with mean $\mu_N = Nn$ and standard deviation

$\sigma_N = \sqrt{2Nn}$, where the individual log-likelihoods have $\mu_1 = n$ and $\sigma_1 = \sqrt{2n}$. This means that the joint test-statistic gives a $2\sigma_N$ measurement in the mass difference as

$$N\alpha \left(\Delta m\right)^2_{2\sigma_N} = Nn + 2\sqrt{2Nn} \tag{C.3}$$

while that for an individual log-likelihood has $N = 1$. Solving this for Δm gives

$$\left(\Delta m\right)_{2\sigma_N} = \sqrt{\frac{n}{\alpha} + \frac{2}{\alpha}\sqrt{\frac{2n}{N}}} \, . \tag{C.4}$$

If we take the ratio of this with an individual log-likelihood measurement, we have

$$\frac{\left(\Delta m\right)_{2\sigma_N}}{\left(\Delta m\right)_{2\sigma_1}} = \sqrt{\frac{n + 2\sqrt{2n/N}}{n + 2\sqrt{2n}}} \, , \tag{C.5}$$

where α has dropped out. We can use this formula to note a few things. First of all, we see that the maximum improvement in the sensitivity achievable asymptotically approaches 0 for the large number of bin n limit, independent of the number of log-likelihoods N combined in this way. Second, for $n = 50$ bins, the maximum improvement in the combined measurement sensitivity is 14.5% in the limit that the number of combined log-likelihoods, N, approaches infinity. Third, if we only combine $N = 2$ or 3 log-likelihoods, the maximum sensitivity improvement is only 4.3% and 6.2%, respectively. This is in the best case scenario where all the variables are uncorrelated and each α_{kv} is identical. In the realistic cases in this paper, the sensitivity improvement from combination is no more than a few percent.

BIBLIOGRAPHY

[1] P. A. M. Dirac, Proc. Roy. Soc. Lond. A **114**, 243 (1927). doi:10.1098/rspa.1927.0039

[2] H. A. Bethe, Phys. Rev. **72**, 339 (1947). doi:10.1103/PhysRev.72.339

[3] W. E. Lamb and R. C. Retherford, Phys. Rev. **72**, 241 (1947). doi:10.1103/PhysRev.72.241

[4] S. Tomonaga, Prog. Theor. Phys. **1**, 27 (1946). doi:10.1143/PTP.1.27

[5] J. S. Schwinger, Phys. Rev. **74**, 1439 (1948). doi:10.1103/PhysRev.74.1439

[6] R. P. Feynman, Phys. Rev. **76**, 769 (1949). doi:10.1103/PhysRev.76.769

[7] R. P. Feynman, Phys. Rev. **76**, 749 (1949). doi:10.1103/PhysRev.76.749

[8] R. P. Feynman, Phys. Rev. **80**, 440 (1950). doi:10.1103/PhysRev.80.440

[9] F. J. Dyson, Phys. Rev. **75**, 486 (1949). doi:10.1103/PhysRev.75.486

[10] F. J. Dyson, Phys. Rev. **75**, 1736 (1949). doi:10.1103/PhysRev.75.1736

[11] M. D. Schwartz,

[12] M. Gell-Mann, CTSL-20, TID-12608.

[13] Y. Neeman, IA-698.

[14] G. Zweig, CERN-TH-401.

[15] M. Y. Han and Y. Nambu, Phys. Rev. **139**, B1006 (1965). doi:10.1103/PhysRev.139.B1006

[16] O. W. Greenberg, Phys. Rev. Lett. **13**, 598 (1964). doi:10.1103/PhysRevLett.13.598

[17] J. D. Bjorken and E. A. Paschos, Phys. Rev. **185**, 1975 (1969). doi:10.1103/PhysRev.185.1975

[18] C. N. Yang and R. L. Mills, Phys. Rev. **96**, 191 (1954). doi:10.1103/PhysRev.96.191

[19] H. Fritzsch, M. Gell-Mann and H. Leutwyler, Phys. Lett. **47B**, 365 (1973). doi:10.1016/0370-2693(73)90625-4

[20] H. D. Politzer, Phys. Rev. Lett. **30**, 1346 (1973). doi:10.1103/PhysRevLett.30.1346

[21] D. J. Gross and F. Wilczek, Phys. Rev. Lett. **30**, 1343 (1973). doi:10.1103/PhysRevLett.30.1343

[22] E. Fermi, Z. Phys. **88**, 161 (1934). doi:10.1007/BF01351864

[23] G. Gamow and E. Teller, Phys. Rev. **49**, 895 (1936). doi:10.1103/PhysRev.49.895

[24] T. D. Lee and C. N. Yang, Phys. Rev. **104**, 254 (1956). doi:10.1103/PhysRev.104.254

[25] C. S. Wu, E. Ambler, R. W. Hayward, D. D. Hoppes and R. P. Hudson, Phys. Rev. **105**, 1413 (1957). doi:10.1103/PhysRev.105.1413

[26] R. P. Feynman and M. Gell-Mann, Phys. Rev. **109**, 193 (1958). doi:10.1103/PhysRev.109.193

[27] E. C. G. Sudarshan and R. e. Marshak, Phys. Rev. **109**, 1860 (1958). doi:10.1103/PhysRev.109.1860.2

[28] S. L. Glashow, Nucl. Phys. **22**, 579 (1961). doi:10.1016/0029-5582(61)90469-2

[29] F. Englert and R. Brout, Phys. Rev. Lett. **13**, 321 (1964). doi:10.1103/PhysRevLett.13.321

[30] P. W. Higgs, Phys. Rev. Lett. **13**, 508 (1964). doi:10.1103/PhysRevLett.13.508

[31] G. S. Guralnik, C. R. Hagen and T. W. B. Kibble, Phys. Rev. Lett. **13**, 585 (1964). doi:10.1103/PhysRevLett.13.585

[32] S. Weinberg, Phys. Rev. Lett. **19**, 1264 (1967). doi:10.1103/PhysRevLett.19.1264

[33] M. Duhrssen, S. Heinemeyer, H. Logan, D. Rainwater, G. Weiglein, et al., *Extracting Higgs boson couplings from CERN LHC data*, *Phys.Rev.* **D70** (2004) 113009, [hep-ph/0406323].

[34] V. Barger, M. Ishida, and W.-Y. Keung, *Total Width of 125 GeV Higgs Boson*, *Phys.Rev.Lett.* **108** (2012) 261801, [arXiv:1203.3456].

[35] M. E. Peskin, *Comparison of LHC and ILC Capabilities for Higgs Boson Coupling Measurements*, arXiv:1207.2516.

[36] **LHC Higgs Cross Section Working Group** Collaboration, A. David et al., *LHC HXSWG interim recommendations to explore the coupling structure of a Higgs-like particle*, arXiv:1209.0040.

[37] B. A. Dobrescu and J. D. Lykken, *Coupling spans of the Higgs-like boson*, *JHEP* **1302** (2013) 073, [arXiv:1210.3342].

[38] T. Han and Z. Liu, *Direct Measurement of the Higgs Boson Total Width at a Muon Collider*, *Phys.Rev.* **D87** (2013) 033007, [arXiv:1210.7803].

[39] S. P. Martin, *Shift in the LHC Higgs diphoton mass peak from interference with background*, *Phys.Rev.* **D86** (2012) 073016, [arXiv:1208.1533].

[40] N. Kauer and G. Passarino, *Inadequacy of zero-width approximation for a light Higgs boson signal*, *JHEP* **1208** (2012) 116, [arXiv:1206.4803].

[41] L. J. Dixon and Y. Li, *Bounding the Higgs Boson Width Through Interferometry*, *Phys.Rev.Lett.* **111** (2013) 111802, [arXiv:1305.3854].

[42] F. Caola and K. Melnikov, *Constraining the Higgs boson width with ZZ production at the LHC*, *Phys.Rev.* **D88** (2013) 054024, [arXiv:1307.4935].

[43] J. M. Campbell, R. K. Ellis, and C. Williams, *Bounding the Higgs width at the LHC: complementary results from $H \to WW$*, *Phys.Rev.* **D89** (2014) 053011, [arXiv:1312.1628].

[44] J. M. Campbell, R. K. Ellis, and C. Williams, *Bounding the Higgs width at the LHC using full analytic results for $gg- > e^-e^+\mu^-\mu^+$*, *JHEP* **1404** (2014) 060, [arXiv:1311.3589].

[45] **CMS** Collaboration, V. Khachatryan et al., *Constraints on the Higgs boson width from off-shell production and decay to Z-boson pairs*, *Phys.Lett.* **B736** (2014) 64, [arXiv:1405.3455].

[46] **ATLAS** Collaboration, *Determination of the off-shell Higgs boson signal strength in the high-mass ZZ final state with the ATLAS detector*, *ATLAS-CONF-2014-042, ATLAS-COM-CONF-2014-052* (2014).

[47] S. Liebler, G. Moortgat-Pick, and G. Weiglein, *Off-shell effects in Higgs processes at a linear collider and implications for the LHC*, *JHEP* **1506** (2015) 093, [arXiv:1502.0797].

[48] T. Han, Z. Liu, and J. Sayre, *Potential Precision on Higgs Couplings and Total Width at the ILC*, *Phys.Rev.* **D89** (2014) 113006, [arXiv:1311.7155].

[49] **ILD Design Study Group** Collaboration, H. Li et al., *HZ Recoil Mass and Cross Section Analysis in ILD*, arXiv:1202.1439.

[50] H. Li, *Higgs Recoil Mass and Higgs-Strahlung Cross-Section Study for the ILD LOI*, arXiv:1007.2999.

[51] A. Miyamoto, *A measurement of the total cross section of σ_{Zh} at a future e^+e^- collider using the hadronic decay mode of Z*, arXiv:1311.2248.

[52] J. Gunion, T. Han, and R. Sobey, *Determining the Coupling of a Higgs Boson to ZZ at Linear Colliders*, *Phys.Lett.* **B429** (1998) 79–86, [hep-ph/9801317].

[53] T. Han and J. Jiang, *CP-violating ZZh Coupling at e+e- Linear Colliders*, *Phys.Rev.D* **63** (2001) 096007, [hep-ph/0011271].

[54] M. Berggren, *SGV 3.0 - a fast detector simulation*, arXiv:1203.0217.

[55] D. Schulte, *Beam-beam simulations with GUINEA-PIG*, *CERN-PS-99-014-LP, CERN-PS-99-14-LP, CLIC-NOTE-387, CERN-CLIC-NOTE-387* (1999).

[56] W. Kilian, T. Ohl, and J. Reuter, *WHIZARD: Simulating Multi-Particle Processes at LHC and ILC*, *Eur.Phys.J.* **C71** (2011) 1742, [arXiv:0708.4233].

[57] T. Sjostrand, S. Mrenna, and P. Z. Skands, *PYTHIA 6.4 Physics and Manual*, *JHEP* **0605** (2006) 026, [hep-ph/0603175].

[58] H. Baer, T. Barklow, K. Fujii, Y. Gao, A. Hoang, et al., *The International Linear Collider Technical Design Report - Volume 2: Physics*, arXiv:1306.6352.

[59] S. Dawson, A. Gritsan, H. Logan, J. Qian, C. Tully, et al., *Working Group Report: Higgs Boson*, arXiv:1310.8361.

[60] D. Asner, T. Barklow, C. Calancha, K. Fujii, N. Graf, et al., *ILC Higgs White Paper*, arXiv:1310.0763.

[61] S. Weinberg, *Phenomenological Lagrangians*, *Physica* **A96** (1979) 327.

[62] C. N. Leung, S. Love, and S. Rao, *Low-Energy Manifestations of a New Interaction Scale: Operator Analysis*, *Z.Phys.* **C31** (1986) 433.

[63] W. Buchmuller and D. Wyler, *Effective Lagrangian Analysis of New Interactions and Flavor Conservation*, *Nucl.Phys.* **B268** (1986) 621–653.

[64] K. Hagiwara, R. Szalapski, and D. Zeppenfeld, *Anomalous Higgs boson production and decay*, *Phys.Lett.* **B318** (1993) 155–162, [hep-ph/9308347].

[65] G. Giudice, C. Grojean, A. Pomarol, and R. Rattazzi, *The Strongly-Interacting Light Higgs*, *JHEP* **0706** (2007) 045, [hep-ph/0703164].

[66] B. Grzadkowski, M. Iskrzynski, M. Misiak, and J. Rosiek, *Dimension-Six Terms in the Standard Model Lagrangian*, *JHEP* **1010** (2010) 085, [arXiv:1008.4884].

[67] R. Contino, M. Ghezzi, C. Grojean, M. Muhlleitner, and M. Spira, *Effective Lagrangian for a light Higgs-like scalar*, *JHEP* **1307** (2013) 035, [arXiv:1303.3876].

[68] **Particle Data Group** Collaboration, K. Olive et al., *Review of Particle Physics*, *Chin.Phys.* **C38** (2014) 090001.

[69] J. Ellis, V. Sanz, and T. You, *Complete Higgs Sector Constraints on Dimension-6 Operators*, *JHEP* **1407** (2014) 036, [arXiv:1404.3667].

[70] J. Ellis, V. Sanz, and T. You, *The Effective Standard Model after LHC Run I*, *JHEP* **1503** (2015) 157, [arXiv:1410.7703].

[71] A. Biekötter, A. Knochel, M. Krämer, D. Liu, and F. Riva, *Vices and virtues of Higgs effective field theories at large energy*, *Phys.Rev.* **D91** (2015) 055029, [arXiv:1406.7320].

[72] A. Falkowski and F. Riva, *Model-independent precision constraints on dimension-6 operators*, *JHEP* **1502** (2015) 039, [arXiv:1411.0669].

[73] M. Beneke, D. Boito, and Y.-M. Wang, *Anomalous Higgs couplings in angular asymmetries of $H \to Z\ell^+\ell^-$ and $e^+ e^- \to HZ$*, *JHEP* **1411** (2014) 028, [arXiv:1406.1361].

[74] N. Craig, M. Farina, M. McCullough, and M. Perelstein, *Precision Higgsstrahlung as a Probe of New Physics*, *JHEP* **1503** (2015) 146, [arXiv:1411.0676].

[75] V. Barger, T. Han, P. Langacker, B. McElrath, and P. Zerwas, *Effects of genuine dimension-six Higgs operators*, *Phys.Rev.D* **67** (2003) 115001, [hep-ph/0301097].

[76] N. Craig, S. Knapen, and P. Longhi, *Neutral Naturalness from Orbifold Higgs Models*, *Phys.Rev.Lett.* **114** (2015), no. 6 061803, [arXiv:1410.6808].

[77] A. Azatov, C. Grojean, A. Paul, and E. Salvioni, *Taming the off-shell Higgs boson*, *Zh.Eksp.Teor.Fiz.* **147** (2015) 410–425, [arXiv:1406.6338].

[78] D. Curtin, P. Meade, and C.-T. Yu, *Testing Electroweak Baryogenesis with Future Colliders*, *JHEP* **1411** (2014) 127, [arXiv:1409.0005].

[79] Z. Chacko, H.-S. Goh, and R. Harnik, *The Twin Higgs: Natural electroweak breaking from mirror symmetry*, *Phys.Rev.Lett.* **96** (2006) 231802, [hep-ph/0506256].

[80] G. Burdman, Z. Chacko, H.-S. Goh, and R. Harnik, *Folded supersymmetry and the LEP paradox*, *JHEP* **0702** (2007) 009, [hep-ph/0609152].

[81] G. Aad et al. [ATLAS Collaboration], *Phys. Lett. B* **716**, 1 (2012) [arXiv:1207.7214]; S. Chatrchyan et al. [CMS Collaboration], Phys. Lett. B **716**, 30 (2012) [arXiv:1207.7235]; G. Aad et al. [ATLAS Collaboration], Phys. Rev. D **86**, 032003 (2012) [arXiv:1207.0319]; S. Chatrchyan et al. [CMS Collaboration], Phys. Lett. B **710**, 26 (2012) [arXiv:1202.1488]; CMS Collaboration, CMS-PAS-HIG-13-005; ATLAS Collaboration, ATLAS-CONF-2013-034.

[82] F. Zwicky, Helv. Phys. Acta **6**, 110 (1933); V. C. Rubin and W. K. Ford, Jr., Astrophys. J. **159**, 379 (1970); V. C. Rubin, N. Thonnard and W. K. Ford, Jr., Astrophys. J. **238**, 471 (1980); A. Bosma, Astron. J. **86**, 1825 (1981).

[83] E. Komatsu et al. [WMAP Collaboration], Astrophys. J. Suppl. **192**, 18 (2011) [arXiv:1001.4538].

[84] B. Fields and S. Sarkar, J. Phys. G **G33**, 1 (2006) [astro-ph/0601514].

[85] A. Refregier, Ann. Rev. Astron. Astrophys. **41**, 645 (2003) [astro-ph/0307212]; J. A. Tyson, G. P. Kochanski and I. P. Dell'Antonio, Astrophys. J. **498**, L107 (1998) [astro-ph/9801193].

[86] D. Clowe, M. Bradac, A. H. Gonzalez, M. Markevitch, S. W. Randall, C. Jones and D. Zaritsky, Astrophys. J. **648**, L109 (2006) [astro-ph/0608407].

[87] For a recent review, see e.g., J. L. Feng, Ann. Rev. Astron. Astrophys. **48**, 495 (2010) [arXiv:1003.0904], and references therein.

[88] E. Aprile et al. [XENON100 Collaboration], Phys. Rev. Lett. **109**, 181301 (2012) [arXiv:1207.5988].

[89] D. S. Akerib et al. [LUX Collaboration], Phys. Rev. Let **112**, 091303 (2014) [arXiv:1310.8214].

[90] R. Agnese et al. [SuperCDMSSoudan Collaboration], Phys. Rev. Lett. **112**, 041302 (2014) [arXiv:1309.3259].

[91] I. Hinchliffe, F. E. Paige, M. D. Shapiro, J. Soderqvist and W. Yao, Phys. Rev. D **55**, 5520 (1997) [hep-ph/9610544]; H. Bachacou, I. Hinchliffe and F. E. Paige, Phys. Rev. D **62**, 015009 (2000) [hep-ph/9907518]; B. C. anach, C. G. Lester, M. A. Parker and B. R. Webber, JHEP **0009**, 004 (2000) [hep-ph/0007009]; B. K. Gjelsten, D. J. Miller and P. Osland, JHEP **0412**, 003 (2004) [hep-ph/0410303]; B. K. Gjelsten, D. J. Miller and P. Osland, JHEP **0506**, 015 (2005) [hep-ph/0501033].

[92] H. C. Cheng, D. Engelhardt, J. F. Gunion, Z. Han and B. McElrath, Phys. Rev. Lett. **100**, 252001 (2008) [arXiv:0802.4290]; H. C. Cheng, J. F. Gunion, Z. Han, G. Marandella and B. McElrath, JHEP **0712**, 076 (2007) [arXiv:0707.0030]; M. M. Nojiri, G. Polesello and D. R. Tovey, [hep-ph/0312317]; K. Kawagoe, M. M. Nojiri and G. Polesello, Phys. Rev. D **71**, 035008 (2005) [hep-ph/0410160].

[93] C. G. Lester and D. J. Summers, Phys. Lett. B **463**, 99 (1999) [hep-ph/9906349]; A. Barr, C. Lester and P. Stephens, J. Phys. G **29**, 2343 (2003) [hep-ph/0304226]; M. M. Nojiri and M. Takeuchi, JHEP **0810**, 025 (2008) [arXiv:0802.4142]; P. Meade and M. Reece, Phys. Rev. D **74**, 015010 (2006) [hep-ph/0601124]; S. Matsumoto, M. M. Nojiri and D. Nomura, Phys. Rev. D **75**, 055006 (2007) [hep-ph/0612249]; C. Lester and A. Barr, JHEP **0712**, 102 (2007) [arXiv:0708.1028]; W. S. Cho, K. Choi, Y. G. Kim and C. B. Park, Phys. Rev. Lett. **100**, 171801 (2008) [arXiv:0709.0288]; B. Gripaios, JHEP **0802**, 053 (2008) [arXiv:0709.2740]; A. J. Barr, B. Gripaios and C. G. Lester, JHEP **0802**, 014 (2008) [arXiv:0711.4008]; W. S. Cho, K. Choi, Y. G. Kim and C. B. Park, JHEP **0802**,

035 (2008) [arXiv:0711.4526]; M. M. Nojiri, Y. Shimizu, S. Okada and K. Kawagoe, JHEP **0806**, 035 (2008) [arXiv:0802.2412].

[94] J. Alwall, A. Freitas and O. Mattelaer, AIP Conf. Proc. **1200**, 442 (2010) [arXiv:0910.2522 [hep-ph]]; J. S. Gainer, J. Lykken, K. T. Matchev, S. Mrenna and M. Park, arXiv:1307.3546 [hep-ph].

[95] T. Han, I. -W. Kim and J. Song, Phys. Lett. B **693**, 575 (2010) [arXiv:0906.5009].

[96] T. Han, I. -W. Kim and J. Song, Phys. Rev. D **87**, no. 3, 035003 (2013) [arXiv:1206.5633]; T. Han, I. -W. Kim and J. Song, Phys. Rev. D **87**, no. 3, 035004 (2013) [arXiv:1206.5641].

[97] K. Agashe, D. Kim, M. Toharia and D. G. E. Walker, Phys. Rev. D **82**, 015007 (2010) [arXiv:1003.0899]; K. Agashe, R. Franceschini and D. Kim, [arXiv:1309.4776].

[98] T. Behnke, J. E. Brau, B. Foster, J. Fuster, M. Harrison, J. M. Paterson, M. Peskin and M. Stanitzki et al., [arXiv:1306.6327]; H. Baer, T. Barklow, K. Fujii, Y. Gao, A. Hoang, S. Kanemura, J. List and H. E. Logan et al., [arXiv:1306.6352]; T. Behnke, J. E. Brau, P. N. Burrows, J. Fuster, M. Peskin, M. Stanitzki, Y. Sugimoto and S. Yamada et al., [arXiv:1306.6329].

[99] M. Koratzinos, A. P. Blondel, R. Aleksan, O. Brunner, A. Butterworth, P. Janot, E. Jensen and J. Osborne et al., [arXiv:1305.6498]; M. Bicer, H. Duran Yildiz, I. Yildiz, G. Coignet, M. Delmastro, T. Alexopoulos, C. Grojean and S. Antusch et al., [arXiv:1308.6176].

[100] E. Accomando et al. [CLIC Physics Working Group Collaboration], [hep-ph/0412251]; L. Linssen, A. Miyamoto, M. Stanitzki and H. Weerts, [arXiv:1202.5940].

[101] C. M. Ankenbrandt, M. Atac, B. Autin, V. I. Balbekov, V. D. Barger, O. Benary, J. S. Berg and M. S. Berger et al., Phys. Rev. ST Accel. Beams **2**, 081001 (1999) [physics/9901022].

[102] H. U. Martyn, [hep-ph/0408226], and references therein.

[103] P. Konar, K. Kong, K. T. Matchev and M. Perelstein, New J. Phys. **11**, 105004 (2009) [arXiv:0902.2000]; J. A. Conley, H. K. Dreiner and P. Wienemann, Phys. Rev. D **83**, 055018 (2011) [arXiv:1012.1035]; Y. J. Chae and M. Perelstein, JHEP **1305**, 138 (2013) [arXiv:1211.4008].

[104] G. Aarons et al. [ILC Collaboration Design Report], arXiv:0709.1893 [hep-ph]; A. Freitas, D. J. Miller and P. M. Zerwas, Eur. Phys. J. C **21**, 361 (2001) [hep-ph/0106198]; A. Freitas, A. von Manteuffel and P. M. Zerwas, Eur. Phys. J. C **34**, 487 (2004) [hep-ph/0310182].

[105] N. D. Christensen and D. Salmon, Phys. Rev. D **90**, 014025 (2014) [arXiv:1311.6465 [hep-ph]].

[106] G. Aad *et al.* [ATLAS Collaboration], JHEP **1405**, 071 (2014) [arXiv:1403.5294 [hep-ex]]; V. Khachatryan *et al.* [CMS Collaboration], arXiv:1405.7570 [hep-ex].

[107] The ATLAS collaboration, ATLAS-CONF-2013-093; G. Aad *et al.* [ATLAS Collaboration], JHEP **1405**, 071 (2014) [arXiv:1403.5294 [hep-ex]]; CMS Collaboration [CMS Collaboration], CMS-PAS-SUS-13-017; V. Khachatryan *et al.* [CMS Collaboration], arXiv:1405.7570 [hep-ex].

[108] For a phenomenological overview, see, e.g., T. Han, S. Padhi and S. Su, Phys. Rev. D **88**, 115010 (2013) [arXiv:1309.5966 [hep-ph]].

[109] J. Kalinowski, W. Kilian, J. Reuter, T. Robens and K. Rolbiecki, JHEP **0810**, 090 (2008) [arXiv:0809.3997 [hep-ph]].

[110] T. Abe et al. [American Linear Collider Working Group], [hep-ex/0106055]; R. Blankenbecler and S. D. Drell, Phys. Rev. D **36**, 277 (1987); M. Bell and J. S. Bell, Part. Accel. **22** (1988) 301.

[111] W. Kilian, T. Ohl and J. Reuter, Eur. Phys. J. C **71**, 1742 (2011) [arXiv:0708.4233].

[112] A. Belyaev, N. D. Christensen and A. Pukhov, Comput. Phys. Commun. **184**, 1729 (2013) [arXiv:1207.6082].

[113] K. Hagiwara, R. D. Peccei, D. Zeppenfeld and K. Hikasa, Nucl. Phys. B **282**, 253 (1987).

[114] A. Birkedal, K. Matchev and M. Perelstein, Phys. Rev. D **70**, 077701 (2004) [hep-ph/0403004].

[115] E. A. Baltz, M. Battaglia, M. E. Peskin and T. Wizansky, Phys. Rev. D **74**, 103521 (2006) [hep-ph/0602187], and references therein.

[116] M. Berggren, arXiv:1203.0217 [physics.ins-det].

[117] **ATLAS** Collaboration, G. Aad et al., *Observation of a new particle in the search for the Standard Model Higgs boson with the ATLAS detector at the LHC*, *Phys. Lett.* **B716** (2012) 1–29, [arXiv:1207.7214].

[118] **CMS** Collaboration, S. Chatrchyan et al., *Observation of a new boson at a mass of 125 GeV with the CMS experiment at the LHC*, *Phys. Lett.* **B716** (2012) 30–61, [arXiv:1207.7235].

[119] **ATLAS** Collaboration, G. Aad et al., *Observation and measurement of Higgs boson decays to WW* with the ATLAS detector*, *Phys. Rev.* **D92** (2015), no. 1 012006, [arXiv:1412.2641].

[120] **CMS** Collaboration, S. Chatrchyan et al., *Measurement of Higgs boson production and properties in the WW decay channel with leptonic final states*, *JHEP* **01** (2014) 096, [arXiv:1312.1129].

[121] **ATLAS, CMS** Collaboration, G. Aad et al., *Measurements of the Higgs boson production and decay rates and constraints on its couplings from a combined ATLAS and CMS analysis of the LHC pp collision data at $\sqrt{s} = 7$ and 8 TeV*, *JHEP* **08** (2016) 045, [arXiv:1606.02266].

[122] **CMS** Collaboration, V. Khachatryan et al., *Search for a Standard Model Higgs Boson Produced in Association with a Top-Quark Pair and Decaying to Bottom Quarks Using a Matrix Element Method*, *Eur. Phys. J.* **C75** (2015), no. 6 251, [arXiv:1502.02485].

[123] **ATLAS** Collaboration, G. Aad et al., *Search for the Standard Model Higgs boson decaying into $b\bar{b}$ produced in association with top quarks decaying hadronically in pp collisions at $\sqrt{s} = 8$ TeV with the ATLAS detector*, *JHEP* **05** (2016) 160, [arXiv:1604.03812].

[124] **ATLAS** Collaboration, *A study of standard model higgs boson production in the decay mode h bb in association with a w or z boson for high luminosity lhc running*, tech. rep., ATL-PHYS-PUB-2014-011, July, 2014.

[125] **ATLAS** Collaboration, *Projections for measurements of Higgs boson signal strengths and coupling parameters with the ATLAS detector at a HL-LHC*, Tech. Rep. ATL-PHYS-PUB-2014-016, CERN, Geneva, Oct, 2014.

[126] T. Han and B. McElrath, *h to mu+ mu- via gluon fusion at the LHC*, *Phys. Lett.* **B528** (2002) 81–85, [hep-ph/0201023].

[127] D. Asner, T. Barklow, C. Calancha, K. Fujii, N. Graf, H. E. Haber, A. Ishikawa, S. Kanemura, S. Kawada, M. Kurata, A. Miyamoto, H. Neal, H. Ono, C. Potter, J. Strube, T. Suehara, T. Tanabe, J. Tian, K. Tsumura, S. Watanuki, G. Weiglein, K. Yagyu, and H. Yokoya, *Ilc higgs white paper*, arXiv:1310.0763.

[128] **FCC-ee study** Collaboration, M. Koratzinos, *FCC-ee accelerator parameters, performance and limitations*, *Nucl. Part. Phys. Proc.* **273-275** (2016) 2326–2328, [arXiv:1411.2819].

[129] **CEPC-SPPC Study Group** Collaboration, *CEPC-SPPC Preliminary Conceptual Design Report. 1. Physics and Detector, http://inspirehep.net/record/1395734*, .

[130] J. M. Butterworth, A. R. Davison, M. Rubin, and G. P. Salam, *Jet substructure as a new Higgs search channel at the LHC*, *AIP Conf. Proc.* **1078** (2009) 189–191, [arXiv:0809.2530].

[131] G. Perez, Y. Soreq, E. Stamou, and K. Tobioka, *Prospects for measuring the Higgs coupling to light quarks*, arXiv:1505.06689.

[132] G. T. Bodwin, F. Petriello, S. Stoynev, and M. Velasco, *Higgs boson decays to quarkonia and the $H\bar{c}c$ coupling*, *Phys. Rev.* **D88** (2013), no. 5 053003, [arXiv:1306.5770].

[133] **ATLAS** Collaboration, G. Aad et al., *Search for Higgs and Z Boson Decays to J/ and (nS) with the ATLAS Detector*, *Phys. Rev. Lett.* **114** (2015), no. 12 121801, [arXiv:1501.03276].

[134] **ATLAS** Collaboration, *Search for the Standard Model Higgs and Z Boson decays to $J/\psi\,\gamma$: HL-LHC projections*, Tech. Rep. ATL-PHYS-PUB-2015-043, CERN, Geneva, Sep, 2015.

[135] I. Brivio, F. Goertz, and G. Isidori, *Probing the Charm Quark Yukawa Coupling in Higgs+Charm Production*, *Phys. Rev. Lett.* **115** (2015), no. 21 211801, [arXiv:1507.02916].

[136] T. Han and X. Wang, arXiv:1704.00790 [hep-ph].

[137] **LHC Higgs Cross Section Working Group** Collaboration, D. de Florian et al., *Handbook of LHC Higgs Cross Sections: 4. Deciphering the Nature of the Higgs Sector*, arXiv:1610.07922.

[138] **NNPDF** Collaboration, R. D. Ball, V. Bertone, S. Carrazza, L. Del Debbio, S. Forte, A. Guffanti, N. P. Hartland, and J. Rojo, *Parton distributions with QED corrections*, *Nucl. Phys.* **B877** (2013) 290–320, [arXiv:1308.0598].

[139] J. Alwall, R. Frederix, S. Frixione, V. Hirschi, F. Maltoni, O. Mattelaer, H. S. Shao, T. Stelzer, P. Torrielli, and M. Zaro, *The automated computation of tree-level and next-to-leading order differential cross sections, and their matching to parton shower simulations*, *JHEP* **07** (2014) 079, [arXiv:1405.0301].

[140] P. Artoisenet, R. Frederix, O. Mattelaer, and R. Rietkerk, *Automatic spin-entangled decays of heavy resonances in Monte Carlo simulations*, *JHEP* **03** (2013) 015, [arXiv:1212.3460].

[141] C. Englert, M. McCullough, and M. Spannowsky, *Gluon-initiated associated production boosts higgs physics*, arXiv:1310.4828.

[142] T. Sjostrand, S. Mrenna, and P. Z. Skands, *PYTHIA 6.4 Physics and Manual*, *JHEP* **05** (2006) 026, [hep-ph/0603175].

[143] **DELPHES 3** Collaboration, J. de Favereau, C. Delaere, P. Demin, A. Giammanco, V. Lemaître, A. Mertens, and M. Selvaggi, *DELPHES 3, A modular framework for fast simulation of a generic collider experiment*, *JHEP* **02** (2014) 057, [arXiv:1307.6346].

[144] S. D. Ellis, C. K. Vermilion, and J. R. Walsh, *Techniques for improved heavy particle searches with jet substructure*, *Phys. Rev.* **D80** (2009) 051501, [arXiv:0903.5081].

[145] D. Krohn, J. Thaler, and L.-T. Wang, *Jet Trimming*, *JHEP* **02** (2010) 084, [arXiv:0912.1342].

[146] J. Thaler and K. Van Tilburg, *Identifying Boosted Objects with N-subjettiness*, *JHEP* **03** (2011) 015, [arXiv:1011.2268].

[147] S. Sapeta, *QCD and Jets at Hadron Colliders*, *Prog. Part. Nucl. Phys.* **89** (2016) 1–55, [arXiv:1511.09336].

[148] J. M. Butterworth, I. Ochoa, and T. Scanlon, *Boosted Higgs $\to b\bar{b}$ in vector-boson associated production at 14 TeV*, *Eur. Phys. J.* **C75** (2015), no. 8 366, [arXiv:1506.04973].

[149] A. Banfi and J. Cancino, *Implications of qcd radiative corrections on high-pt higgs searches*, arXiv:1207.0674.

[150] **ATLAS** Collaboration, *Expected pileup values at the HL-LHC*, Tech. Rep. ATL-UPGRADE-PUB-2013-014, CERN, Geneva, Sep, 2013.

[151] C. Shimmin and D. Whiteson, *Boosting low-mass hadronic resonances*, *Phys. Rev.* **D94** (2016), no. 5 055001, [arXiv:1602.07727].

[152] F. Bishara, U. Haisch, P. F. Monni, and E. Re, *Constraining light-quark yukawa couplings from higgs distributions*, arXiv:1606.09253.

[153] **CMS** Collaboration, *Search for the standard model higgs boson produced through vector boson fusion and decaying to b bbar*, arXiv:1506.01010.

[154] **ATLAS** Collaboration, *Search for the standard model higgs boson decaying into $b\bar{b}$ produced in association with top quarks decaying hadronically in pp collisions at $\sqrt{s}$=8 tev with the atlas detector*, arXiv:1604.03812.

[155] **CMS** Collaboration, *VBF H to bb using the 2015 data sample*, .

[156] G. Perez, Y. Soreq, E. Stamou, and K. Tobioka, *Constraining the charm yukawa and higgs-quark coupling universality*, arXiv:1503.00290.

[157] Y. Zhou, *Constraining the Higgs boson coupling to light quarks in the HZZ final states*, *Phys. Rev.* **D93** (2016), no. 1 013019, [arXiv:1505.06369].

[158] Y. Soreq, H. X. Zhu, and J. Zupan, *Light quark yukawa couplings from higgs kinematics*, arXiv:1606.09621.

[159] G. Bonner and H. E. Logan, *Constraining the Higgs couplings to up and down quarks using production kinematics at the CERN Large Hadron Collider*, arXiv:1608.04376.

[160] Y. Meng, Z. Surujon, A. Rajaraman, and T. M. P. Tait, *Strange Couplings to the Higgs*, *JHEP* **02** (2013) 138, [arXiv:1210.3373].

[161] F. Yu, *Phenomenology of Enhanced Light Quark Yukawa Couplings and the $W^{\pm}h$ Charge Asymmetry*, arXiv:1609.06592.

[162] A. L. Kagan, G. Perez, F. Petriello, Y. Soreq, S. Stoynev, and J. Zupan, *Exclusive Window onto Higgs Yukawa Couplings*, *Phys. Rev. Lett.* **114** (2015), no. 10 101802, [arXiv:1406.1722].

[163] **Particle Data Group** Collaboration, K. A. Olive et al., *Review of Particle Physics*, *Chin. Phys.* **C38** (2014) 090001.

[164] I. W. Kim, Phys. Rev. Lett. **104**, 081601 (2010) doi:10.1103/PhysRevLett.104.081601 [arXiv:0910.1149 [hep-ph]].